Joonas Heikkinen

Novel materials and devices for neuronal studies on microfluidic chips

School of Electrical Engineering

Thesis submitted for examination for the degree of Master of Science in Technology.

Espoo 19.10.2015

Thesis supervisor:

Prof. Sami Franssila

Thesis advisor:

Ph. D. Ville Jokinen

Aalto University
School of Electrical
Engineering

AALTO UNIVERSITY
SCHOOL OF ELECTRICAL ENGINEERING

ABSTRACT OF THE
MASTER'S THESIS

Author: Joonas Heikkinen

Title: Novel materials and devices for neuronal studies on microfluidic chips

Date: 19.10.2015 Language: English Number of pages: 7+90

Department of Materials Science and Engineering

Professorship: Material Science Code: MT-45

Supervisor: Prof. Sami Franssila

Advisor: Ph. D. Ville Jokinen

In this Master's thesis, the aim of the research was to characterize three new materials for neuronal studies, and fabricate functional neuron stimulation devices based on these materials using microfabrication techniques. Three different materials were studied with respect to their compatibility with nerve cells: thiol-ene based OSTE (off-stoichiometry thiol-ene) and OSTE+ (off-stoichiometry thiol-ene epoxy), and carbon-based NCC (nanocrystalline carbon). Polymer materials were characterized for their elastic properties and fabrication methods, and compared to conventional polymer PDMS (polydimethylsiloxane). OSTE(+) materials showed decent compatibility with neurons, as roughly 30 % of samples allowed neuron maturation. Axon stretching device fabricated from glass, PDMS and OSTE+ proved to function in wider strain range than many published devices, reaching strain as high as 80 % with 21 μN force.

Thin film of NCC was fabricated, and it was characterized for surface roughness (AFM, RMS 41 nm), chemical structure (Raman spectroscopy, peak ratio of sp^3 and sp^2 carbon bonds is D/G $\approx$ 1.00), and electrical resistivity (four point probe, 3.2 Ωcm). NCC was etched with plasma etching (O_2-based recipe) and highest achieved etch rate was 42 nm/min. NCC showed extraordinary biological property by enhancing the neuron maturation and neurite arborization during seven days of cultivation. Multielectrode array was successfully fabricated from silicon, silicon dioxide and NCC. The MEA had lower electrode resistance (R_{ave} = 6.5 Ω) compared to commercial product MED64 (R_{ave} = 460 Ω) with approximately same dimensions.

Keywords: Off-stoichiometry thiol-ene, OSTE, OSTE+, nanocrystalline carbon, NCC, neuron, axon stretching, microfluidics, enhanced maturation

AALTO-YLIOPISTO
SÄHKÖTEKNIIKAN KORKEAKOULU

DIPLOMITYÖN
TIIVISTELMÄ

Tekijä: Joonas Heikkinen

Työn nimi: Uudenlaiset materiaali- ja laiteratkaisut hermosolututkimuksiin mikrofluidistisissa järjestelmissä

Päivämäärä: 19.10.2015 Kieli: Englanti Sivumäärä: 7+90

Materiaalitekniikan laitos

Professuuri: Materiaalitiede Koodi: MT-45

Valvoja: Prof. Sami Franssila

Ohjaaja: FT Ville Jokinen

Tämän Diplomityön tarkoituksena oli tutkia ja karakterisoida kolme eri materiaalia hermosolututkimuksia varten, ja valmistaa niistä toiminnallisia hermosolun tutkimusalustoja mikrovalmistusteknologian keinoin. Kolme tutkittavaa materiaalia olivat: thioleeniin pohjautuvat OSTE (epästoikiometrinen thioleeni) ja OSTE+ (epästoikiometrinen thioleeni epoksi), sekä hiilipohjainen NCC (nanokristallihiili). Tutkimuksen alla oli erityisesti näiden materiaalien yhteensopivuus hermosolujen kanssa. Polymeerimateriaalit karakterisoitiin niiden elastisten ominaisuuksien ja valmistumenetelmien kautta, sekä näitä vertailtiin tavanomaiseen polymeerimateriaali PDMS:iin (polydimetyylisiloksaani). OSTE(+) materiaalit osoittivat keskinkertaista yhteensopivuutta hermosolujen kanssa, sillä noin 30 % näytteistä tuki hermosolujen kasvua ja kehittymistä. Aksonin venytysalusta valmistettiin onnistuneesti lasista, PDMS:sta ja OSTE+:sta, ja sen toiminta-alue osoittautui laajemmaksi verrattuna moneen aiemmin julkaistuun venytysalustaan saavuttaen jopa 80 % venymän alkuperäisestä pituudesta 21 μN voimalla.

NCC:ltä valmistettiin ohut kalvo ja mitattiin sen pinnankarheus (AFM, RMS 41 nm), kemiallinen rakenne (Raman spektroskopia, sp^3 ja sp^2 hiilisidosten huippuintensiteettiarvojen suhde D/G $\approx$ 1.00) ja sähköinen resistiivisyys (nelipistemittaus, 3.2 Ωcm). NCC:ltä etsattiin kuivaetsaamalla (O_2-pohjaisella kaasuyhdistelmällä) ja suurin saavutettu etsausnopeus on 42 nm/min. Lisäksi NCC tuotti epätavanomaisia hermokasvatustuloksia, kun se tehosti hermosolujen kehittymistä ja neuriittien haarautumista seitsemän päivän kasvatuskokeen aikana. Monielektrodijärjestelmä valmistettiin onnistuneesti piistä, piidioksidista ja NCC:stä. Järjestelmän elektrodiresistanssi oli matalampi (R_{ave} = 6.5 Ω) verrattuna kaupalliseen järjestelmään MED64:än (R_{ave} = 460 Ω), jossa oli suurinpiirtein samat dimensiot.

Avainsanat: Epästoikiometrinen thioleeni, OSTE, OSTE+, nanokristallihiili, NCC, hermosolu, aksonivenytys, mikrofluidistiikka, tehostettu maturaatio

Preface

The research was rewarding and challenging, but most of all, interesting. It opened my mind into totally different fields of science. During this work and my time in Microfabrication group, I have met wise, interesting, open-minded, and ingenious persons who are ready to rock. I have also met scientists.

First of all, I wish to thank professor Sami Franssila for taking me into the research group and then guiding me through this thesis, and giving ideas how to proceed when problems occurred. Huge gratitude goes Ph. D. Ville 'Joksa' Jokinen for patiently guiding me into the field of microfluidics and showing me the secrets of microfabrication. Also, thanks to Cecilia Brunello, Shokoufeh Khakipour, Tatiana Sukhanova, and Claudio Rivera for all the experiments done with neurons, this Thesis would not be a whole without the results. Appreciation goes also to whole Micronova infrastructure and research community for enabling the research.

Great thanks goes to my fellow colleagues (Mario, Giovanni, Ville, Sasha, Farzin, Ashkan, Anas, Maria, Juan, Topi, Anand...) in the group, who helped me to keep my sanity by offering relaxing discussion moments. Special gratitude goes to Mario and Giovanni for the G-word, lunch breaks, and other 37 Errors. I also want to show extra gratitude to Ville for all the scientific, non-scientific, and contemplating discussions during and between coffeebreaks.

Greatest gratitude goes to my fiancé Pauliina, who has shared the hard times and the good times during my study years, and who has encouraged me to continue beyond obstacles, but also who has restrained my mind when needed. I also give appreciation to my daughter, who motivated me to finish this Thesis in time.

I want to thank my parents Päivi and Markku for supporting me in all my choices, and for being truly happy of my achievements in life.

Last, but definitely not least, I want to thank the Inkubio Freshmen 2009, who I had the pleasure to get known, and who shared all the jolly good moments and expeditions during these six years. Thanks to my brother Pete for giving a warm welcome to this neighbourhood, which once was a long way from home. Overall, thanks to Otaniemi and all the people I have met during my time here, especially Inkubio, ITMK'11 and Pulterit. Without you guys and gals, I would not have participated in any student activity, and I dare to say, I would have missed a lot in life.

Otaniemi, 24.9.2015

Joonas Heikkinen

Contents

Symbols and abbreviations

Symbols

Re	Reynolds number
We	Weber number
Oh	Ohnesorge number
ρ	fluid density
v	velocity
L or l	length
μ	dynamic viscosity also denotes unit prefix *micro*, 10^{-6}
σ	surface tension
E	Young's modulus
I	second moment of area
w	deflection of a beam in the z direction at some position of x
x	point along a beam
q	uniform load
P	concentrated load
δ	deflection of a beam

Abbreviations

AC	Alter current
CFUBM	Close field unbalanced magnetron sputtering
CNC	Computer numerical control
CNT	Carbon nanotube
CVD	Chemical vapor deposition
CNS	Central nervous system
EOF	Electro-osmotic flow
DIV	Days in vitro
DI-water	Deionized water
FEB	Focused electron beam
FIB	Focused ion beam
HMDS	Hexamethyldisilazane
GFP	Green fluorescent protein
ICP-RIE	Inductively coupled plasma reactive ion etching
IPA	Isopropyl alcohol
ITO	Indium tin oxide
LDPE	Low-density polyethylene
LOC	Lab-on-a-chip
MEMS	Microelectromechanical system
MEA	Multielectrode array
MWCNT	Multiwalled carbon nanotube
NCC	Nanocrystalline carbon
OOC	Organ-on-a-chip
OSTE	Off-stoichiometric thiol-ene
OSTE+	Off-stoichiometric thiol-ene epoxy
PBS	Phosphate buffered saline
PDMS	Polydimethylsiloxane
PECVD	Plasma enhanced chemical vapor deposition
PGMEA	Propylene glycol methyl ether acetate
PLL	Poly-L-lysine
PMMA	Polymethylmethacrylate
PNS	Peripheral nervous system
PS	Polystyrene
PVD	Physical vapor deposition
RF	Radio frequency
RIE	Reactive ion etching
UV	Ultraviolet

1 Introduction

All living creatures from bacteria to mammals or from fungus to trees are formed from cells. Cell is the basic structural, functional, and biological unit of all living organisms. Most of the cells can replicate independently, and they have their own specific functionality. From the wide variety of different cell types, nerve cell shows extraordinary properties and high importance to multicellular animals. Therefore, in this Master's thesis, the focus will be in the study of three novel materials and their biocompatibility especially for neuroscience. The study is carried out with microfluidic devices, which allow simultaneous manipulation and monitoring of studied neurons.

The neuronal research emerged already in 19th century (first microscope image of a nerve cell by Gabriel Gustav Valentin, 1836), but the tenet of modern neuroscience, neuron doctrine, was published in 1888 by Santiago Ramón y Cajal [1]. The neuron doctrine combines many smaller theories into one entity, and the main argument is that the nervous system comprises from discrete individual cells: neurons. Neuron doctrine is the cornerstone on which all the neuroscientific disciplines were constructed throughout the 20th century.

The research tools, equipment, and methods in all scientific fields have improved remarkably from the days of first neuron images. Many of the developed equipment are taken into use in modern neuroscience, like scanning and transmission electron microscopes (SEM and TEM). These equipment allow more detailed and specific measurement, imaging, stimulation, and observation of the neurons under study. Also the sample size can nowadays be specified from conventional brain slices and cultured neuron populations to single cell analysis. The biocompatible material selection for neuronal research is getting larger all the time, and stunning designs and devices for neuroscience are developed by researcher all over the world.

In this Master's thesis, the aim of the research is to characterize three new materials for neuronal studies, and fabricate functional neuron stimulation devices based on these materials. Two of the materials under study are thiol-ene based polymers off-stoichiometry thiol-ene OSTE and off-stoichiometry thiol-ene epoxy OSTE+, which were first introduced by Carlborg et al. [2]. These materials show superior properties compared to other similar polymers, and therefore their compatibility in neuronal studies will be examined. Third material under study is carbon based material nanocrystalline carbon (NCC), which has shown interesting material properties. In general, carbon material family (carbon nanotube, graphene, fullerene, diamond...) is known to have unique properties which cannot be found in any other material [3, 4, 5].

These above-mentioned materials are adapted to two devices, which are described in this Master's thesis. Polymer materials are used in axon stretching chips as a biocompatible cell growth substrate, and carbon material is used in multielectrode array (MEA) system for cell growth but also for electrical measurements. In both devices, the main functionality requires isolation of axon from the neuron's cell body. For this purpose, a novel PDMS (polydimethylsiloxane) chip designed by Jokinen et al. [6] is used. In the final stage of the experiments, the axons are stretched in

axon stretching chip and the reactions of neurons are measured with confocal laser microscope. MEA chip is used to track and stimulate axons while they grow in axon isolation channels.

In this Master's thesis a brief introduction is given about neurons and microfluidic devices for neuronal studies. The studied polymer materials are introduced in detail with the aid of literature. The novel materials are compared to conventional ones, and their chemical composition, structure, properties and elastic abilities are presented. Different microfabrication techniques are introduced as they are needed in OSTE(+) fabrication and NCC patterning. The carbon material and its structure is also presented. Last part of introduction section presents equations concerning stretching of elastic membranes with load perpendicular to the membrane itself, as this information is needed with axon stretching chip characterization.

Materials and methods section introduces different polymer chip designs used, and presents in detail how the different polymers (PDMS, OSTE, OSTE+) are fabricated, and example processes are shown. MEA chip fabrication process and equipment parameters are also presented. Last part describes how the fabricated devices are intended to use. Results section presents fabrication notes for different polymer membrane types, characterizes the magnetic stretching properties of the axon stretching chip, characterizes MEA chip made from NCC, and shows neuronal biocompatibility tests and neuron maturation results made with the materials.

2 Theory and Background

The study of nerve cells emerged nearly two centuries ago, but there are still lots of mysteries and questions concerning neurons, and cells in general. Nowadays cell studies can be performed in selected environments (petri dishes, tissue slices, microdevices, *in vivo*...) and different data can be acquired with these tests. In this chapter the basics of neurobiology are presented. The field of microfluidics has shown interesting possibilities concerning cell and neuron studies, and the field is introduced here in more detail.

2.1 Nerve cell

Nerve cells act as "data highways" in almost all multicellular animals. The number of nerve cells can vary between 302 (Roundworm - Caenorhabditis elegans)[7] to 86 000 000 000 (Human - Homo sapiens sapiens)[8]. All the nerve cells form a nervous system, which can be further divided into central nervous system (CNS) and peripheral nervous system (PNS)[9]. In mammals, CNS consists of brain and spinal cord and PNS includes all the nervous tissue outside CNS. Multicellular animals have receptors to sense world around them and their own body. The signal from receptors is delivered through PNS to CNS, and processed in the brain. Brain undergoes complex series of signal analysis, and after decision making it sends signals back to PNS if actions are required.

2.1.1 Structure

Most nerve cells have three main structural elements: cell body, dendrites and axon. The cell body, also known as *soma*, contains nucleus, and other typical cell organelles such as lysosome and mitochondria. Dendrite and axon are generally called nerve fibers, which mean any neuronal extension that emerges from the cell body. Dendrites are small branched extensions, which serve as input for neuron. Neurons can have only one axon, which serves as output, meaning it delivers nerve impulses towards other neurons' dendrites, muscles, or gland cells. Axon is long and thin cylinder-like structure, which connects to the cell body at axon hillock. Between axon hillock and axon itself is a junction called trigger zone, where nerve impulses arise. Structures of different neurons can be seen in Figure 1.

Size of neuron cell body varies from 5 μm to 135 μm [9]. Dendrites are usually branched directly from the cell body, but a neuron can also have only one dendrite. Length of an axon can vary from less than 1 mm to even 1 m or more. Axon diameters can vary a lot: the smallest can be found from mammalian brains [10], where unmyelinated cortical axon diameter varies between 0.08 and 0.4 μm and the biggest known axon is squid giant axon with diameter close to 1 mm. Rat hippocampal neurons have axon diameter of 3–5 μm.

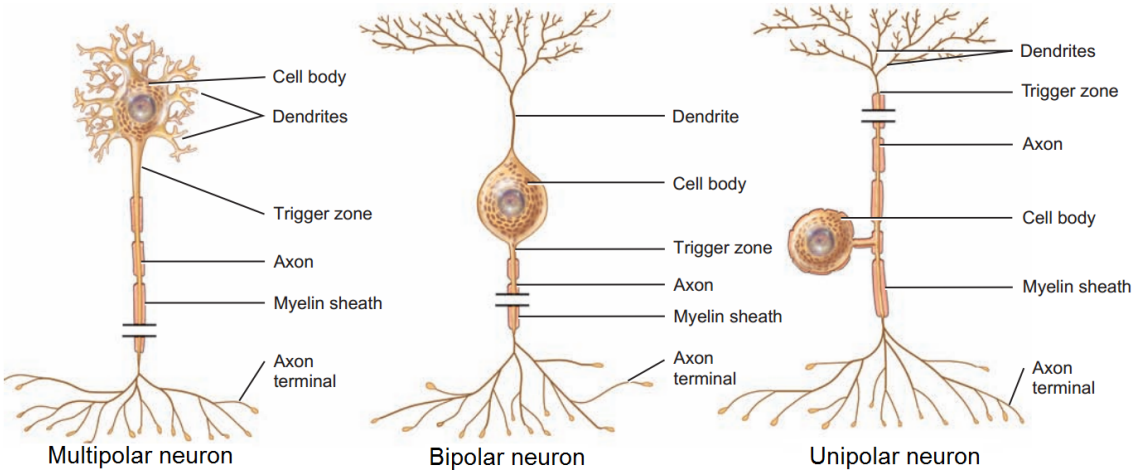

Figure 1: Different types of neurons [9, p. 419]

2.1.2 Functions

The main function of a neuron is to transfer electrical signal from dendrites to the end of the axon [9]. The dendrites receive the signal in chemical synapses. Presynaptic neuron delivers neurotransmitters to synaptic cleft, where neurotransmitters can diffuse to neurotransmitter receptors located at receiving dendrite. Neurotransmitters change the membrane potential, and can create postsynaptic potentials, which eventually can trigger axon potential in trigger zone. Axon potential propagates through axon with ionic currents, which mean that the membrane's ion channels open in segments, one after another, propagating the changed membrane potential forward. When the axon potential reaches the end of the axon, it releases stored neurotransmitters into synaptic cleft.

2.1.3 Axonal studies

Axon is important since it has functionality of transferring messages for long distances in very short time. Longest axons in humans can extend from the toes all the way to the lowest parts of the brain [9]. Along this path, there are many joints, muscles and other parts of the body which cause physical forces to the axon. As one can imagine, human body is full of neurons and their axons, and as for example, the signal from sense of feeling from the skin is transported by axons. Due to the importance of neurons, neurotrauma is widely studied field.

One of the most important aspects of neuronal study is axotomy, which means cutting or breaking the axon. How do neurons survive when their axons are cut or broken? Central nervous system (CNS) is vital for multicellular animals, and traumatic brain injuries (TBI) are the leading injury-related cause of death and permanent disability. Another arising field of study is axon stretching, which can eventually lead to axotomy [11, 12, 13]. Stretching is considered to be a good model for neuron trauma, and therefore more sophisticated devices for research are developed [12, 14, 15].

Before the axon could be isolated, studying axotomy was particularly hard due to the fact that the cultured neurons grew everywhere and axons were directed to all directions in the growth dish. When axon could be isolated [16, 17], performing the axotomy became rather simple. There are multiple methods to manipulate the axon in a way that it breaks. Simplest would be using knife or scalpel and cut it in half. Other ways include stretchable membrane, which can be actuated for example with pneumatic pressure [18], mechanical pulling force [19], or compressed air [20].

2.2 Devices for neuronal study and stimulation

Nerve cell studies are quite different compared to studies of other cell types, mainly due to presence of the axon. As the axon provides the key functionality for the nerve cell, it is preferred to study axon and the cell body separately. When neurons are grown in standard cell culture well, the axons grow to every direction and connect randomly to other neurons. Different staining methods make it possible to dye separate neurons, and therefore it is possible to distinguish separate cells which are adjacent to each other.

However, there is a constant need for new tools for testing the boundaries. These include the use of different drugs, introduction of other cell types, and changing the growth environment with different cell culture platforms. These neuron culture devices manipulate the world which the cell senses, meaning either culture dish material is changed or forces affecting the cells are added. These devices can be manipulated with pneumatic pressure changes, physical pull/push forces, electric forces, magnets and with many more.

The idea of compartmentalization was first described by Robert Campenot in 1977 with so called 'Campenot chamber' [16, 17], and similar work was carried out by Klostermann et al. and Ivins et al. with 'modified Campenot chamber' [21, 22]. One type of compartmentalization chip was introduced in 2003 by Taylor et al. [23]. They built a chip with soft lithography methods which had two compartments separated with axon guiding channels (Figure 2). After few days of incubation, axons grew into the channels and even all the way to the other compartment. Later on, Taylor et al. [24, 25] used similar design in their microfluidic local perfusion (μLP) chamber. Peyrin et al. [26] used compartmentalization in order to form axon diodes. In their chip, the axon growth is physically blocked with channels which are narrower from one end, therefore blocking the axon growth from that end.

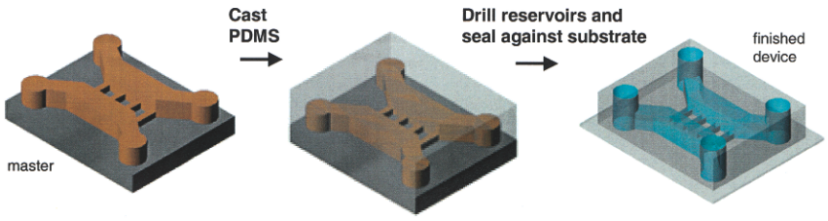

Figure 2: Compartmentalization chip made by Taylor et al. The small channels are too narrow or low for cell bodies, so only axons can grow into them. [23]

To further develop the idea of compartmentalization, Honegger et al. [27, 28, 29] developed multiple devices where it is possible to guide axonal growth with AC electric field (Figure 3). They also used the microfluidic channels to block neuron soma migration into the channels, thus allowing only axons to grow in the channels.

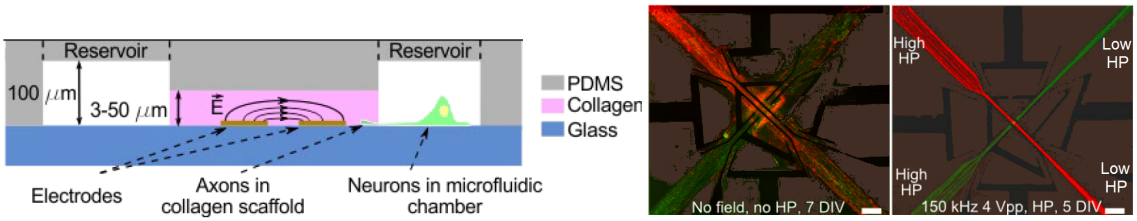

(a) Axon guidance with AC electric field

(b) Axon "beam" focusing with electric field

Figure 3: Axon isolation devices by Honegger et al. [27, 28, 29]

One axon isolation design is made by Jokinen at al. [6]. They used it in their axon isolation electrophysiology chip. The chip design consists of two round fluidic reservoirs, which are connected to each other through microchannels. The dimensions of the chip design are presented in Figure 4. In their work, Jokinen et al. used three-layer design for their device, where the axon isolation chip made from PDMS was on the bottom against a glass slide. Two other PDMS pieces were inserted on top to increase fluidic volume of the reservoirs. After culturing cells in the device, the two topmost layers were peeled off (PDMS supports reversible and waterproof bonding) and the cultured neurons went to electrophysiology studies.

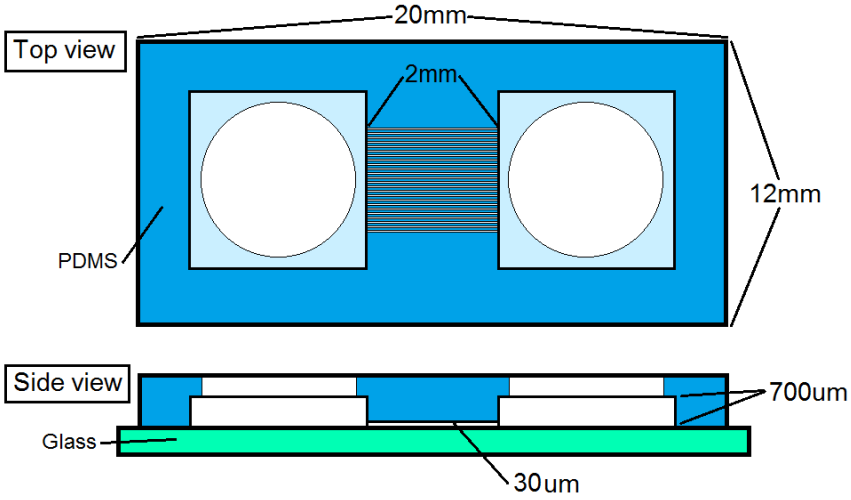

Figure 4: Critical dimensions of the axon isolation chip. The reservoirs are connected with 34 microchannels with width of 7.5 μm and height of 30 μm. [6]

2.2.1 Microfluidics

Whitesides [30] describes the field of microfluidics as following: "It is the science and technology of systems that process or manipulate small (10^{-9} to 10^{-18} liters) amounts of fluids, using channels with dimensions of tens to hundreds of micrometers." Microfluidics has many advantages compared to disadvantages, and new microfluidic systems are developed intensively in academic studies (Figure 5). It has also reached moderate stage of commercialization [31].

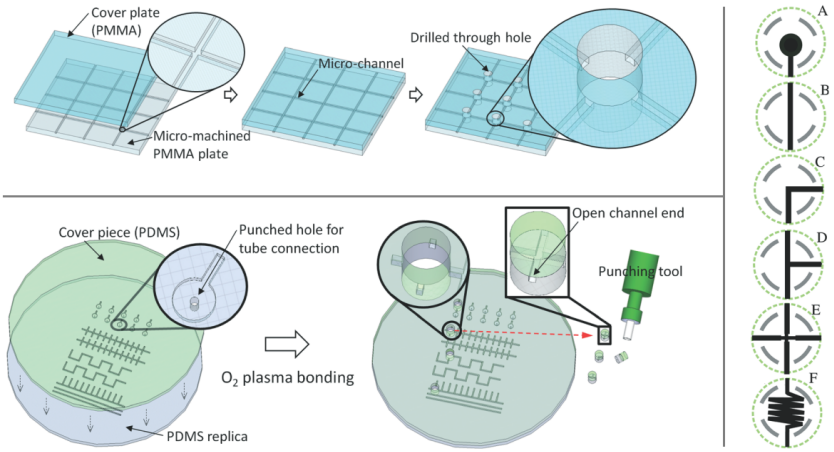

Figure 5: Do-it-yourself microfluidic system. The setup has grid of channels in PMMA substrate with holes in the channel intersections. PDMS cylinders with channels are inserted into the holes and new microfluidic setups can be created. [32]

Field of microfluidics started as tool for chemical analysis [33], as one key feature is the needed sample size. When the amount of sample/reagent is reduced to nano- or femtoliters, more sophisticated tools for imaging and measurement are needed. Applications using laser for stimulation and detection has improved the resolution, and single cell analysis is possible [34].

In microfluidic world, all phenomena observed in macroworld do not apply. For example, a river flows forward, but the water itself has lots of small vortexes and turbulence; if one pours carton of milk into the river, it will be mixed in no time. One revolutionizing phenomenon in microfluidics is laminar flow. Let's consider a channel system shaped as letter Y (Figure 6). Two different colored liquids are introduced from the inlets and they meet in the intersection, they do not mix, but continue to flow side by side. Because the flow is laminar, the mixing is caused only by diffusion of molecules and particles from one fluid to another. Also due to this effect, special micromixers and structures causing fluid lamination are invented to speed up the diffusion. Other important characteristics for microfluidics are capillary filling (which will be used in axon stretching application), electro-osmotic flow (EOF), and importance of material surface energies. There are many dimensionless numbers that tell useful information about microfluidic system at hand.

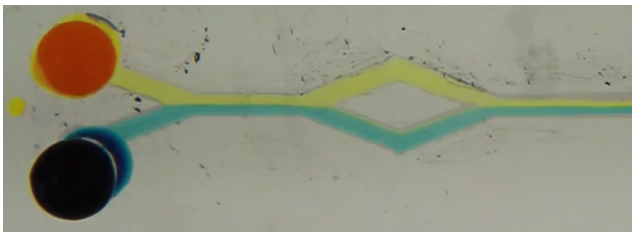

Figure 6: Two channels combine to form Y-junction. Due to laminar flow, the colored fluids do not mix. [35]

Reynolds number Reynolds number is a dimensionless ratio of inertial forces to viscous forces:

$$Re = \frac{\text{inertial forces}}{\text{viscous forces}} = \frac{\rho v L}{\mu} \tag{1}$$

where ρ is the density of the fluid (kg/m^3), v is the mean velocity (m/s), L is a characteristic linear dimension (travelled length of the fluid; hydraulic diameter when dealing with river systems) (m), and μ is the dynamic viscosity of the fluid (Ns/m^2 or kg/ms).

With Reynolds number, one can determine if the fluid flow in the system is laminar or turbulent. Low Reynolds number indicates to laminar flow where viscous forces are dominant and high Reynolds number leads to turbulent flow as the system is dominated by inertial forces. Re < 10 means flow is laminar and Re > 2000 means flow is turbulent. Between 10 and 2000 the flow is in between; laminar flow with increasing turbulent characteristics.

Weber number Weber number is dimensionless number that is used in analyzing fluid flows when there is an interface between two different fluids. It becomes especially handy when dealing with multiphase flows with curved surfaces. The equation for Weber number is

$$We = \frac{\rho v^2 l}{\sigma} \tag{2}$$

where ρ is the density of the fluid (kg/m^3), v is its velocity (m/s), l is its characteristic length, typically the droplet diameter (m), and σ is the surface tension (N/m).

Weber number can be thought to be strongly dependent of the ratio between fluid's inertia to its surface tension. The quantity is used in analyzing thin film flows and the formation of droplets and bubbles.

Ohnesorge number Ohnesorge number is a dimensionless number, the ratio between Weber number and Reynolds number:

$$Oh = \frac{\mu}{\sqrt{\rho \sigma L}} = \frac{\sqrt{We}}{Re} \approx \frac{\text{viscous forces}}{\sqrt{\text{inertia} * \text{surface tension}}} \tag{3}$$

where μ is the liquid viscosity, σ is the surface tension, ρ is the liquid density , L is the characteristic length scale (typically drop diameter), Re is the Reynolds number, and We is the Weber number. Ohnesorge number is useful in studying droplet formation for example in ink jet printing.

2.2.2 Cell stretching on chip

Researchers have done a lot of work in the field of cell stretching, and the fabricated setups vary a lot even though the main purpose is the same. Kreutzer et al. [36] introduced a cardiac cell stretching device working with pneumatic actuation. The device was made from glass and PDMS, and when vacuum was introduced inside a PDMS chamber, the cell growth membrane stretched and the cardiac cell culture was affected. Nakashima et al. [37] fabricated an SU-8 (negative photopolymer capable of forming even 500 μm high structures) based device with complex mechanical actuation principle. The device's base function was to stretch cell culture, which was grown on top of stretchable PDMS membrane. When a slider was pushed with microneedle, the pushing force was directed to both ends of the cell culture membrane and stretching occurred. Chang et al. [19] built a microfluidic PDMS stretching chip which was actuated with a linear translation stage. The chip included microchannels parallel and perpendicular to the stretching motion. Nerve cells were grown and studied in both channel types.

One cell stretching design has made it through commercial stage: Flexcell [38]. This design relies on vacuum pump and a flexible membrane on top of a loading post. Lubricant is injected on the loading post and the membrane with cultured cells (from muscle, lung, heart, vascular vessels, skin, tendon, ligament, cartilage, and bone) on top of that. An airtight chamber is brought around the membrane, and when vacuum is introduced around the loading post, the membrane is deflected and the part of the membrane which is on top of the loading post with lubricant is stretched with the cells [38, 39]. Schematic working principle of the device can be seen in Figure 7.

Axon stretching on chip is a new idea, and there are not many publications from this area [41, 42]. The principle is as simple as the name suggests: to find a method how only the axon is stretched, but not the soma area. The problem of isolating the axon has now been solved, and there are multiple methods available (microchannel dimensions [6], hydrogel [43], collagen scaffolds [29]). Chang et al. [19] made a chip and translation stage which stretches the whole cell culture, and Desmaële et al. [41] describe many MEMS-devices (microelectromechanical systems) which actuate either single cells or even cultures of thousands of cells. These different devices use magnetic or electric fields, laser trap system, electrothermal or electrostatic microactuators or constricted channels. Sasoglu et al. [42, 44] have published a way to stretch axons with polymeric microbeam array and Kamotani et al. [45] describes cell culture stretching by deformation of substrate, which both are important features in novel axon stretching chip presented in this thesis. Closely related research is done by Dolle et al. [18], where axons between brain slices are stretched by pressure.

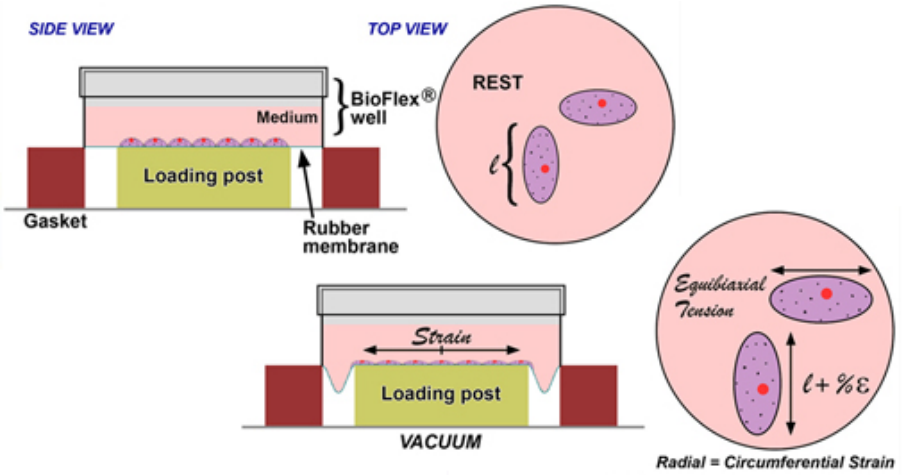

Figure 7: Commercial Flexcell device. The device performs stretching of flexible membrane by applying vacuum around loading post. [40]

2.3 Elastomer materials in microfluidic devices for neuronal studies

In 1907, the first demonstration of growing cells outside organs was provided by Ross Harrison [46]. The used platform was a glass dish, and since then engineers and biologists alike have searched new methods and substrates for cell culturing. Nowadays such culture is considered routine, and materials like polystyrene (PS), polydimethylsiloxane (PDMS), polymethylmethacrylate (PMMA), Teflon, cyclo-olefin copolymer (COC) and thiol-enes are considered standard materials [47]. These materials have their own unique properties which are compared in Figure 8. As can be seen, there is no universal material which has best properties in all fields of science. Therefore, two new materials to the list are introduced and applied in cell culturing: off-stoichiometry thiol-ene (OSTE) and off-stoichiometry thiol-ene-epoxy (OSTE+).

The reason why engineers and biologists alike are interested in different material selections is that the two fields have started to overlap. Biologists need devices and applications, where different structures and patterns are fabricated or material properties modified for the study of variety of cell properties like growth, responses and differentiation (for example shear stress studies on cell adhesion [48]). Engineers have knowledge of fabrication of microfluidic systems, and growing interest for all possible applications for the systems and materials [30]. Microfluidic systems are nowadays essential part in the study of novel functions of cell assays.

Microfluidics has been concentrating on proof-of-concept structures for several years [49], and recently more and more working lab-on-a-chip applications have been invented [30, 50]. These proof-of-concept structures include valves, active and passive mixers, regions for optical analysis, intersections, filters, and so on. In each scheme, there are plenty of different solutions how they have been implemented, for example valving. Valves can operate by air pressure, pneumatic pressure, magnetic actuation, chemical reaction, capillary filling or by many other reactions [51, 52]

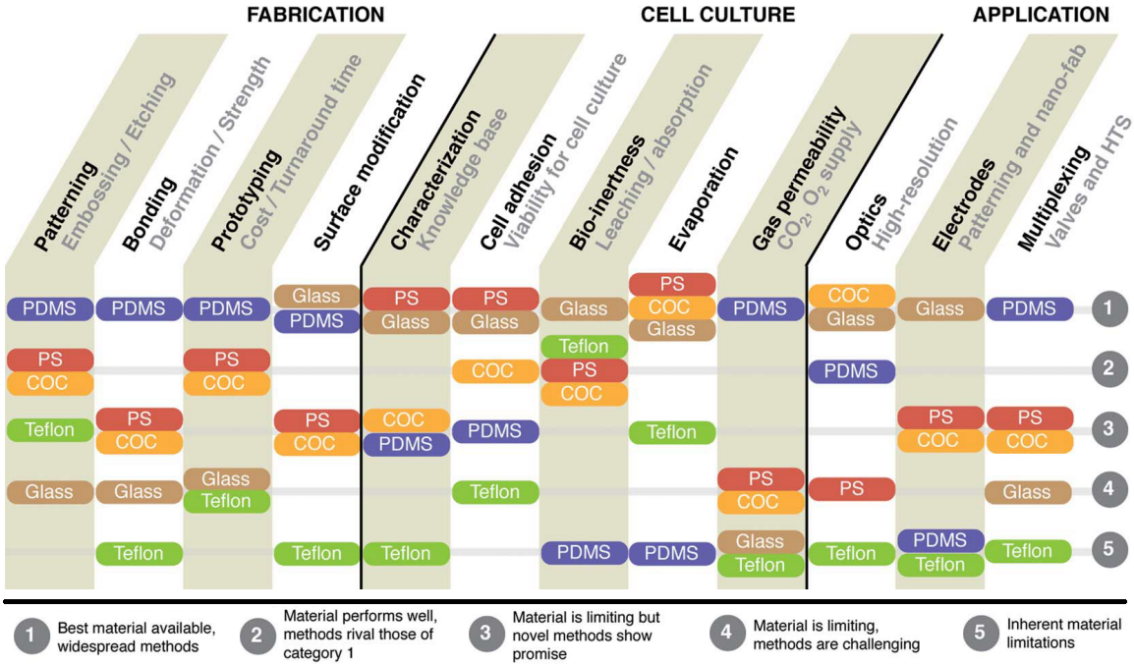

Figure 8: Comparison of strengths and weaknesses of materials used in microfluidic cell-based devices. The comparison chart is divided into three categories: the ability to fabricate microsystems, the ability to perform cell-based experiments and the potential for integrated micro-engineering applications. [47]

Lab-on-a-chip (LOC) concept integrates inlets, reservoirs, channels, mixers, valves, analyzing areas, reactors, filters and outlets, and still their size can be less than a bottle cap, but they perform reactions as efficiently as or even more efficiently than their macroscale counterparts. Many different structures can be seen in Figure 9, including 3-D basketweave channel structure in PDMS with channels crossing under and over each other [53] and coiled channel around straight one [54]. Laminar flow is commonly thought as positive phenomenon in small capillary channels, but efforts have been made to overcome laminar flow and mix reagents inside the channels. Examples of this kind of structures are alternating whirl mixer [55] and asymmetric, double-T, tangential and TTree mixer [56]. To actuate the liquid flow, capillary filling can be used as a pump in microfluidic system [57] or in electrospray nozzle to spray the sample into mass spectrometer [58].

Sieves and filter structures can be used to sort out big particles out of small ones, and this also applies in sorting of red blood cells out of white blood cells (Figure 10a) [59]. Bose et al. had different kind of approach when sorting out the cells, and they introduced a cell sorting device based of surface chemistry (Figure 10b) [60].

As the amount of biological samples increase in lab-on-a-chip designs, one can start thinking of organ-on-a-chip (OOC) devices, where functions of organs are implemented. Lung-on-a-chip has a functioning design (Figure 11a) [61, 62, 63], but also other organs like eye [64], vein [65], kidney (Figure 11b) [66] and even brain [67, 68] have their microfluidic chip versions.

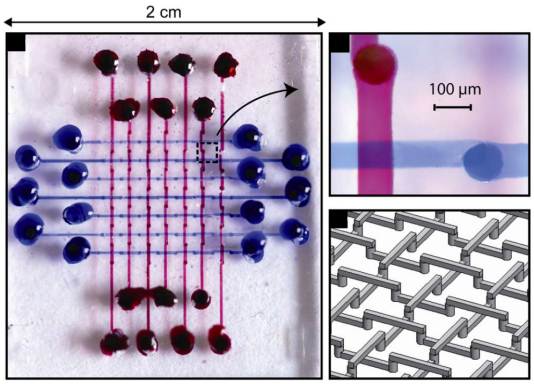

(a) 3D basket structure. [53]

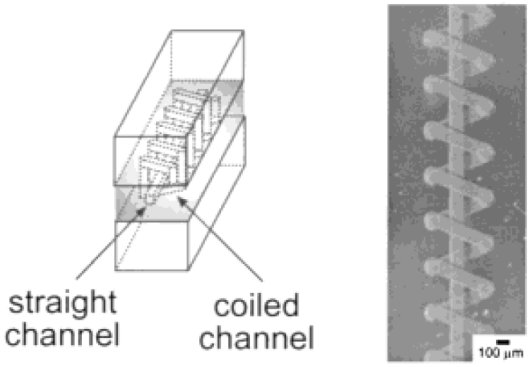

(b) Coiled channel. [54]

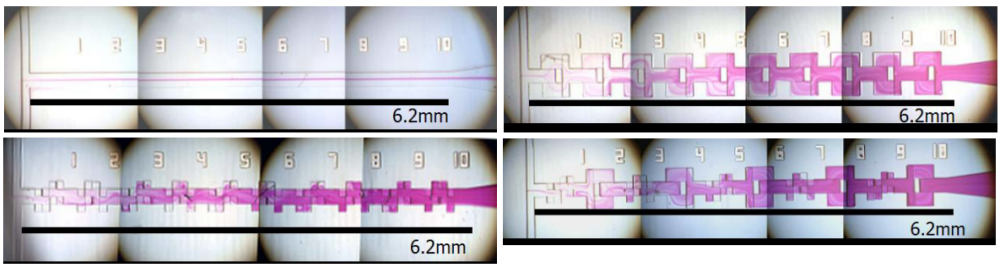

(c) Laminating whirlmixers. [55]

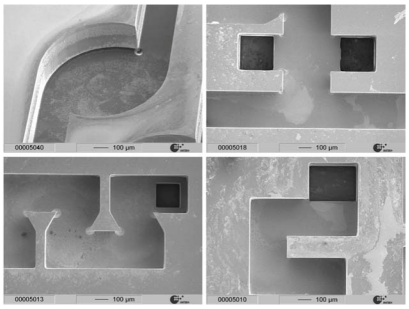

(d) Laminating mixer structures. [56]

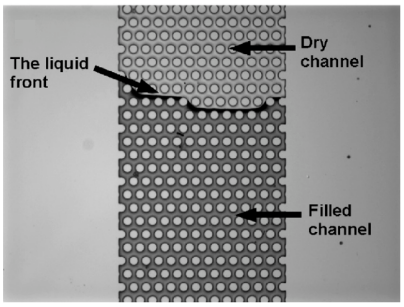

(e) Capillary filling. [58]

Figure 9: Microfluidic devices can have many different structures made from polymers, silicon etc. a) and b) show different 3D channel designs with overlapping channels. Figures c) and d) present structures which can be used to laminate flow to enhance diffusion. e) Presents capillary filling is channel filled with pillars.

2.3.1 Polydimethylsiloxane

Polydimethylsiloxane (PDMS) is a polymeric organosilicon compound (silicone), which is the most widely used silicon-based organic polymer [53]. PDMS has been the central material for microfluidics for the past fifteen years due to its many attractive properties like optical transparency (down to wavelengths of 240 nm [6] or 280 nm [69]) and chemical inertness, and it is non-toxic [70] and non-flammable [47]. PDMS has its roots all the way in 1899 when Frederick Kipping did research in silicone chemistry, including siloxanes [47, 71]. Since then it has found its way into various applications. In addition to microfluidics, it is also used in contact lenses,

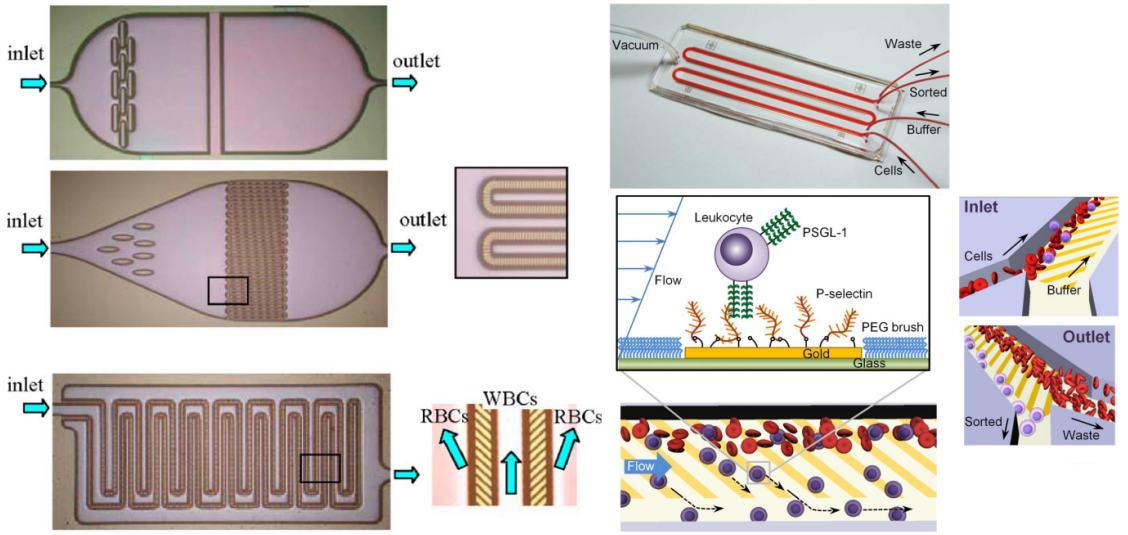

(a) Blood filter structures. [59] (b) Blood separation. [60]

Figure 10: Cell sorting structures. a) Presents different filter structures and b) shows how leukocytes are filtered from blood with aid of P-selectin guides.

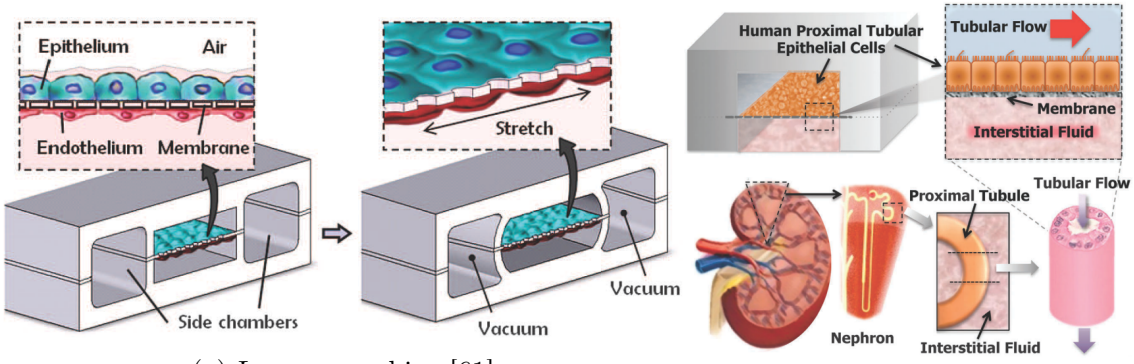

(a) Lung-on-a-chip. [61] (b) Kidney-on-a-chip. [66]

Figure 11: Different Organ-on-a-chip structures implemented with microfluidic methods.

medical devices, shampoos, lubricating oils and in food (it has E-code of E900).

PDMS is attractive to microfluidics especially because it allows fast fabrication of prototypes, but also batch processing is possible. One of the most used technique in microfluidics is replication molding [6, 54, 69]. In this method, a master mold is fabricated as negative of the desired patterns. If one wants to create a PDMS-pillar, the master mold must have a hole with same dimensions. Before curing the pre-polymer liquid can be poured on top of a master, and after thermal curing, PDMS will transform into elastomeric solid with optical transparency in the shape of desired pattern.

Johnston et al. [72] made research of PDMS Young's modulus in respect of

curing temperature. They concluded, that curing temperature radically changed the physical properties of PDMS, as Figure 12 shows [72].

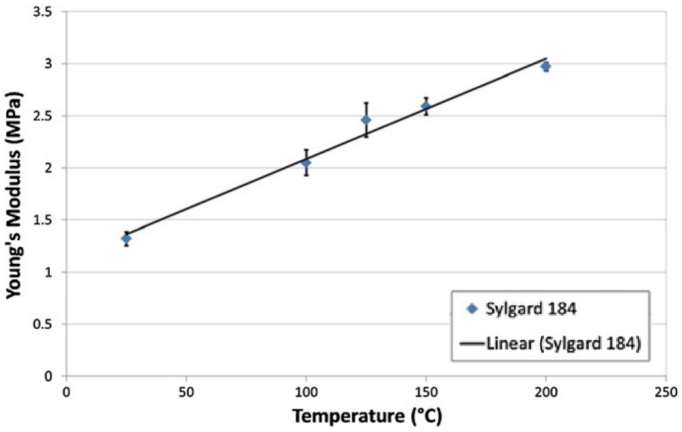

Figure 12: Young's modulus for 10:1 PDMS with varying curing temperature. [72]

Wang et al. [73] made another study of PDMS. They examined the Young's modulus in respect of mixing ratios, all the way from 5:1 to 33:1. Their results can be seen in Figure 13.

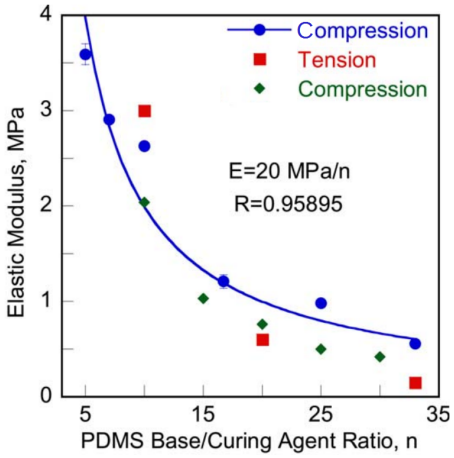

Figure 13: Young's modulus for PDMS with different mixing ratios. Curing time is constant 65°C. Blue line shows the results from Wang et al., red and green dots are results from other studies for comparison. [73]

PDMS is transparent, which allows optical measurements with microscopes and lasers, and it is compatible with biological samples like cells. The bulk properties can be tailored by varying the ratio of two precursors, and adding extra particles of materials is trivial because of inertness of PDMS. One prominent property of PDMS is its waterproof sealing, either temporarily on permanently. The temporary waterproof bonding is due to adhesive properties of elastomeric solid. PDMS is

self-adhesive, meaning it can adhere to almost any surface without external adhesives. In microfluidics, the most used materials for bonding are glass, polystyrene and PDMS itself. If pressure tolerance is needed, one can bond PDMS pieces permanently without added adhesives or glues. PDMS can be treated with oxygen (O_2) plasma, which activates silanol (Si-OH) groups on the surface of the material. These activated groups create strong bonds with silicon (Si-O-Si) in glass or other silane groups in PDMS [69]. Oxygen plasma treatment makes the surface of PDMS also hydrophilic, which enhances the coating properties that are needed in cell culturing. Untreated plain PDMS is hydrophobic by nature; therefore different coatings might need surface activation by plasma.

According to some studies, PDMS might have some adverse effect in cell culturing. These effect are deformation, evaporation, absorption, leaching of uncrosslinked oligomers and hydrophobic recovery [47]. These effects are now discussed in detail.

Deformation When PDMS is used for a valve or a pumping membrane, the deformability is indeed a must. But when the material is used for microchannels or reservoirs, the compliance may be a problem. As other materials, like thermoplastic polystyrene, can deform in the bonding step due to temperature, PDMS can deform dynamically in response to pressure change. Higher pressure in channels or reservoirs may bulge the material, or if aspect ratio is bad, the structures can collapse and even block whole channels accidentally, because they cannot support their own weight (sagging).

Evaporation Gas permeability of PDMS is a known property, and it is an important advantage for cell culture applications. This is because the cells need the transportation of O_2 and CO_2 from cells through PDMS, especially in long-term cell cultures without fluidic flow. The permeability of gases can become a significant problem when macroscale cell cultures are shifted into microscale, as even small amounts of evaporation may cause drastic change in volumes, concentrations, chemical balances or critical gradients. All these effects can cause problems like osmolarity shifts that affect cell differentiation. PDMS is highly permeable to water vapor, which causes particularly challenging mode of evaporation, that occurs through bulk PDMS. In a closed system, water vapor evaporation may cause bubbles inside the system. Air bubbles can propagate, block liquid flow or lyse cells, which can lead to data loss or ending of experiments prematurely. The problem can be alleviated with parylene coating of PDMS surface [74], which effectively decreases evaporation effect. Other alleviation methods are humid outside environment [47, 75] and sacrificial liquid reservoirs adjacent to main cell culture media [75].

Absorption As PDMS can have evaporation through the bulk, it also has effect of absorbing small molecules inside the bulk, a phenomenon which is not present in glass or thermoplastics (they are only subject to surface adsorption). Clearly this can be an issue in cell culture studies, where absorption of signal or other molecules is not desired, as it lowers the concentration of molecules reaching the cell. Microscale

structures and devices provide better sensitivity than macroscale, but the gain can sometimes be tempered because of absorption of molecules into PDMS.

Leaching of uncrosslinked oligomers When PDMS is cured, it still contains some residual uncrosslinked polymer chains, which can diffuse freely within the bulk material. When the PDMS is in contact with liquid, leaching of these oligomers into the solution can occur. This can be a serious problem in cell cultures, if one wants to study cell membrane signaling and molecule trafficking, as the oligomers can attach to the cells. Leaching can also occur after absorption. If small molecules, like pluronic F127, are embedded inside bulk PDMS, they can later leach out in ethanol bath [Heikkinen, unpublished data].

Hydrophobic recovery As PDMS is hydrophobic by nature, it is common practice in laboratories to modify the surface properties with oxygen plasma. Reason for this modification can be bonding with dissimilar material, allowing surface functionalization with molecules, or facilitation of microchannel filling and cell culturing. Since PDMS has its silicon backbone, it has similar surface chemistry to glass, and is therefore attractive material for surface modifications. But PDMS has the ability to diffuse polymer chains from bulk to the surface, and therefore they can replace the created hydroxyl groups and recover the hydrophobicity [76]. This hydrophobic recovery can occur in matter of hours, giving hydrophilic PDMS a limited shelf time, which is a problem if one wants to fabricate devices in mass-production or the device must be transported from laboratory to another. Another problem may be partial microchannel filling due to hydrophobic resistance or cells grown on the surface may experience dynamic change in hydrophilicity, which can ultimately lead to loss of cell adhesion and mechanotransduction. The adverse properties of PDMS are shown in Figure 14.

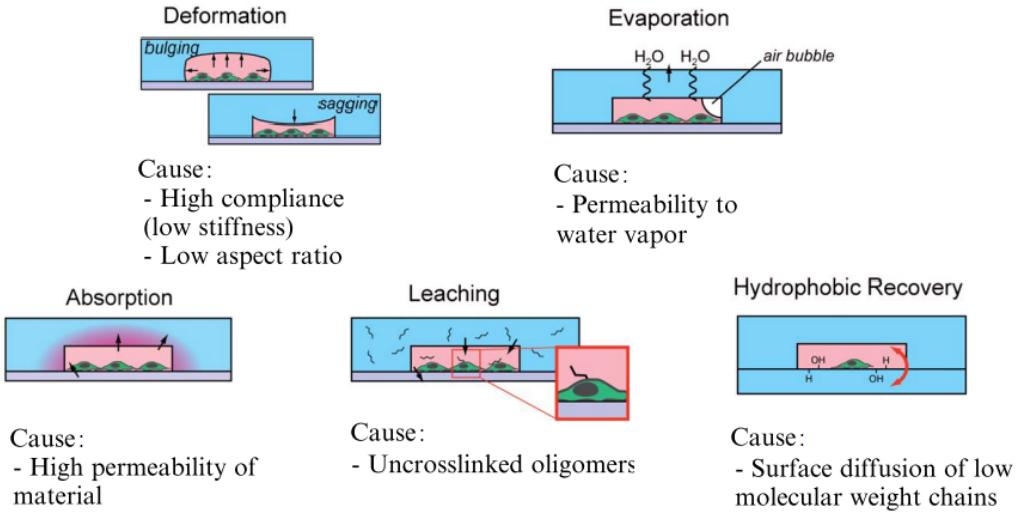

Figure 14: Adverse PDMS-properties. [47]

2.3.2 Thiol-enes

Thiol-enes are a set of compounds which can create solid polymers. As the name suggests, it has two different substances mixed, organic molecules with thiol-groups (sulphur-hydrogen) and ene-groups (carbon-carbon double bond). When these two molecules are brought close to each other, they tend to create a bond, since they have matching structural and chemical composition. This bonding is called "click chemistry" [77].

The field of thiol-ene chemistry has gained interest for the fabrication of lab-on-a-chip devices. Thiol-enes are usually mixed with 1:1 ratio, when there are no excess of reactive groups of thiol nor alkene, but all monomers "click" and form copolymers creating elastomeric solid [78, p. 27]. Thiol-enes are usually made from two monomers, one with thiol functional groups $xR_1–(SH)_m$, and the other with allyl functional groups $yR_2–(CH_2–CH=CH_2)_n$, where x and y indicates the number of monomers in the compound [2]. Usually with stoichiometric systems the number of functional groups are almost the same, xm = yn, meaning all the functional groups have reacted with each other, and almost none are remaining. This means that the surface of the material is stable and not chemically active.

With thiol-enes, two reactive groups are present [79]. Thiol has characteristic sulphur-hydrogen bond, which is relatively weak and allows plethora of chemical reactions. Allyl has reactive carbon-carbon double bond, "ene". Even though the bonds are reactive, they do not tend to react spontaneously with each other, but they require external energy to start the reaction [80]. The external energy source is usually thermal or photonic. Figure 15 shows the thiol-ene radical reaction. First, the thiol R-SH group is radicalized to form R-S*, and when -ene group is introduced, the C=C double bond breaks and carbon is connected to sulphur. This compound lacks of one hydrogen atom, which is taken from another thiol-group (energetically favorable) to form complete thiol-ene molecule and R-S* radical which continues the mechanism of "clicking" with other -ene groups [79, 80, 81].

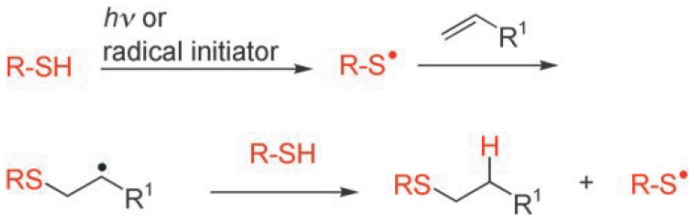

Figure 15: Scheme showing click-chemistry reaction with thiol and allyl. [80]

As the reaction goes on, more and more polymer chains are formed and solid material is created. Proper thiol-ene material should be resistant to solvents, it must have good elastic properties and it should be biocompatible.

2.3.3 Off-Stoichiometry Thiol-Ene (OSTE)

In the previous chapter, the thiol-enes are mixed in 1:1 ratio, meaning the ratio between thiol and ene groups is stoichiometric. When the ratio is changed, it is called off-stoichiometric, and in the case of thiol-enes, new properties can be achieved with the excess of one functional group. This section describes what OSTE is, and what and how its properties can be modified.

Off-stoichiometry thiol-ene (OSTE) has been developed to replace PDMS. It is said that OSTE has many beneficial properties compared to PDMS [30]. First of all, the lab-on-chip products developed in research laboratories cannot reach commercial production, if they are made of PDMS. This is because PDMS require long thermal curing steps, individual handling and is hard to standardize (meaning that the commercial products need invariable surface chemistry and mechanical strength). These properties make the PDMS hard to scale up. The bonding of PDMS into other substrates of materials is done with oxygen plasma. Downside with plasma bonding is that the plasma treatment can destroy surface chemistry of materials, and therefore it can also destroy the material biocompatibility or some other ways weaken the polymer properties.

Off-stoichiometry thiol-ene (OSTE) has many features similar with PDMS, like elastomeric composition and transparency, but at the same time many features can be tailored. This new kind of material can overcome the problems faced with PDMS, with improved solvent resistance, and with gas permeable and gas blocking abilities.

Materials When thiol-ene is made off-stoichiometric (xm $\neq$ yn), it has excess of either functional groups, both in bulk material and on the surface. This excess of one functional group also defines the properties of the material. One must take into account, that the monomers used should not homopolymerize, meaning that the functional groups should not react with themselves.

Properties OSTE has many good properties, which makes it suitable material for microfluidic systems. One important property is the possibility for tailoring the properties of the material. It can be made hard as thermoplastics (Young's modulus 1740 MPa), soft as low density polyethylene LDPE (Young's modulus 250 MPa) or something in between [2, 78, 82]. When OSTE is made with excess of thiol, the resulting material is soft and rubber-like. When the material is made with excess of allyl, it is hard and stiff. The excess ratios usually vary from 0 to 120 percent, and the properties of the material vary with the ratio. Figure 16 shows two different pieces of OSTE, one with excess of thiol and one with excess of allyl.

Before the monomers in OSTE click, the prepolymer has low viscosity, and it can be molded to master structure. When the liquid polymer is exposed to ultraviolet light, thiol and ene groups click. Photoinitiator can be used to enhance the curing. Resulting material is solid and elastic with excess of one monomer on the surface [2].

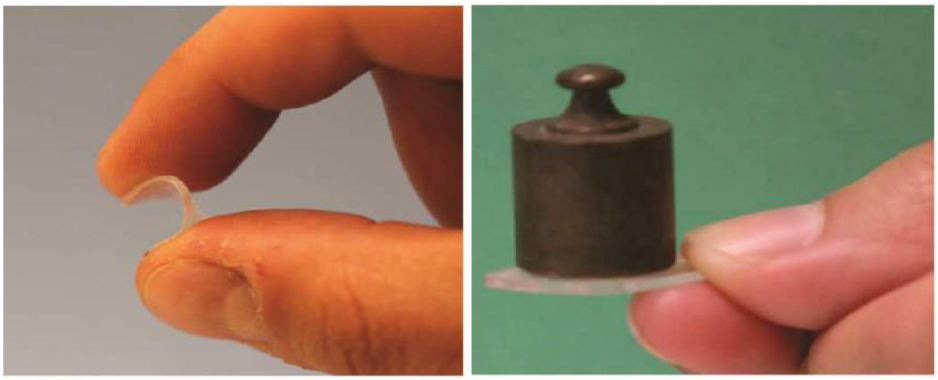

Figure 16: Two different kinds of OSTE. Left: excess of thiol, right: excess of allyl. Thiol excess makes the polymer soft, while allyl excess makes OSTE stiff. [82]

Many microfluidic devices need different surface chemistries, so also OSTE needs to be versatile with surface modifications in order to replace PDMS. OSTE can be made in a way that the surface contains allyl or thiol-groups, but also properties like water contact angle (hydrophobicity and hydrophilicity) and attachment of foreign molecules on the surface need to be considered. With PDMS, the water contact angle can be modified with oxygen plasma treatment, but the effect stays only for few hours. With OSTE, the surface treatment can be made permanent by attaching molecules, like polyethylene glycol PEG, on the surface [2]. The contact angle can be changed when hydrophobic or hydrophilic molecules are attached. The attachment step is simple; the OSTE surface needs to have excess of one monomer on the surface, and the desired molecule need to have the other monomer attached to it. This way allyl-thiol connection is possible. When the molecule + monomer compound is poured on the surface, the allyl and thiol functional groups find each other, but do not connect. Only after UV-cure, the bonding on the functional groups takes place. Carlborg et al. changed contact angle of thiol excess OSTE from natural 76° to 97° with vinyl-PDMS and 48° with allyl-PEG. They also modified OSTE with allyl excess from natural 68° to 77° and 35° with thiol-PDMS and thiol-PEG respectively.

Bonding Bonding of macroscopic objects with click-chemistry is possible with same reactions which were described earlier [77]. Bigger elements can be bonded when smaller units join together. The smaller units are usually functional groups of monomers on the surfaces. In order for click-bonding to occur, the functional groups between two surfaces must be matching type. Good example is thiol and vinyl silane [83]. A silicon wafer can be surface modified to have vinyl-functional group R-CH=CH_2 on the surface, and then thiol-excess OSTE can be brought into contact with the silicon-vinyl surface. When the interface is exposed to UV-light, the small units will click and form covalent bond. Same principles apply when thiol excess OSTE is bonded to allyl excess OSTE.

Like with PDMS, also click-bonding can be easily done in wafer scale. This gives OSTE one more great feature for commercial production. With click-bonding,

used monomers can be selected to be biocompatible, and there is no need to raise temperature in any step, meaning ready-made features and surface modifications will stay unaffected [83]. Also, the biofunctionalization for the channels can be made before bonding.

Biocompatibility As the aim is to grow neurons on the surface of OSTE, biocompatibility has to be studied. Errando et al. [84] reported cell growth (HEK293A and HEP G2) on two different OSTE polymers and polystyrene petri dish (Figure 17). The two different OSTE polymers contained different monomers (OSTE 3T4A and OSTE $4T_13A$, where number before T and A indicates number of thiol and allyl reactive groups, respectively), and they were also tested with different ratio of thiol excess (number in brackets is excess of thiol in percents). A PS petri dish was half-filled with OSTE, and the other half was left untreated. Also different thiol-excess OSTE-polymers were tested with polystyrene well plate (Figure 17 right). In this test, a bit different OSTE monomers were used: OSTE $4T_23A$. Photoinitiators were added on all samples.

	Day 1	Day 2	Day 3	Day 6
Control (PS)	Proliferation	Proliferation	Overpopulation	Overpopulation
OSTE4T$_1$3A[50]	Viable	Low viability	Low viability	Low viability
OSTE4T$_1$3A[70]	Med. viability	Low viability	Low viability	Dead
OSTE3T4A[50]	Viable	Viable	Proliferation	Proliferation
OSTE3T4A[70]	Viable	Viable	Viable	Proliferation

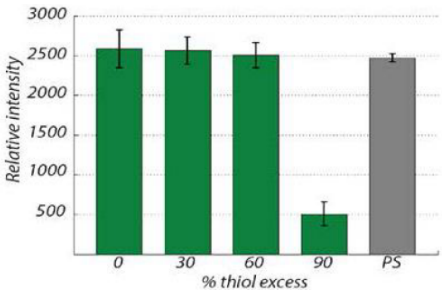

Figure 17: Biocompatibility studies of different OSTE materials. Left table shows HEK293A cell viability on the surface of different OSTE composition. Right hand chart shows HEP G2 cell viability on OSTE $4T_23A$ with different thiol excess ratios. [84]

The results show that cells do grow on different OSTE materials, but compared to standard polystyrene petri dish, differences could be found. Results show that OSTE with thiol excess ≤ 60 % provides good environment for cells to grow. Errando et al. reported that they found effects of leaching in their experiments: when they grow the cells on a petri dish which is half filled with OSTE, the cells have lower viability on both halves compared to control sample. They suggested that this is because the OSTE material leaches some monomers or photoinitiator to the medium and therefore affect the growth on polystyrene side also.

2.3.4 Off-Stoichiometry Thiol-Ene Epoxy (OSTE+)

As OSTE contains some limitations, the polymer compositions has been developed further, and novel material consisting of thiol-ene-epoxy (OSTE+) has been invented [78, p. 67 - 68]. OSTE+ has three major components, thiol, allyl and epoxy.

By varying the ratios of these components, one can choose between numbers of different properties to the final product. One can choose to fabricate stiff and hard OSTE+, or by changing the used epoxy molecule, create rubbery OSTE+ [78]. Rubbery OSTE+ has all the advantages of previously presented OSTE+, e.g. rapid fabrication procedures and biocompatible bonding, while possessing the flexibility similar to PDMS. Table 1 shows comparison between PDMS, OSTE and OSTE+.

Table 1: Comparison of PDMS and OSTE(+) properties

	PDMS	OSTE	OSTE+
Color	clear	yellowish	yellowish
Young's modulus (MPa)	0.5 - 4	250 - 1740	0.5 - 1740
Water contact angle	105°	70°	73°
Structure	Si backbone	Thiol & Allyl	Thiol, Allyl & Epoxy
Curing time (approx.)	2 h	60 s	60 s + 30 min

OSTE+ is cured in two steps, where the first step is the same as with OSTE; material is poured in liquid form into master and photocured, leading thiol and ene groups to click. Curing step is usually enhanced with photoinitiator. Resulting material is soft and rubbery, which has active surface layer that can be functionalized. Second curing is thermal (enhanced with thermal initiator), where the material transforms into stiffer polymer by reaction of thiol and epoxy functional groups (see Figure 18), allowing easy handling of the created chip without need of bonding to stiff lids made from glass, for example.

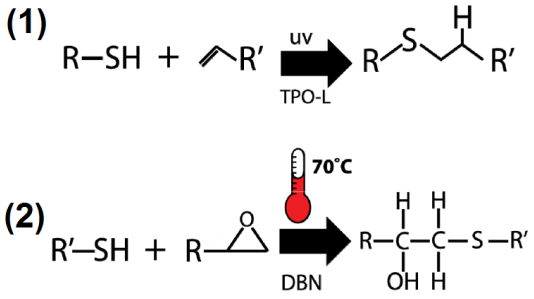

Figure 18: OSTE+ dual curing process first binds thiol and ene groups to form previously presented thiol-ene. Second cure binds thiol and epoxy. [85]

The addition of epoxy increases the glass transition temperature of the material [78, p. 67]. The new material has also reduced the leaching of uncured material, which was major issue with PDMS [78, p. 69-70] and OSTE, as discussed above. This new material can also be bonded in room temperature, and the bond can withstand moderate pressure in high temperatures, which enables the use of material on PCR thermocycling [78, p. 71].

The dual cure system of OSTE+ is specifically developed for microfluidic applications. OSTE+ can be patterned with soft lithography methods, and it creates strong and biocompatible dry bonds to almost any surface during LOC creation [85], while it mimics the properties found in thermoplastics. These properties allow even rougher machining of OSTE+, like drilling, without tearing the material apart.

2.4 Microfabrication techniques

In 1959 physicist Richard Feynman had his famous talk "There's plenty of room at the bottom" [86]. The message was that we must advance in technologies which manipulate micro- and nanoworld in order to proceed further in science. The standard tools like drills, lathe, milling tool, bandsaw and CNC (Computer Numerical Control) have been developed quite far, and they have reached the accuracy of less than one millimeter. But when we are talking about features of couple of micrometers, these tools are not usable. Thus, new methods of fabrication have been adopted. These methods include different deposition methods of thin films, chemical etching, ion bombardment, photolithography, and imprint/molding techniques. With these methods, structures with size less than a micron can be fabricated and functionalized, and complex lab-on-a-chips can be made to have a surface area of a coin.

2.4.1 Lithography

The lithography technique is a method where certain pattern is transferred from mask to substrate with the aid of light (usually ultraviolet light). The method includes photoactive polymer, which is to be patterned, a mask, which has the initial pattern to be copied, a substrate, which holds the photoactive polymer while it is being exposed to UV-light, and developer, which dissolves unneeded parts of the polymer [87, p. 93-126] [88]. The complete lithography process is shown in Figure 19 with positive and negative resist options.

The key part of lithography is photoactive polymer, usually known as photoresist, or just resist. The resists vary with viscosity, chemical composition, and the minimum feature size they can acquire, but most of all, they can be either positive resists or negative resists. Positive resist will be dissolved into developer in the areas which are exposed to UV-light, and negative resist will dissolve from the areas which are not exposed. Resists are used as etch mask (wet and dry etching), in lift-off, as protective coatings, and as a glue.

In microfabrication technology, the substrate used is usually silicon wafer, but other substrates are also possible (like glass). The substrate wafer is placed into a spinner, which rotates the wafer at high speed, and due to rotational forces, it expels the resist away from the wafer surface. There are some adhesive forces between the polymer and the substrate, and therefore thin layer of resist is left on the surface after spinning. Some of the solvent in the resist is evaporated away by baking the wafer for a short time.

While the resist is solid on the surface of the wafer, it is usually exposed to UV-light. Exposure can be done to the whole thin film, but if some patterns and features

are desired, a mask should be used. The mask consist simply from transparent parts and opaque parts, and when the film of resist is exposed to UV-light through this kind of mask, the photoactive molecule in the polymer activates and either weakens the polymer structure (positive) or hardens the structure (negative). After this step the resist is immersed into developer to get rid of the weaker parts of the resist, and finally physical structures are present of the surface of the substrate. Standard processing for positive tone photoresist AZ 5214E with viscosity of 24 cSt (centistokes) is spin coating with 4000 rpm, soft bake 50 s in 110°, exposure to UV-light for 3 s, development in AZ 351B developer for 1 min, and post bake for 50 s in 120°. This yields approximately 1.4 μm thick film.

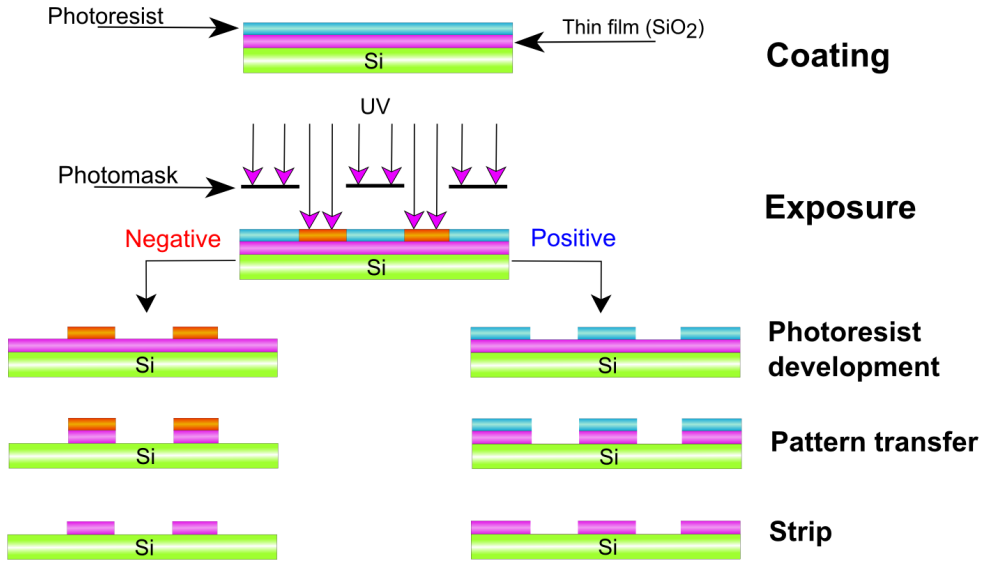

Figure 19: Basic process steps in lithography.

2.4.2 Molding techniques

The most common technique in microfluidics is molding technique, as with it one can produce microchannels and complex microfluidic systems with high precision, fast, and inexpensively. In molding technique, a 3D master mold is fabricated with lithography methods, for example solid photoresist pattern of top of a silicon wafer can act as a master mold. Then, liquid polymer is poured on the master. Most common polymer is PDMS, which acquires the 3D structures accurately, and it can be peeled off easily. As one can understand, the structure on the molded polymer will be inverse from the patterns in master, so when fabricating the master, care must be taken to choose mask and photoresist correctly [54, 87, p. 209-212].

Also PDMS can be used as a master. If some patterns are needed in OSTE or OSTE+, it is possible to use PDMS as a master for that, since OSTE can be easily peeled off from PDMS. The same molding technique is used when PDMS is used in imprinting. First, the PDMS is molded in master, then coated with imprinting

molecule/material and finally the PDMS piece is stamped on the surface where imprinting is done [85, 89].

2.4.3 Sputtering

Thin film vacuum deposition methods can be roughly divided into two categories, deposition due to chemical reactions (CVD, chemical vapor deposition) [87, p. 50-52] and physical deposition (PVD, physical vapor deposition) [87, p. 48-50]. Sputtering is PVD method, and it is needed while fabricating the multielectrode array chip, which will be introduced in later chapters. In sputtering, a target wafer is placed into vacuum chamber, and desired sputtering material (sputtering target) is placed above the wafer. Then, inert gas like argon is introduced to the chamber, and it is ionized with RF-source. The created ions are accelerated towards sputtering target with such a power that the surface atoms from the target are released as a vapor into the chamber. As the vapor spreads into the chamber, it starts to condensate to all possible surfaces, also on the surface of the wafer. Since deposition in the chamber walls should be minimized, the gap between target and wafer is kept small [87, p. 428-430].

2.4.4 Wet etching

Etching procedures can be also divided into two categories, wet and dry etching. Wet etching is a process, where etched wafer is immersed in etchant liquid. The etchant has compounds which react with molecules on the wafer, for example aluminum can be etched in a mixture of phosphoric acid and nitric acid H_3PO_4:HNO_3. The mixture works in a way that the thin native aluminum oxide Al_2O_3, which is present in every aluminum thin film, is etched away with phosphoric acid, and then the nitric acid oxidizes exposed Al layer [88, p. 81-82]. The continuous process of Al oxidation and dissolving oxide continues as long as there is material available.

2.4.5 Reactive Ion Etching

Dry etching methods usually include etching by gas/vapor or high energy molecules. In reactive ion etching (RIE), gas/vapor is ionized into plasma in vacuum chamber, and then the ions are accelerated towards wafer surface with RF field [87, p. 132-134]. The gas is chosen accordingly so that the ions react with surface molecules, detaching them from the bulk. When gas compound is excited into plasma, the atoms detach and ionize.

When ions hit the wafer surface, they bombard it and create bonds with atoms located in the surface. If the newly created bond is stronger than the bonds in the etched material, the created molecule detaches from the surface and it can be pumped out. While reacted gas is pumped out, new etching gas is pumped in at the same time; therefore the etching process is continuous. Schematic picture of RIE chamber is presented in Figure 20-left.

2.4.6 Inductively Coupled Plasma Reactive Ion Etching

One form of RIE is inductively coupled plasma RIE (ICP-RIE). In ICP-RIE the plasma is formed with radio frequency powered magnetic field far away from the wafer, and then it is guided with small bias voltage to bombard the wafer [87, p. 428]. Due to ICP, very high concentration of plasma can be achieved, and the plasma can be controlled before it is directed towards wafer. Capacitively coupled plasma (CCP) is used to guide the formed ions to wafer surface, which then react in the same way as in RIE process, and the formed compounds are pumped out of the chamber. As seen in Figure 20-right another difference between RIE and ICP-RIE chambers is that in ICP the wafer holder/chuck is usually cooled with liquid nitrogen or helium.

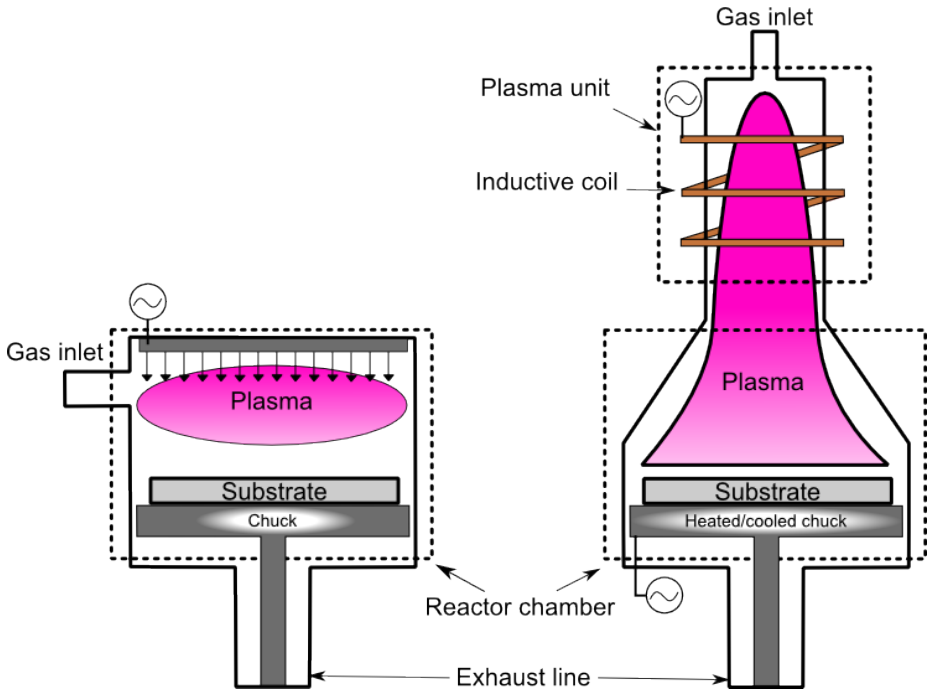

Figure 20: RIE-chamber vs ICP-RIE-chamber. Conventional RIE chamber is so-called parallel plate reactor, where one plate is powered and another is grounded. In ICP-RIE reactor, the plasma is formed remotely with magnetic field and then directed to wafer with another power source.

Wet etching enables batch processing, as multiple wafer can be immersed in etchant at the same time [87, p. 130-132], whereas in dry etching usually only one wafer is processed at a time. Wet etching is usually a cheap option compared to dry etching methods, as it does not require vacuum chambers or complicated electronics and mechanics. It usually produces isotropic etching profiles, where etching of material proceeds to all directions forming a shape of a sphere. But there are also wet etching processes, which have anisotropic etching profile, like silicon etching in potassium hydroxide KOH, which is restricted by slow etching crystal planes in silicon structure. With plasma etching, usually anisotropic etching

profile is acquired, but with some gas – material combinations isotropic profile is also possible. Figure 21 show different etching profiles formed with different etching methods. Each subfigure presents a situation where part of the etched material is covered with etch mask, like patterned photoresist. Etch mask protects the area under it from etchants, keeping it intact. This step is illustrated in Figure 19 as pattern transfer.

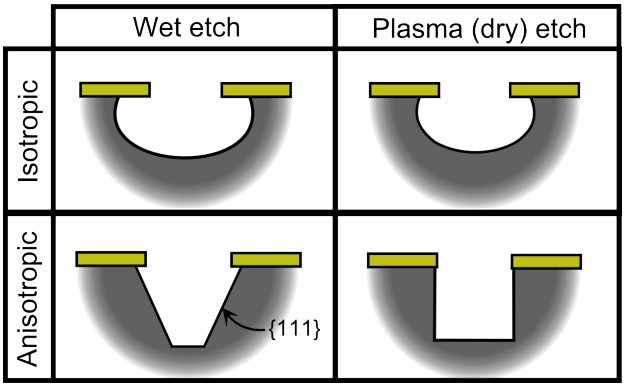

Figure 21: Common etching profiles. Yellow area represents etch mask, which is considered to be inert for corresponding etch method. The exact shape of isotropic profile depends on process details.

2.5 Multielectrode Array chips

Multielectrode array (MEA) is a set of electrodes packed close to each other, and it is usually made either on a planar surface as growth platform [90, 91, 92, 93] or as an invasive needles [94, 95]. The purpose of such array is to measure multiple locations in one sample, like in brain slice [90, 93] or in the invasive method, the MEA is punched into the brain itself. In some cases, individual neurons and their axons can be measured with underlying multielectrode array [91]. In such cases, the axon is isolated from the neuron soma by a channel structure. This kind of setup allows optical inspection through transparent channel materials like PDMS, but also electrical measurement through electrodes located at the bottom of the axon isolation channel.

Material selection is an important factor in MEA devices. Neurons must grow smoothly on the substrate, but also on the conductive electrode. Substrate material can be made from many biocompatible materials available, like from polystyrene or glass. Electrode material must possess good electrical properties in order to deliver signals without noise, but also it must be biocompatible, and axons must attach to it to create electrical contact. One such electrode material is indium tin oxide (ITO), as it is biocompatible, has good electrical properties, and it is transparent [91, 96]. Other possible materials are biocompatible metals like platinum, titanium or gold [96].

Different MEA structures have long been used in research, but the fabrication of such a device requires access to microfabrication tools. Since the array layout in planar electrodes resemble a lot of each other, couple of designs have made their way to commercial level, thus allowing research groups without microfabrication tools to carry out electrical studies for brain slices etc. One such device is MED64 (Figure 22) [97], which has 8 x 8 array of electrodes separated with varying distance (150 μm to 450 μm). Conducting path is made from ITO, center electrodes (which are in contact with studied sample) and outer electrodes (which are used as output) are coated with platinum black (biocompatible, has higher surface area than normal platinum layer [98]). Passivation layer on top of conducting path is acrylate resin [97].

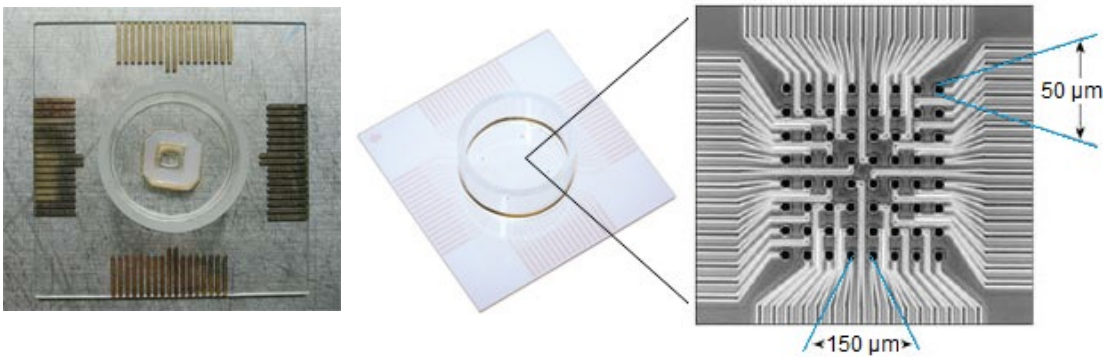

Figure 22: A commercial MED64 multielectrode array (MEA) chip. The chip is 5 cm square, and is has 64 electrodes reaching the center. The round structure is culture well for living samples. [97, 99]

2.5.1 Carbon as electrode material

New materials are searched all the time, and one promising candidate for biological measurements is carbon. Carbon is known to form really strong structures with many elements, and it is naturally biocompatible. Different carbon compounds have gained a lot of attention after discovery of multi-walled carbon nanotubes (MWCNT) in 1991 by Iijima et al. [100].

Carbon atoms form strong bonds with each other. Probably the best known carbon compound is diamond, where all carbon atoms have single bonds with other carbon atoms (called sp^3 bond). Due to this bonding type, carbon atoms are equally distributed around each other, in a form called tetrahedral (see Figure 23). Diamond is known to be the hardest available material, and this is because of strong C–C bonds.

Another commonly known carbon compound containing only carbon atoms is graphite. Graphite is a multilayered structure, where the layers are sheets of carbon, known as graphene. Graphene structure resembles benzene ring, where carbon atoms form circle with single and double bonds (bond type known as sp^2), but in graphene, the rings are connected to each other to form large 2D network with a shape resembling honeycomb (Figure 24) [102]. Graphene is the structure where

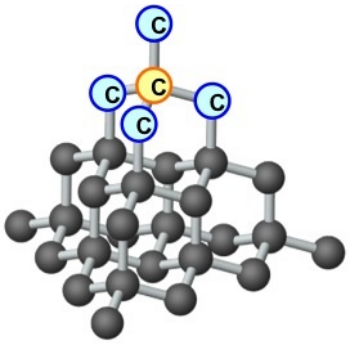

Figure 23: Tetrahedral bonding type of carbon. Every carbon atom is bonded to four carbon atoms with single bond, called sp^3 bond. Diamond is known to have this composition. [101]

carbon nanotubes are formed by rolling sheets of graphene. If graphene is rolled in 3D, it will form fullerene, a ball shaped structure made entirely of carbon atoms. Graphene and its different structures are presented in Figure 24.

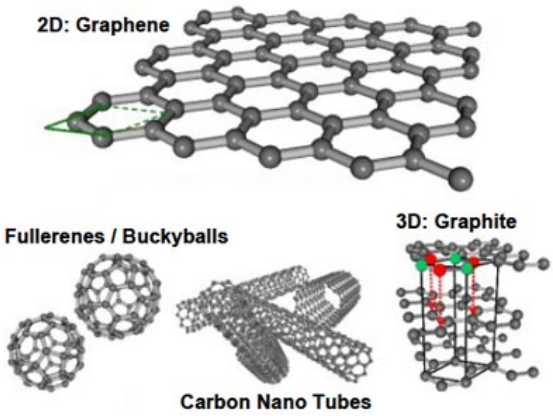

Figure 24: Graphene and its structures. Graphene is sp^2 bonded carbon in 2D form. Multiple layers of graphene is known as graphite, rolled graphene is nanotube and ball shaped graphene is fullerene. [103]

Even though the different structures are made from one kind of atoms only, they still possess very different properties. The electrical properties of carbon nanotubes can be either metallic or semiconducting, depending of its chirality (angle of rolling graphene sheet into CNT). Graphene is studied intensively since its rather recent discovery. Graphene and CNT are studied in transistors, fullerenes as encapsulating structures, and diamond as electrical insulator. All of the carbon compounds (except thick layer of graphite) are known for their high hardness, low-friction coefficient, good wear resistance, optical transparency and chemical inertness.

2.5.2 Nanocrystalline carbon properties

In ternary phase diagram (Figure 25), carbon type known as nanocrystalline carbon (NCC) is located on the line between sp^2 and sp^3 indicating that the amount of hydrogen is close to zero (nearly the same area where ta-C, tetrahedral amorphous carbon, is located). NCC is a mixture of these two bonding types, meaning it has diamond-like regions (sp^3) and graphene-like regions (sp^2). Depending of the ratio of these types, material properties (like electrical properties from semiconducting to insulating) can vary.

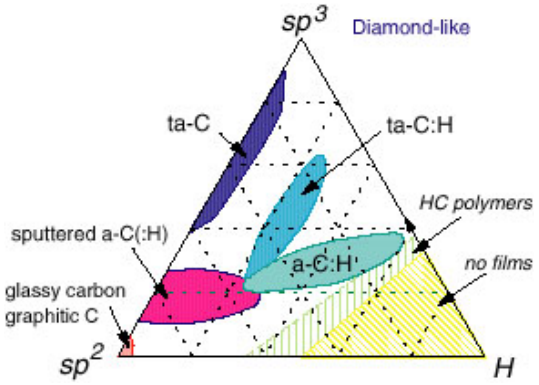

Figure 25: Ternary phase diagram of sp^2 and sp^3 bonds of carbon and hydrogen H. [104]

When NCC is considered as electrode material, sp^2 bond type is important, as it provides the conducting path for electrons [105]. NCC is mostly sp^3 bonds and it has "islands" of sp^2 bonded carbon (Figure 26).

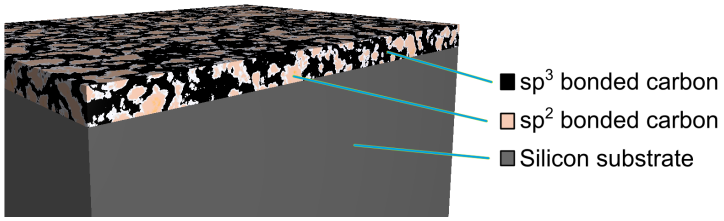

Figure 26: Illustration of what NCC film could look like on top of silicon substrate.

NCC can be deposited in multiple ways like electron cyclotron resonance chemical vapor deposition (ECR-CVD), laser ablation, arc ion plating, DC- and RF-plasma enhanced chemical vapor deposition (PECVD), RF magnetron sputtering, and close field unbalanced magnetron sputtering (CFUBM) [106, 107]. CFUBM reactor is presented in Figure 27. NCC and ta-C films contain amorphous regions, and therefore they exhibit many desirable and extraordinary properties like extremely high hardness, high density, high melting temperature, good wear resistance, low friction coefficient, chemical inertness, good corrosion resistance, optical transparency, high elastic modulus, and high electrical resistivity [105, 106, 107, 108].

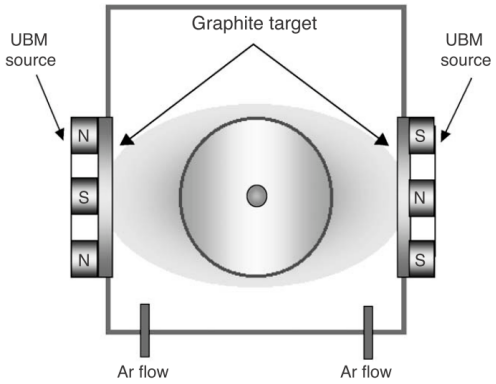

Figure 27: Schematic picture of CFUBM sputtering system. The substrate is placed in the center of magnetic field while the sputtering targets are near the north and south poles of the magnet. [106, 109]

Due to their properties, carbon compounds have found their way into applications like wear resistance coatings for metallic, ceramic and optical materials (protective layers on magnetic discs), corrosion protection, liquid and vapor transport barrier, passivation, dielectric and heat transfer layers for electronic devices, and solid lubricant [105, 106, 107, 108]. For different applications, just bare film of carbon (amorphous or crystalline) might not be enough, but patterns and features are required. Therefore patterning and etching methods for extremely hard carbon films are studied. As stated above, amorphous carbon is chemically inert, meaning that it does not form spontaneously any new chemical bonds in liquids or gases. Therefore wet etching of these films is practically impossible, and dry etching methods must be considered [110].

Techniques like focused ion beam (FIB) can be used to make grooves and patterns into carbon film, but these methods are expensive and slow (serial process). RIE is a good candidate for etching a carbon film like NCC, as it is cheaper, the whole wafer can be patterned simultaneously (parallel process), and it is relatively fast [111, 112]. When ions are accelerated towards carbon surface, they provide enough energy to break the carbon-carbon bond, but the used ions must also react with the freed carbon-atoms in order to prevent redeposition of carbon-atoms on the surface. That is why oxygen and fluorine compounds can be considered as good etching gases as they form volatile compounds with carbon [110, 113, 114]. Some general ionization, excitation and dissociation equations are presented below with standard etching gas compounds.

$$e^- + O_2 ==> O_2^* + e^- \tag{4}$$

$$e^- + SF_6 ==> SF_5^* + F^* + e^- \tag{5}$$

$$e^- + CHF_3 ==> HF + F_2^* + C^* + e^-. \tag{6}$$

When these gases are used for etching carbon, the equations are as follows:

$$C + O_2 ==> CO_2 \tag{7}$$

$$2C + SF_6 + 2O_2 ==> 2COF_2 + SO_2F_2 \tag{8}$$

$$C + CHF_3 + O_2 ==> COF_2 + CO + HF. \tag{9}$$

2.6 Magnetic actuation of an elastic membrane

Many of the devices introduced in microfluidics section had a functionality which relied on the fabricated static structures and shapes. One of these devices is the axon isolation chip made by Jokinen et al. [6] which is also used in the devices presented in this thesis. However, static structures and functions have limited operation area. Dynamic structures inside a fabricated device allow mechanical manipulation and stimulation to studied subject. This chapter introduces magnetic actuation and membrane deflection of the axon stretching chip. The chip design is first of its kind, and therefore existing calculations does not exist.

First, it is necessary to know a bending profile of an elastic membrane. The magnetic membrane deflection can be compared to membrane deflection with pressurized air (schematic shown in Figure 28a) and membrane deflection with vacuum (schematic shown in Figure 28b). The pneumatic force is initially uniaxial, but rather soon it turns into multiaxial. Vacuum actuation produces similar stretch profile as magnetic stretch chip, but it is multiaxial, whereas magnetic membrane deflection is mostly uniaxial. Pneumatic and vacuum theories cannot be used for beam fixed only from both ends, as the pneumatic force or vacuum is only valid for airtight membrane systems [115, 116, 117, 118, 119]. But these theories are good for comparison, as many cell culture stretching devices use pneumatic force or vacuum for actuation [18, 20, 115, 116].

(a) Pneumatic actuation (b) Vacuum

Figure 28: Membrane deflection profiles. a) Pneumatic force actuated and b) vacuum actuated. [116]

In respect of theories of deflection, axon stretching chip can be considered as a wide beam which is fixed from both ends (Figure 29). This simplifies theoretical calculations. Two theories need to be considered in axon stretching chip: beam which is bent with uniform load, and beam which is bent with concentrated load.

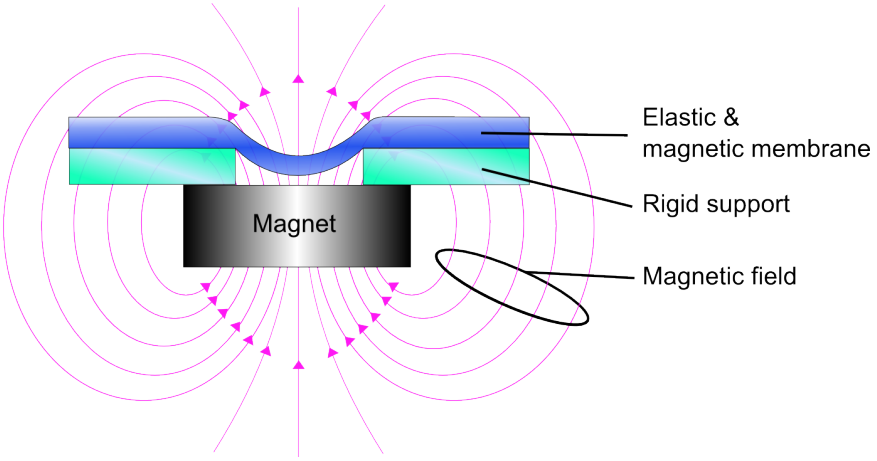

Figure 29: Magnet (grey) in proximity with magnetic membrane (dark blue). Two glass pieces (green) are used as spacers to allow only middle part of the membrane to be pulled. Purple arrows show the magnetic field orientation.

In axon stretching chip, the load can be thought to spread uniformly on whole 'beam' (Figure 30) or the load can be thought to be concentrated on single point (Figure 32). Actually, the concentrated load theory is not concentrated on a single point, but on specific area (which is small compared to total area of the beam), but to simplify the calculations, a single point model is used. The equations for uniform load are presented first.

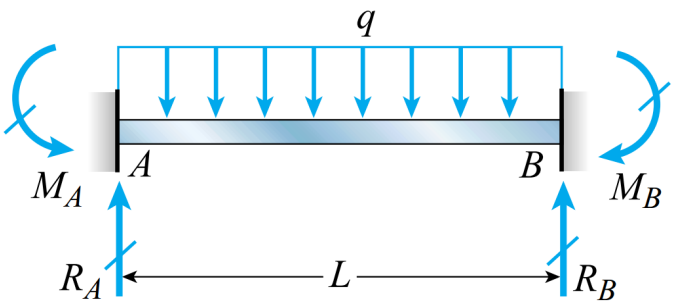

Figure 30: Uniform load on beam which is fixed from both ends. [119, p. 728]

The pulling force produced by magnet can be calculated with Euler-Bernoulli beam equation

$$\frac{d^2}{dx^2}(EI\frac{d^2w}{dx^2}) = q \tag{10}$$

where E is material Young's modulus, I is second moment of area, w is the deflection of the beam in the z direction at some position of x, x is point along the beam, and q is used load [119]. The Euler–Bernoulli equation describes the relationship between the beam's deflection and the applied load.

In the case where beam is exerted for uniform load and it is fixed from both ends, bending moment has equation (with boundary conditions)

$$M_A = M_B = \frac{qL^2}{12}. \tag{11}$$

The bending moment M can also be described as

$$M = -EI\frac{d^2w}{dx^2} \tag{12}$$

and combination of these two equations yields

$$\frac{qL^2}{12} = -EI\frac{d^2w}{dx^2}. \tag{13}$$

The point of interest is the middle point of the beam or membrane, and Gere [119] substitutes following equation for deflection at the middle point with uniform load for a beam which is fixed from both ends:

$$w_C = \delta_C = \frac{qL^4}{384EI}. \tag{14}$$

where δ_C is the deflection of the beam at the center.

Second moment of area I depends of beam's cross-section, which is perpendicular to the applied load. The loads axis must pass through the centroid C of cross-section. If the beam is directed along x-axis, and the load is applied from y-direction, the cross-sectional area is yz-plane

$$I = \int\int z^2 dydz. \tag{15}$$

In axon stretching chip, the 'beam' is rectangular, and the cross-section is illustrated in Figure 31. Y-direction is the thickness of the membrane h, and z-direction is the width b.

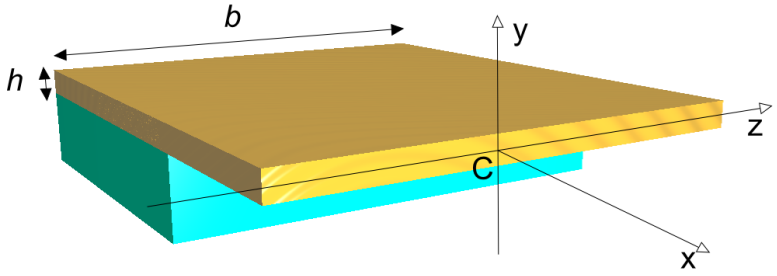

Figure 31: Schematic of the chips cross-section from the middle of the membrane. Blue part indicates the glass spacer and yellow is the polymer membrane. Illustration shows what information is needed for calculation of second moment of area. C is located at the center of the beam, h is thickness of the membrane, and b is the width of the membrane.

Second moment of area, when force comes along y-axis, can be calculated with the dimensions of the chip as follows:

$$I_y = \int_A x^2 dA = \int_{-b/2}^{b/2} \int_{-h/2}^{h/2} x^2 dy dx = \int_{-b/2}^{b/2} h x^2 dx = \frac{b^3 h}{12}. \tag{16}$$

In situation where the pulling force is concentrated on a single spot, the mathematical model for calculations changes. The schematic illustration of the situation can be seen in Figure 32, where forces M_A and M_B are moments at the fixed ends and R_A and R_B are supporting forces against load P.

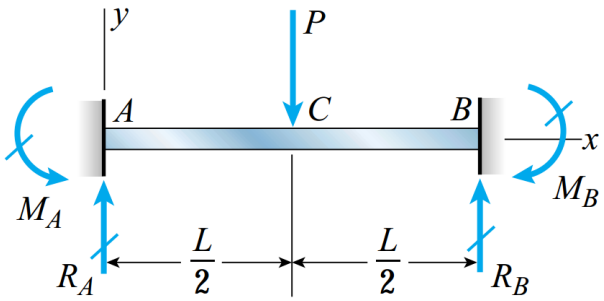

Figure 32: Schematic figure of concentrated load on beam which is fixed from both ends. [119, p. 715]

The starting point for calculations is once again the Euler-Bernoulli formula (Equation 10), which changes it's form after all boundary conditions are taken into account. The interesting point is at the midpoint where the load is located, and the maximum deflection at that point by Gere is

$$\delta_{max} = -(v)_{x=L/2} = \frac{PL^3}{192EI} \tag{17}$$

where $-v_{x=L/2}$ is the midpoint of the beam, P is concentrated load, L is length of the beam, E is Young's modulus of the material, and I is second moment of area.

The theoretical deflection curve for the beam is presented in Figure 33. As can be seen, the deflection curve is not perfect circle, but circular. This is because boundary conditions fix the ends of the membrane to be horizontal. The final stretch of the membrane is difficult to calculate for this kind of model, so the length of the arc is approximated with straight lines from fixed ends to the center. With this simplification, it is possible to get a approximate value for total strain of the membrane. The theory behind calculations is shown in Figure 34.

The maximum deflection δ_{max} is the same as variable h and membrane initial length is L, which are shown in Figure 34. The variable s is the length of the triangle, which also approximates the length of the membrane under deflection. From basic geometry, it is known that

$$(\frac{s}{2})^2 = (\frac{L}{2})^2 + h^2 \Longrightarrow s = 2 * \sqrt{(\frac{L}{2})^2 + h^2}. \tag{18}$$

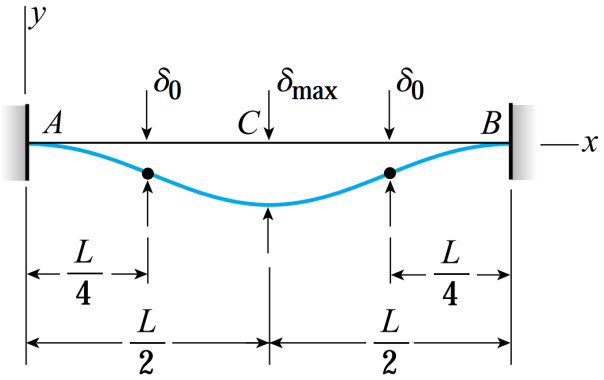

Figure 33: The deflection model with concentrated load. [119]

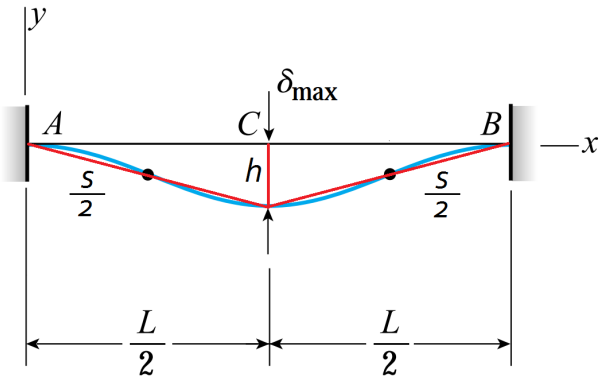

Figure 34: Approximation of deflected membrane strain can be calculated with Pythagoras equation. In the figure, h is the height of the triangle, and s is the length of the membrane.

The Equation 18 can be used when the maximum deflection δ_{max} is measured under actuation.

The abovementioned equations allow for calculation of uniform load q, pressure P by concentrated load, and resulting strain of the membrane. When Young's modulus is known, its equation can be used to calculate the force stretching the membrane:

$$E = \frac{F/A_0}{\Delta L/L_0} = \frac{FL_0}{A_0 \Delta L} \tag{19}$$

where E is the Young's modulus (modulus of elasticity), F is the force exerted on an object under tension, A_0 is the original cross-sectional area through which the force is applied, ΔL is the amount by which the length of the object changes, and L_0 is the original length of the object. The equation is formed from situation where object under tension is stretched horizontally. This equation applies also to situation where

membrane is deflected downwards, and force stretching the membrane is then

$$F = EA_0 e = \frac{EA_0(s - L_0)}{L_0} \tag{20}$$

where s is the length of the arc and e is strain of the membrane. The resulting information about forces and stretch effects can be compared to forces in different brain trauma situations. This matter will be discussed in later chapters.

3 Materials and methods

This section describes the designs of different axon stretching chips and material selections in polymers. Also, fabrication process for stretch chip and NCC MEA is introduced in detail. Finally, introduction to device actuation is given.

3.1 Chip designs

The structure of the stretching chip did not evolve out of nothing, but it is a product of multiple tryouts and efforts to improve my previous designs. First parental designs (axotomy chip and 1st version of stretching chip) are presented in the following paragraphs to fully understand the final design.

Axotomy chips schematic design is presented in Figure 35. The idea is to fabricate an axon isolation chip (Figure 4) with glass-PDMS bottom, cut the chip in half from channel region and then connect the pieces back together to achieve fluidic contact through the channels. Neuron culturing is done in one reservoir, and the axons are directed through the channels to the other reservoir. Finally, the pieces are separated from each other, which results to axotomy, since the axons attach to the bottom while they grow. The idea of the design where axon is surrounded by elastomeric material, is original, and the same idea is applied to the axon stretching chip.

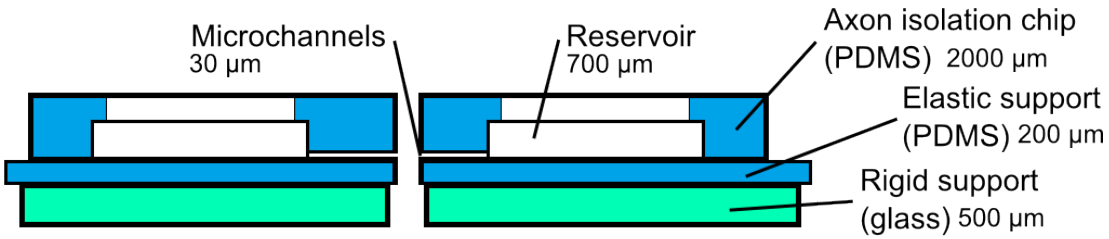

Figure 35: Schematic side view of axotomy chip. Blue parts are PDMS and green indicates glass.

As the small channels (only few microns margin for success) of axotomy chip are hard to align, different channel dimension solutions were tested. Different channel solutions are presented in Figure 36. Three different channel layouts vary the width and height of half of the channels.

My first version of axon stretching chip mimics the design of the axotomy chip. The schematic picture can be seen in Figure 37. Design consists of two glass pieces, which are connected with PDMS block. The chip is made so that there is no step between glass and PDMS pieces, and the whole bottom is permanently bonded with oxygen plasma. Final functionality is obtained by attaching the axon isolation chip introduced by Jokinen et al. [6] on top of the glass-PDMS platform. The neurons are cultured on top of the glass piece and then the axons will grow through the microchannels and reach the other reservoir. Then by mechanical pulling it is possible to stretch the axons and even reach axotomy.

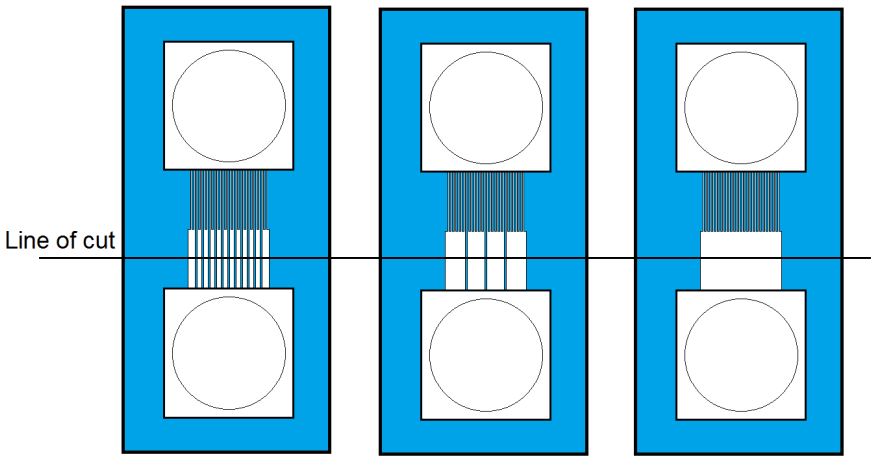

Figure 36: Different axotomy chip channel variations. One half of the channel is made larger, and after cutting the chip in two, it is easier to accomplish fluidic contact with larger channels. Black line shows where the PDMS chip is cut.

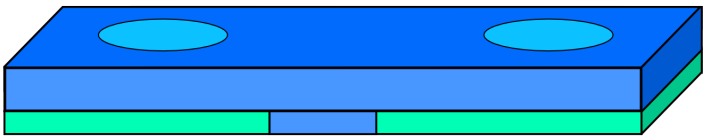

Figure 37: Stretching chips' first design. Green pieces represent glass pieces, which are connected with PDMS. Axon isolation chip is bonded on top of the chip to isolate the axons only on top of the PDMS between glass pieces. Actuation is done mechanically.

The resulting axon stretching chip is a combination of these two presented chip designs. It takes advantage of axotomy chip to have flexible polymer membrane under the cells to give mechanical support for axon guidance, and it also mimics the preliminary design of stretching chip to fill the gap between glass slides. The resulting design has a full polymer membrane over the glass gap, which acts as a substrate for axon isolation chip, but also for cell culturing. The different stages of development are presented in following chapters, as different chip designs and actuation methods can be used for different purposes.

3.2 Axon stretching chip

3.2.1 Materials

Different polymer materials were used in the stretching chip fabrication process. Table 2 shows all the needed materials for axon stretching chip.

Table 2: Materials needed in stretch chip fabrication

Material	Needed in	Chemical composition
Base agent (Complete list of containing chemicals can be found in [120])	PDMS	Ready PDMS
Curing agent (Complete list of containing chemicals can be found in [120])	PDMS	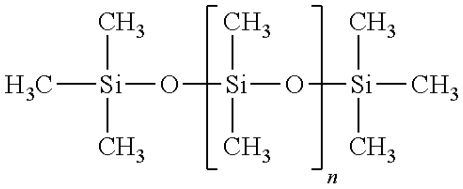 [121]
Thiol Pentaerythritol tetrakis(3-mercaptopropinate) (TMPEC)	OSTE/ OSTE+	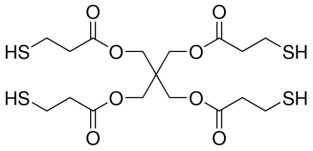 [122]
Allyl Trimethylolpropane diallyl ether (TMPDE)	OSTE/ OSTE+	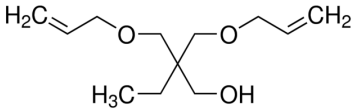 [123]
Epoxy Novolac Resin DEN 431	OSTE+	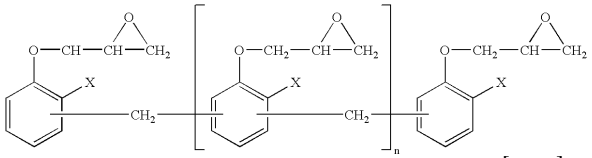 [124]
Photoinitiator Ethyl (2,4,6-trimethylbenzoyl) phenylphosphinate (TPO-L)	OSTE/ OSTE+	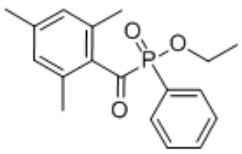 [125]
Thermal initiator 1,5-Diazabicyclo [4.3.0]non-5-ene (DBN)	OSTE+	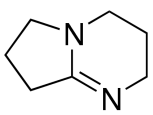 [126]

3.2.2 PDMS replication molding

Master fabrication

The master mold was fabricated on silicon wafer with standard lithography methods. First, clean <100> silicon wafer was primed with HMDS (Hexamethyldisilazane). The priming was done in vacuum/vapor priming oven Imtec Star-2000, where wafer is heated to 150 °C and then exposed to gas-phase HMDS. HMDS priming promotes adhesion between silicon substrate and resist.

Next step was photoresist spinning. Negative SU-8 50 was used for fabrication of structures tens of microns high. The resist was spun on the wafer with 4000 rpm for 30 seconds, followed by soft bake step at hotplate. Soft bake was performed in two steps; 5 minutes at 65 °C and 15 minutes at 95 °C. After soft bake the wafer was let to cool down to room temperature.

When the wafer had reached room temperature, it was ready for exposure, which was done with Süss Mask Aligner MA-6 through a plastic photomask. The photomask has pattern of channels as negative image. Hard contact mode was used while exposing with 365 nm UV-light for 16 seconds. Exposed wafer was placed on hotplate for post exposure bake at 95 °C for 15 minutes. Resist was immersion developed in 1-methoxy-2-propanol acetate (PGMEA) for 10 minutes, followed by isopropanol and DI-water rinsing and finally dried with nitrogen gun and in oven of 90 °C for 10 minutes.

For fabrication of thick structures (target 700 μm), negative resist SU-8 100 was used. The resist was spun on the wafer with 800 rpm for 30 seconds, followed by a soft bake step at hotplate in two steps; 25 minutes at 60 °C and 3.5 hours at 95 °C. After soft bake, the wafer was slowly let to cool down to room temperature.

Second exposure was done with mask which had openings at reservoir parts. Alignment was crucial, therefore alignment marks in both masks were required. The resist was exposed to UV-light for 105 seconds. Exposed negative photoresist was post exposure baked in 65 °C for 60 minutes with 4 hours ramp down to room temperature in order to avoid photoresist cracking and buckling. Finally, resist was developed in PGMEA for two hours to dissolve unexposed areas. The final master had negative structures of desired axon isolation chip: two larger blocks with microchannels between them (Figure 38).

Molding

Axon isolation chip is fabricated from PDMS with molding technique. First, the ready master mold was attached to polystyrene petri dish. PDMS (Sylgard 184 Silicon elastomer kit) was mixed from two ready-made commercial components, pre-polymer and curing agent, in 15:1 ratio by weight. PDMS mixture was degassed in vacuum desiccator and cast in master mold followed by curing in oven of 50 °C for 2 hours. Solid PDMS was cut from master and carefully peeled off. PDMS slab was further diced into individual chips with a scalpel. 6 mm holes were punched on the reservoirs with round manual craft punching tool (Eleganttang leather craft), and residual PDMS debris was washed away with isopropanol in ultrasonic bath for 2 hours, followed by drying in oven of 50 °C for 80 minutes.

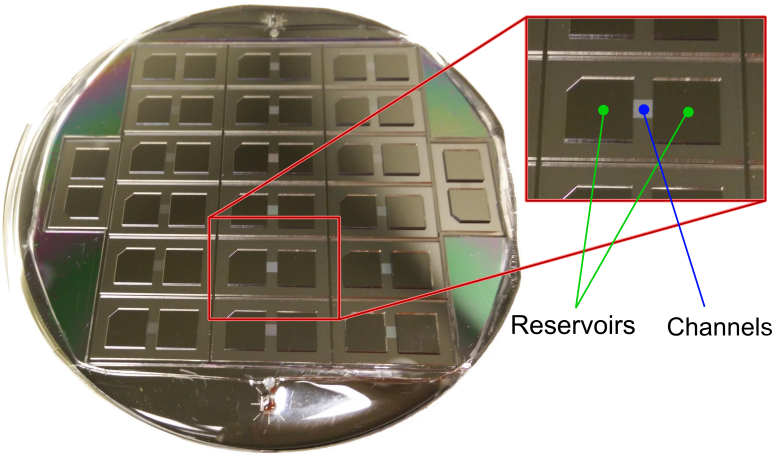

Figure 38: Silicon - SU-8 master mold for PDMS casting.

3.2.3 Full PDMS stretching chip assembly

Schematic assembly of the chip is shown in Figure 39. The glass pieces for this design were diced from 100 mm glass wafer, which had thickness of 500 μm. The glass wafer was diced with Loadpoint MicroAce 3, Series 2 dicing saw, and the size of the cut pieces were 15 mm x 12 mm. After dicing, the glass pieces were washed in isopropanol bath with ultrasonication for 2 hours and dried in oven at 50 °C for 80 minutes.

The thin PDMS membrane for the chip was done with molding technique. In order to achieve planar surface, a silicon master with SU-8 ring on the edge of the wafer was fabricated. PDMS components were mixed in 15:1 ratio by weight. After degassing the mixture, approximately 1 gram of PDMS was cast on master in order to achieve 300 μm thick membrane. PDMS was cured in oven of 50 °C for 2 hours, followed by careful peeling off and cutting into 30 mm x 12 mm pieces.

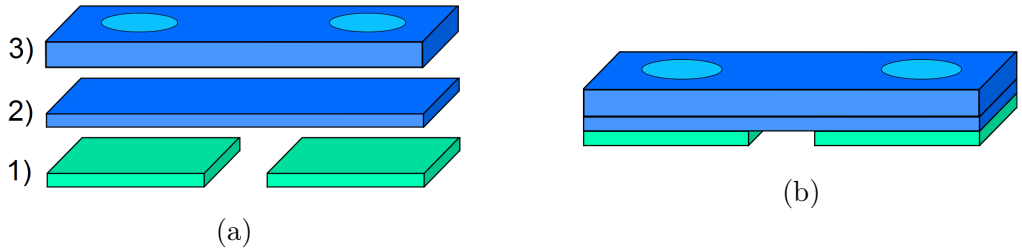

Figure 39: Full-PDMS stretch chip assembly. Green parts in figure present glass pieces, which are added to give support and allow easier handling. Cell growth reservoirs and channel walls are PDMS (blue), and the actuation is done mechanically. Layers: 1) glass 2) elastic growth membrane 3) axon isolation chip

One functional stretching chip needs two glass pieces, one membrane PDMS and one axon isolation chip. All parts were inserted in plasma chamber PVA TEPLA

PS 400, and treated with oxygen plasma (O_2 flow 800 sccm, power 800 W, time 30 seconds, frequency 2.45 GHz) in order to activate the surfaces, which makes permanent bonding possible. After plasma treatment, glass pieces were inserted into template (made from silicon and SU-8) which separated glass pieces exactly 2 mm from each other (12 mm side). The thin PDMS membrane was placed on top of the glass pieces and pressed gently to get rid of air bubbles between glass and PDMS. Last, axon isolation chip was inserted on top of the membrane in a way that the microchannels were on top of the 2 mm gap between glass pieces. Waterproof sealing was achieved by gently pressing the axon isolation chip on the membrane and getting rid of air bubbles, but paying attention not to collapse any microchannels.

3.2.4 OSTE-PDMS chip

The second design of stretching chip is similar to previously described design with PDMS membrane, but now the elastic actuation membrane is made from off-stoichiometry thiol-ene (OSTE) or off-stoichiometry thiol-ene epoxy (OSTE+). The fabrication steps for OSTE and OSTE+ are rather complicated when compared to PDMS; therefore the steps are described in detail.

OSTE Bare OSTE is made from two main components, thiol and allyl. An initiator is added to enhance curing. The steps for 40 % thiol excess OSTE-polymer fabrication are described in Table 3 and additional information can be found from Appendix A.

OSTE+ Making OSTE+ is a bit more complex than OSTE, since number of used components increases to five. Table 4 describes fabrication steps of OSTE+ (thiol excess 40 %, epoxy excess 60 %) and Appendix B gives additional details about the material fabrication.

Biocompatibility/Poly-L-lysine coating In order to make the polymer surface fully compatible with nerve cells, it had to be coated with cell attachment factor. Poly-L-lysine (PLL) was used for this purpose, as it improves cell adherence. The coating was done in multiple steps. First, the sample surface had to be sterilized. Two methods were used:

- 10 minute bath in 96 % ethanol followed by MilliQ water rinsing four times, or
- 10 minute UV-curing with 365 nm UV-light

The effect on poly-L-lysine was increased with oxygen plasma treatment, which made the polymer surface more hydrophilic and therefore greatly enhanced the adherence of PLL. Then the samples were immersed into undiluted poly-L-lysine solution and placed into incubator (water saturated, +37 °C, 5% CO_2) for 6 - 8 hours. After the coating step, samples were washed twice in PBS (phosphate buffered saline) and twice in MilliQ water. Drying of the samples were done in laminar hood by placing

Table 3: OSTE fabrication steps. Resulting polymer has 40 % excess of thiol groups.

Step	Instructions	Notes [Example 10 g]
1	Measure allyl TMPDE into glass beaker	**[4.17 g]**
2	Add photoinitiator TPO-L	0.5 % from total weight **[0.05 g]**
3	Mix thoroughly and place beaker into oven of 70 °C for 10 minutes	Liquid should turn yellowish. Let cool down before proceeding
4	Add thiol TMPEC	Amount depends on off-stoichiometry ratio **[5.83 g]**
5	Mix thoroughly and place the beaker into oven of 70 °C for 15 minutes	
6	Degas in vacuum desiccator for 5 minutes	To get rid of possible air bubbles
7	Pour liquid polymer on petri dish or master mold	
8	UV-cure for 30 seconds	If necessary, longer time can be used if OSTE is not solid
9	Cut the solid polymer into 10 mm x 30 mm pieces and peel off	Scalpel or scissors can be used
10	Rinse with DI-water, followed by short isopropanol wash and another DI-water shower	To get rid of most of the OSTE debris produced while cutting
11	Dry in oven of 70 °C for 30 minutes	To make sure no IPA is left
12	Bond the parts to form functioning stretching chip	

them on top of a sterile surface for overnight. After drying, samples are ready for cell growth experiments.

OSTE+ water contact angle was also studied. Contact angle with native OSTE+ was measured with sessile drop test, and then placed into plasma chamber. Plasma parameters were: 500 sccm O_2 flow, 800 W plasma power and duration 50 s. After plasma treatment, water contact angle was measured immediately and in 24h interval for 3 days.

Table 4: OSTE+ fabrication steps. Resulting polymer has 60 % thiol excess and 40 % epoxy excess.

Step	Instructions	Notes [Example 10g]
1	Measure allyl TMPDE into glass beaker	**[2.39 g]**
2	Add thermal initiator DBN	0.2 % from total desired weight **[0.02 g]**
3	Mix thoroughly and place in oven of 70 °C for 10 minutes	
4	Add Epoxy Novolac Resin DEN 431	**[3.26 g]**
5	Mix well and place in oven of 70 °C	For dissolving
6	Add photoinitiator TPO-L	0.5 % from total weight **[0.05 g]**
7	Mix thoroughly and place beaker into oven of 70 °C for 10 minutes	Liquid should turn yellowish. Let cool down before proceeding
8	Add thiol TMPEC	Amount depends of off-stoichiometry ratio **[4.35 g]**
9	Mix thoroughly and place the beaker into oven of 70 °C for 15 minutes	
10	Degas in vacuum desiccator for 5 minutes	To get rid of possible air bubbles
11	Pour liquid polymer on petri dish or master mold	
12	UV-curing for 30 seconds	If necessary, longer time can be used in order to solidify OSTE+
13	Cut the solid polymer into 12 mm x 30 mm pieces and peel off	Scalpel or scissors can be used
14	Rinse with DI-water, followed by short isopropanol wash and another DI-water shower	To get rid of most of the OSTE+ debris produced while cutting
15	Dry in oven of 70 °C for 30 minutes	To make sure no IPA is left
16	Bond the parts to form functioning stretching chip	

3.2.5 Magnetic membrane fabrication

Magnetic beads embedded OSTE+ First design (Figure 40) relied on magnetic cobalt nanoparticles (diameter <50 nm) with carbon coating (Sigma Aldrich). The polymer OSTE+ (60 % thiol excess, 40 % epoxy excess) was fabricated with same methods as described in Table 4 with the difference that initiator DBN was left out, since it made the polymer too hard for stretching. The polymer was prepared until the step 8 when thiol TMPEC was introduced. At this step, cobalt nanoparticles were added 2.1 % from total polymer weight. After proper mixing, the recipe

continued with same steps as mentioned in Table 4.

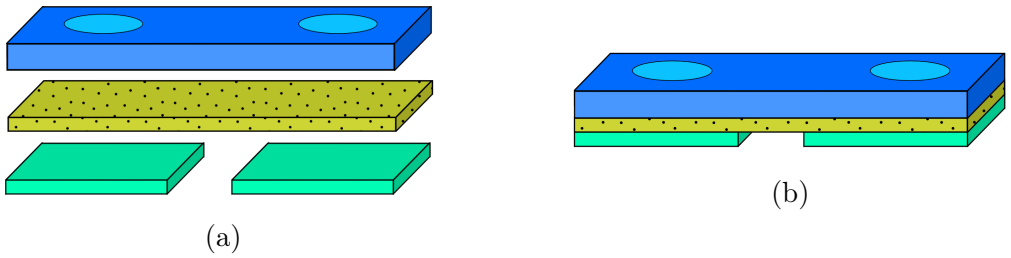

(a) (b)

Figure 40: OSTE+ magnetized with nanoparticles. a) shows individual pieces needed for the chip. It is important to note that the cells grow on top of OSTE+, and the reservoir holes are not punched through it. b) Assembled chip.

Metal rod embedded OSTE+ Second version of polymer membrane with magnetic properties (Figure 41a and 41d) was achieved with metal rods. Membranes with different metal materials and number of rods were fabricated. First of all, the polymer OSTE+ (60% thiol excess, 40% epoxy excess) was fabricated without initiator DBN until the degassing step 10. After this, metal rods (length: 2 – 8 mm, diameter: 1 mm, material: galvanized steel with copper coating (paperclip) or flatwire galvanized steel (staple)) were embedded into liquid polymer. After all rods were in place, polymer was exposed to 365 nm UV-light for 30 seconds. OSTE+ polymer was cut into 12 mm x 30 mm pieces in a way that the metal rod was at the center of the membrane. When bonding the pieces of stretching chip together, care were taken to make sure the metal rod is on top of the gap between glass pieces, and axon isolation chips microchannels were aligned on top of the metal rod.

Magnet embedded OSTE+ Third version (Figure 41b and 41e) replaced metal rods with small permanent neodymium magnets with dimensions of 5 x 1.5 x 1 mm (grade N45) and 5 x 4 x 1 mm (grade N50) (Webcraft GmbH / Supermagnete). OSTE+ polymer was prepared without DBN until the degassing step and the small magnets were embedded into liquid polymer. After 30 seconds curing in 365 nm UV-light, polymer was cut into 30 mm x 12 mm pieces in a way that the magnet is in the middle of the membrane. The final chip was bonded in similar way as with metal rod; the magnet was aligned to be on top of the gap between glass pieces and axon isolation microchannels were aligned on top of the magnet.

Metal rod embedded PDMS with OSTE+ membrane Fourth design of elastic polymer membrane with magnetic properties was implemented with two polymers, PDMS and OSTE+ (Figures 41c and 41f). First, layer of PDMS was fabricated with embedded metal rod. PDMS (Sylgard 184 Silicon elastomer kit) was mixed in 15:1 ratio base:curing agent (w/w). After thorough mixing, the prepolymer was degassed in vacuum desiccator for 80 minutes and poured on polystyrene petri dish

to achieve 1 mm membrane. While PDMS was still liquid, metal rods were inserted and aligned same way as described in metal rod embedded OSTE+ -section. Magnetic PDMS membrane was cured in oven on 50 °C for 120 minutes. While PDMS was curing, OSTE+ (60 % thiol excess, 40 % epoxy excess) was prepared without initiator DBN until the step of degassing and left in oven (note, that all oven steps were done in 50 °C since PDMS was cured in same oven).

After PDMS was cured, it was carefully peeled off from petri dish and placed in plasma chamber, as described in Section 3.2.3. Treated PDMS slab was placed into spinner, and warm liquid OSTE+ was cast on top of the PDMS, and spun with 1000 rpm for 30 seconds in order to achieve thin (∼240 μm) OSTE+ membrane of top on metal rod embedded PDMS. The polymer combination was placed into UV-curing system and treated with 365 nm UV-light for 30 seconds, followed by dicing it into 30 mm x 12 mm pieces in a way that the metal rods are in the middle of each membrane. Bonding of the final chip is similar to previously described methods for metal rod embedded OSTE+ bonding.

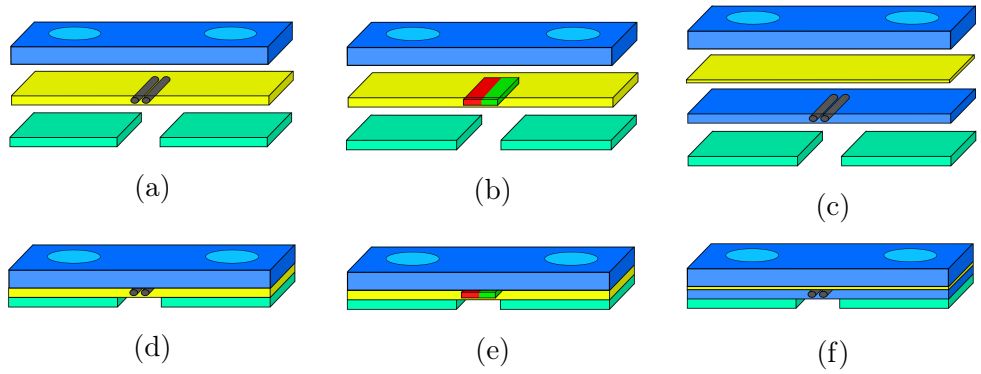

Figure 41: OSTE magnetized with (a) Metal rods and (b) magnet. (c) PDMS magnetized with metal rod, OSTE+ layer on top. (d), (e), (f) Assembled chips.

3.2.6 Stretching chip actuation

The actuation magnets are commercial nickel plated neodymium rare-earth magnets (Webcraft GmbH / Supermagnete), which are labeled to have magnetization grade of N48. Starting point of the actuation setup is presented in Figure 42a. The magnet is brought into close contact with the chip, and the closer the magnets is brought, stronger the magnetic field gets (red lines in Figure 42a). Finally, when the magnet is in contact with the chip (Figure 42b), the stretching force is at maximum. Membrane deflection distance was measured under optical microscope. The microscope was equipped with camera, and after magnet was brought close, image was taken and it was processed with ImageJ software to calculate the deflection distance.

Figures 42a and 42b present only the stretching of the membrane itself. The main function is to stretch axons. First, the axon isolation chip is attached on top of axon stretching chip. Neurons are grown on one reservoir, and plated as

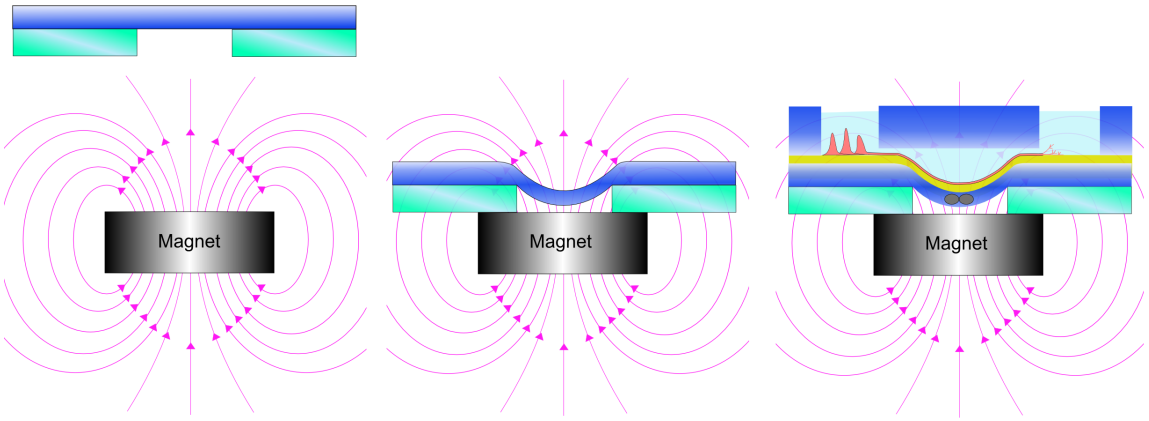

(a) (b) (c)

Figure 42: Schematic setup where the magnet is brought closer to the axon stretching chip. The chip is illustrated with two glass pieces and one membrane for simplicity. In reality, the chip can have dual membrane (PDMS-OSTE). (a) Magnet out of the magnetic field. (b) When magnet is in contact with axon stretching chip, the stretching force is at maximum. (c) Illustration of axon stretching.

close to the channel openings as possible. Then, after neurons have matured until DIV10, their axons should be 2 mm long, and the population is ready for actuation. Cultured neurons are stained with green fluorescent protein (GFP) lentivirus to mark the axons. The chip is placed into custom built stage, which allows the magnet to be in close contact with the neurons while the whole chip is under laser confocal microscope. When magnet is as close to the chips bottom as possible, the membrane stretches downwards, which is illustrated in Figure 42c. Possible reactions can be measured from neurons with increased or decreased calcium activity, and location of axons can be traced with GFP color marking.

3.3 Multielectrode Array chip

Multielectrode array (MEA) chip is made of thin films which are deposited on silicon wafer. Hard aluminum or chromium masks are used while etching, and photoresist is used as passivation layer. These steps will be described in greater detail in next paragraphs. In the final step, axon isolation chip is needed for guiding the axons on top of the electrodes. Materials used are aluminum as mask and conducting enhancement and tungsten or NCC as electrode that is in contact with the nerve cells.

3.3.1 Nanocrystalline carbon

Nanocrystalline carbon (NCC) was primarily studied as electrode material. The fabricated carbon electrode array on silicon substrate is used in probe station where conductors are clamped on the outer electrodes on the chip. The probe station is

built for commercial electrode chip, but with aligned outer electrode layout, it is possible to use same device for these custom made MEA chips.

Deposition First, 100 mm <100> silicon wafer was thermally oxidized in order to get 300 nm thick silicon dioxide layer, which provided electrical insulation. CFUBM sputtering was used to grow NCC conducting layer on top of the SiO_2 layer. The deposition was done at Sungkyunkwan University (SKKU) in Professor Jeon G. Han's laboratory Center for Advanced Plasma Surface Technology (CAPST). Thickness of NCC was 500 nm, and resistivity of the film was 3 Ωcm. Material surface roughness was measured with AFM and carbon bond types with Micro-Raman spectroscopy (WITec Alpha 300 RA).

Reactive Ion Etching Metal mask was deposited on top of the wafer to serve as hard mask for plasma etching. 100 nm of aluminum or chromium was deposited by sputtering (Oxford Instruments, Plasmalab 400). Standard lithography was used to pattern the photoresist. Photoresist served as etch mask for metal wet etching, which was performed in H_3PO_4:HNO_3 mixture in 50 °C for aluminum or 3:1 H_2O:H_2O_2 in room temperature for chromium. Etching time was not critical, since all of the exposed metal was intended to be etched away while avoiding too long under etching. Photoresist was stripped with acetone, which resulted in pattern in Figure 43.

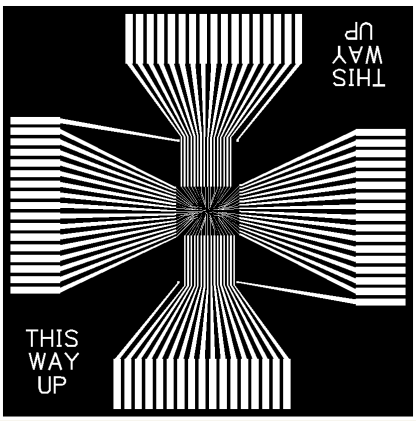

Figure 43: MEA layout. Chip consisted of 68 electrodes, of which 4 acted as reference electrodes. Design mimicked the structure od MED64 electrode chip. Inner electrodes were 50 μm wide rectangles.

Reactive ion etching (RIE) was carried out with Oxford Instruments Plasmalab 80Plus. After several test runs with the machine (Table 18), the recipe shown in Table 5 was used for etching. Etch depth was confirmed with profilometer.

Inductively Coupled Plasma RIE Etching of NCC was also carried out with inductively coupled plasma reactive ion etching (ICP-RIE) (Oxford Instruments Plasmalab System100 - ICP 180). Couple of test runs with NCC material were run with recipe shown in Table 6. Etch depth was confirmed with profilometer.

Table 5: Etch parameters used in RIE

Ar flow	**O_2 flow**	**CHF_3 flow**	**Power**	**Pressure**
80 sccm	50 sccm	50 sccm	100 W	50 mTorr

Table 6: Etch parameters used in ICP-RIE

O_2 flow	**RF Power**	**ICP Power**	**Pressure**	**Temperature**	**DC Bias**
10 sccm	100 W	200 W	3 mTorr	20°C	300 V

After etching, the mask metal was removed from the central pads in order to expose the underlying NCC. Photoresist mask was patterned on the wafer with standard lithography methods. In the case of aluminum mask, the central pad aluminum was removed with aluminum etchant H_3PO_4:HNO_3 mixture in 50 °C. Chromium was removed with H_2O:H_2O_2 in room temperature. After wet etching and rinsing, photoresist etch mask was stripped with acetone. SEM (SEM EBL Zeiss Supra 40) and profilometer (Bruker DekTak/XT) images were taken to confirm etch profile.

Next step was electrode isolation with negative photoresist SU-8 2000.5. The insulating material was intended to cover everything else than inner and outer pads, which served as contact pads between measurement station and studied neurons. Insulating polymer layer was deposited (target thickness: 800 nm) with spin coating method, and the recipe is shown in Table 7.

Table 7: SU-8 2000.5 deposition recipe.

Step	**Info**	**Time**
Spin	3000 rpm	30 s
Soft bake	95 °C	2 min 45 s
Exposure	365 nm UV-light	7 seconds
Post exposure bake	95 °C	5 min
Development	PGMEA	25 seconds
Rinse	IPA & DI-Water	

The final step for the MEA chip was bonding of axon isolation chip on top of it. This way the axons from neurons can be easily guided to grow on top of the inner electrodes, which serve as neuron measurement sites. PDMS was bonded on top of SU-8 layer with oxygen plasma treatment. Schematic view and MEA test setup can be seen in Figure 44.

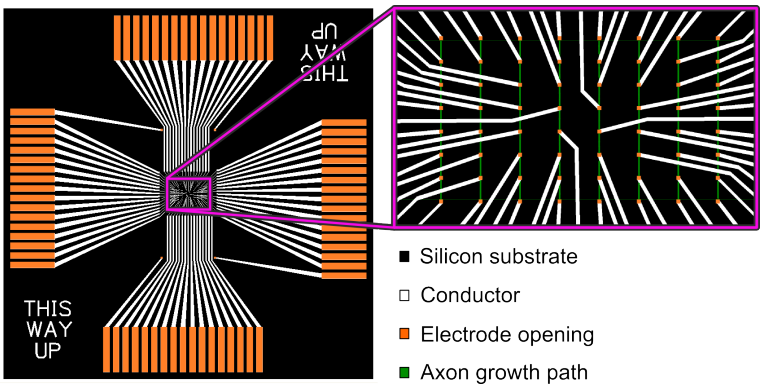

(a) Schematic layout.

(b) Ready MEA with PDMS test ring.

Figure 44: MEA chip. a) Presents schematic setup where axon isolation chip is on top of microelectrodes (green lines represent axon isolation channels). In b) PDMS polymer ring is bonded to provide fluidic isolation. This setup is meant for testing.

3.3.2 Metal electrodes

As a reference, the same electrode design was made from metal. The chosen metal was tungsten with aluminum base layer. In these designs, 500 μm Pyrex glass wafer was used as a substrate.

Tungsten electrode was done in two layers. First layer was 100 nm of aluminum and second layer was 50 nm of tungsten. Etch mask was done with standard lithography and metals were etched in proper etchants: Tungsten with 3:1 H_2O:H_2O_2 at room temperature and aluminum with H_3PO_4:HNO_3 at 50°C. After wet etching, photoresist was stripped and SU-8 passivation layer was deposited as described earlier.

For electrical comparison, an array made from copper was also fabricated. Copper is not biocompatible material, and therefore it could not be used for actual measurement with cells. But since copper is an excellent conductor, it gives good reference point for electrical characterization of the carbon and tungsten MEAs.

Copper electrode was fabricated with lift-off process on silicon wafer. Standard lithography techniques were used with recipe shown in Table 8. In lift-off process, the metal layer is "lifted" from the wafer while removing photoresist, and resulting device will have the metal only in the areas which were not covered by the resist.

3.3.3 MEA measurement

Axon isolation chip made from PDMS is attached on the surface of MEA chip (permanently or temporarily). Neurons are grown on one reservoir of axon isolation chip, and the axonal growth can be measured as soon as the axons reach the first electrodes. Usually after 14 days in vitro (DIV14) the axons have reached the other reservoir. The axon isolation chip is aligned in a way that the channels are on top of inner electrode openings (made from carbon, no metal coating visible). When axons

Table 8: Negative resist ma-N 1407 deposition recipe and lift-off process

Step	Info	Time
Pre-treatment	HMDS	30 min
Spin	3000 rpm	30 s
Soft bake	100 °C	60 s
Exposure	365 nm UV-light	10 s
Develop	TMAH based developer	1-1.5 min
Post exposure	Flood exposure	20 s
Sputter	300 nm Cu	
Lift-off	Immerse into stripper rem-400	1-5 min
Rinse and dry	IPA & DI-water	

touch the carbon surface, it is possible to measure neuronal activity electrically through embedded electrodes.

4 Results and Discussion

This section presents results obtained from different axon stretching chip designs and characterization of NCC. From axon stretching chip, the models are tested with actual device dimensions and materials constants. Then, chip actuation and characterization results are presented in same order as they are presented in Materials and Methods section followed by discussion. Biocompatibility studies and fabrication notes are last parts concerning axon stretching chip.

In second part characterization (AFM, Raman) results of nanocrystalline carbon are presented, followed by etching results with SEM pictures of etching profiles. Lastly, MEA electrical properties are compared between different materials.

4.1 Stretching chip actuation

4.1.1 Modeling membrane deflection

Young's modulus

In axon stretching chip the PDMS curing temperature is 50 °C, and regarding to Johnston et al. [72] (Figure 12), Young's modulus should be approximately 1.6 MPa. But one must note that Johnston et al. used 10:1 base agent:curing agent mixing ratio for their PDMS samples, and our axon stretching chip has ratio of 15:1. Therefore, the Young's modulus should be lower than 1.6 MPa, as increased quantity of base agent makes PDMS more elastic.

In Wang et al. [73] it is stated that 10:1 PDMS has Young's modulus of 2.61 ± 0.021 MPa and 16.7:1 PDMS has 1.21 ± 0.069 MPa with curing temperature of 65 °C. The formula for custom mixing ratio of PDMS seen in Figure 13 given by Wang et al. is

$$E = \frac{20MPa}{n} \tag{21}$$

where n is the ratio of base agent:curing agent.

Now it is possible to calculate the Young's modulus for 15:1 PDMS, which is

$$E = \frac{20MPa}{15/1} = 1.33MPa. \tag{22}$$

The calculated value can be compared to the plot in Figure 13, which shows 15:1 PDMS to have E approximately 1.4 MPa. This value seems logical when compared to results from Johnston et al. and Wang et al.

PDMS is not the only polymer material used in the stretching chip, and therefore Young's modulus for OSTE(+) must be known. According to studies by Carlborg et al., OSTE has Young's modulus of 250 MPa [2]. The E changes when OSTE(+) recipe is changed, but determining OSTE(+) Young's modulus with varied parameters is out of the scope of this thesis. Therefore, $E_{OSTE(+)} = 250$ MPa is used.

Second moment of area
As chip dimensions are known (thickness h = 1 mm, width b = 12 mm), it is possible to calculate the second moment of area with Equation 16:

$$I_y = \frac{(b)^3 h}{12} = \frac{(12mm)^3 1mm}{12} = 144mm^4. \tag{23}$$

Uniform load
The Equation 14 for uniform load is

$$q = \frac{384EI\delta_C}{L^4} \tag{24}$$

where E for OSTE+ is 250 MPa, I = 144 mm^4, and beam length L = 2 mm. Uniform load q is only dependent of maximum deflection δ_C

$$q = \frac{384 \ * 250MPa \ * 144mm^4 \ * \delta_C}{(2mm)^4} = 864\ 000\ MPa \ * \delta_C. \tag{25}$$

Concentrated load
In concentrated load model the pressure P can be calculated with Equation 17. For PDMS membrane, the equation is

$$P = \frac{192 \ * 1.33MPa \ * 144mm^4 \ * \delta_{max}}{(2mm)^3} = 4\ 596.48\ MPa\ mm \ * \delta_{max} \tag{26}$$

and for OSTE+ membrane

$$P = \frac{192 \ * 250MPa \ * 144mm^4 \ * \delta_{max}}{(2mm)^3} = 864\ 000\ MPa\ mm \ * \delta_{max}. \tag{27}$$

4.1.2 Magnetic beads embedded OSTE+

Different concentrations of cobalt magnetic beads were tried in the membrane. The initial starting point is to add 2.1 % of nanoparticles counted from total polymer weight (for example, if there is 10 g of OSTE+, 0.21 g of cobalt particles were added). The final chip design was tested with 2.1 % and 4.2 % cobalt ratios. Table 9 shows membrane bending results when external magnet was brought close.

As can be seen from the table, the vertical movement of the membrane is very small or zero with 4.2 % and 2.1 % concentration, respectively. The zero value for 2.1 % is because the used optical microscope did not have camera with high enough resolution to capture the movement of the membrane. Because of small vertical movement values, the membrane stretch (length of the arc) is also small. By using Equation 18 it is possible to determine the arc length for 4.2 % concentration membrane to be 2003.71 μm and 2000.09 μm with small magnet and big magnet, respectively (initial length $\sim$ 2000 μm). The force produced is not enough to stretch

the axons to a limit of axotomy, and neither to a limit where major biological changes could be measured. With membrane deflection δ_C, it is possible to calculate the load for OSTE(+) membrane with Equation 25. Since the deflection is so small with 4.2 % concentration, values for $q_{\text{small cube}}$ and $q_{\text{big cube}}$ are only 45 619 MPa*mm and 6 912 MPa*mm respectively.

Table 9: Membrane deflection with magnetic beads, when exposed to external magnetic field.

Particle concentration (%)	Used magnet	Membrane deflection (μm)	Elongation (μm)	Strain
2.1	Small cube	0	0	0.00
2.1	Big cube	0	0	0.00
4.2	Small cube	52.8	3.7	∼0.00
4.2	Big cube	8.0	0.1	∼0.00

4.1.3 Metal rod embedded OSTE+

The metal rod membrane had seven different setups for rod length and orientation (See Figure 45). Preliminary tests without membrane deflection measurement showed that short rods in line generated internal magnetic poles when exposed to external magnetic field. These poles then either repelled or attracted each other and the short metal rods started to twist inside polymer, which is some cases lead to failure in polymer adhesion to metal. Also the actuation force was weaker than in one long rod version. Therefore the short rod designs were discarded based on these preliminary tests.

Preliminary tests for single rod with varying length were performed to find out the strength of the magnetic field affecting to individual metal rod. Experiments show that the longer the rod is, more the membrane deflects, which seems logical conclusion, as longer ferromagnetic rod has more magnetic domains in which external magnetic field has influence on. Based on these tests, three different designs were used in final membrane deflection tests: one, two or three rods in parallel.

As the external magnet creates magnetic field around it (shown in Figure 42b) also the ferromagnetic rod magnetizes and creates positive and negative magnetic poles. Therefore the external magnet needs to be aligned correctly in order to pull the rod uniformly downwards. If the external magnet is not aligned properly, the metal rod starts to twist inside the polymer and try to align along magnetic fields. That is the reason why the orientation of magnetic field needs to be tested every time before starting stretching experiments. Orientation is rather easy to determine: when the magnet is brought closer to the membrane (2-3 cm), it can be clearly seen if the rod is pulled downwards uniformly, or if the rod starts twisting. After finding out the correct magnetic field orientation, stretching experiments can be done by

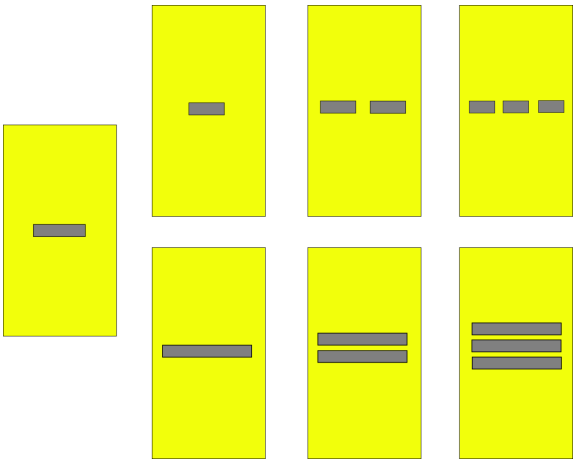

Figure 45: Seven different metal rod configurations. Three different lengths of rods were tested: 2 mm, 3 mm and 7 mm.

placing the magnet into immediate contact with the axon stretching chip. Results of stretching experiments can be seen in Table 10, where two different external magnets were tested. If chip is placed into culturing well, the magnet can be placed under the well; magnetic force is strong enough to pull the membrane even through 1-2 mm gap.

Table 10: OSTE+ membrane deflection with metal rods, when exposed to external magnetic field. The magnet is brought into immediate contact with the chips glass spacers.

Amount of small rods	**Used magnet**	**Membrane deflection (μm)**	**Elongation (μm)**	**Strain**	**Force (μN)**
1	Small cube	73.2	5.4	~0.00	13.3
1	Big cube	67.8	4.6	~0.00	11.5
2	Small cube	90.0	8.1	~0.00	20.2
2	Big cube	100.4	10.1	~0.00	25.1
3	Small cube	130.4	11.3	~0.00	0.10
3	Big cube	151.8	15.3	~0.00	0.14

As can be seen, the deflection is higher than with magnetic beads. With Equation 18, it is possible to determine the strain of the polymer membrane where axons are grown. The force is calculated with Equation 20. One must note, that the presented force is calculated, not measured. The force is applied only to the polymer membrane and not the individual axons. Other research groups have acquired forces like 12 pN – 400 pN [41], 250 nN – 25 μN [44], and 0.18 N [45], but their system designs differ from the axon stretching chip and therefore the forces are not directly

comparable.

Interesting force values can be seen between 2 rods and 3 rods. This difference is because when embedding 3 rods into the membrane, 2 mm gap between glass slides was not enough for actuation, and therefore the gap had to be enlarged to 3 mm, and this value is used in calculations. These results show promise but the stretch length is still no enough for proper axotomy. Smith et al. [20] report that axotomy needs > 65 % strain to occur. This is the reason why other designs were considered, as described in next chapters.

When maximum deflection δ_{max} is known, concentrated load P can be calculated with the Equation 27. The membrane deflection values presented in Table 10 yield values for P from 58 579 MPa*mm^2 to 131 155 MPa*mm^2.

4.1.4 Magnet embedded OSTE+

Magnet embedded OSTE+ was actuated similarly as metal rod embedded OSTE+. With this design, care had to be taken to approach with the external magnet with correct magnetic field orientation, as the small embedded magnet reacts more vigorously to external magnetic field than metal rod. The few experiments done with embedded magnet are shown in Table 11. Experiments were also carried out with PDMS membrane, and the results are listed in Table 12.

Surprisingly, the magnet reacts less to external magnetic field than metal rods. This might be due to the fact that embedded magnet could only be aligned into the membrane in a way that the poles are located in different sides of axon isolation channels (horizontally, not vertically). This means that the external magnet should also be aligned horizontally, as vertical magnetic field would twist the embedded magnet. This alignment can weaken the magnetic pulling force. Another problem with OSTE+ measurement was loss of adhesion. During actuation, the polymer network around the magnet was not strong enough to hold it inside for a long time, and in many cases the membrane was destroyed. PDMS membrane deflects a lot more than OSTE+, but it had the same problem of detaching. Also the gap between glass slides had to be a little bigger than 2 mm.

Table 11: OSTE+ membrane deflection with embedded magnet, when exposed to external magnetic field.

Chip number	Used magnet	Membrane deflection (μm)	Elongation (μm)	Force (μN)
1	Small cube	~19.2	0.37	0.1
1	Big cube	~23.0	0.53	1.3
2	Small cube	~16.8	0.28	0.7
2	Big cube	~21.6	0.47	1.2

Concentrated load P can be calculated with Equation 26 and 27. For OSTE+ membrane, the P varied from 14 515 MPa*mm^2 to 19 872 MPa*mm^2. For PDMS membrane, the P was calculated to vary from 5 222 MPa*mm^2 to 15 325 MPa*mm^2.

Table 12: PDMS membrane deflection with embedded magnet, when exposed to external magnetic field.

Chip number	Used magnet	Membrane deflection (μm)	Elongation (μm)	Strain	Force (μN)
1	Small cube	1136.2	1027.2	0.51	13.7
1	Big cube	1711.2	1963.9	0.98	26.1
2	Small cube	1666.8	1887.5	0.94	25.1
2	Big cube	3333.6	4960.7	2.48	66.0

4.1.5 Metal rod embedded PDMS with OSTE+ membrane

The previous designs rely totally on OSTE+ polymer. But after several tests it can be noted that OSTE+ is not as flexible and stretchable (Young's modulus in OSTE+ is higher than in PDMS) as PDMS when the membrane is thick (1-2 mm). This was found to be major reason for low deflection distances with previous designs, but as neuron growth of PDMS is difficult, the novel design of PDMS with OSTE+ layer was invented. In this design, the metal rod can be embedded into PDMS which is responsible for mechanical properties, and OSTE+ coating allows neuron growth.

The results from deflection experiments can be seen in Table 13. The chip was fabricated with one, two or three parallel metal rods, and thickness of PDMS was around 1 mm while OSTE+ membrane was kept as thin possible, around 200-300 μm. This dual layer membrane has Young's modulus higher than plain PDMS membrane (E = 1.33 MPa), but as OSTE+ membrane is kept very thin, the E value of PDMS membrane is used to be able to do calculations.

Table 13: Membrane deflection with embedded rod in PDMS with OSTE+ layer, when exposed to external magnetic field.

Amount of long rods	Used magnet	Membrane deflection (μm)	Elongation (μm)	Strain	Force (μN)
1	Small cube	359.0	125.0	0.06	1.66
1	Big cube	350.4	119.2	0.06	1.59
2	Small cube	1495.4	1597.9	0.80	21.25
2	Big cube	1336.8	1338.9	0.67	17.81
3	Small cube	875.4	658.1	0.33	8.75
3	Big cube	618.2	351.3	0.18	4.67

For comparison, experiments with just PDMS membrane were performed. These results are shown in Table 14. The fabrication process for PDMS membrane is similar to the design at hand, but this time the OSTE+ is not spun on top of

PDMS. Another way to make experiments is to peel off the OSTE+ membrane after measurements; this way it is possible to compare exact same membranes.

Table 14: Membrane deflection with embedded rod in PDMS, when exposed to external magnetic field.

Amount of long rods	Used magnet	Membrane deflection (μm)	Elongation (μm)	Strain	Force (μN)
1	Small cube	723.8	468.9	0.23	6.2
1	Big cube	714.6	458.2	0.23	6.1
2	Small cube	1315.0	1304.1	0.65	17.3
2	Big cube	1545.4	1681.5	0.84	22.4
3	Small cube	1173.4	1083.4	0.54	14.4
3	Big cube	3024.0	4370.1	2.19	58.1

When comparing the Tables 13 and 14, it can be seen that the deflection is higher with plain PDMS membrane. The last measurement in Table 14 shows extraordinary high deflection. This might be due to higher gap between glass slides.

Concentrated load P can be calculated with Equation 27. For PDMS with OSTE+ membrane, the P was calculated to vary from 1 610 MPa*mm^2 to 6 874 MPa*mm^2 with different amount of rods. With plain PDMS membrane the P varied from 3 285 MPa*mm^2 to 13 899 MPa*mm^2.

The axonal stretch chip had maximum elongation of 1 598 μm with PDMS-OSTE+ membrane, and the corresponding force pulling the 2 rods in the membrane was calculated to be 21.3 μN. Desmaele et al. [41] describe in their review many different cell stretching devices. These devices generated forces from 12 pN to 400 pN, and elongations between 3.4 μm and 50 μm were reported. Kamotani et al. [45] deflected their membrane with Braille display 0.4 mm with force of 0.18 N, and Sasoglu et al. [44] acquired forces between 250 nN and 25 μN with their polymeric beam setup. The axon stretching chips proves to function in larger range, as the membrane deflection can be lowered by moving the external magnet further.

With the above results, it is possible conclude that the stretch chip and external magnet can produce forces and strains high enough to stretch the axon and even perform axotomy. Smith et al. [20] report that $>$ 65 % strain is needed for axotomy, and the PDMS-OSTE+ chip produced strains from 5 % to 80 % with 2 mm long membrane.

4.2 Stretching chip biocompatibility

The effect of several surface treatments on OSTE+ were tested for biocompatibility. Oxygen plasma treatment has proved to be functional with PDMS, and therefore the same method is implemented with OSTE+. PLL coating was also carried out. Neuron culturing was performed on treated chips.

4.2.1 Plasma treatment of OSTE+

The water contact angles of OSTE+ with and without an oxygen plasma treatment are shown in Table 15. Two types of OSTE+ are studied: with and without DBN. The native contact angle of OSTE+ without DBN was 71.8° ± 2.0°, while after the plasma process the contact angle was 10.1° ± 0.8°. OSTE+ with DBN had native contact angle of 74.6° ± 13.6° and after plasma the contact angle was 24.0° ± 3.0°. The surface thus becomes much more hydrophilic which should make it more suitable for adhesion and growth of neurons. These results are similar to what has been described for PDMS and many other polymers [47, 76, 127].

Table 15: Water contact angle on OSTE+ before and after oxygen plasma treatment.

Without DBN

Sample no.	Before plasma	After plasma	Change
1	69.8°	9.0°	60.8°
2	74.5°	11.0°	63.5°
3	71.0°	10.4°	60.6°
Average	71.8°± 2.0°	10.1°± 0.8°	61.6°± 1.3°

With DBN

Sample no.	Before plasma	After plasma	Change
4	93.8°	27.4°	66.4°
5	66.4°	24.5°	42.0°
6	63.6°	20.0°	43.7°
Average	74.6°± 13.6°	24.0°± 3.0°	50.7°± 11.1°

A series of contact angle measurements were performed with 24 hour frequency. Results are shown in Figure 46. The initial state is shown on the left side of the graph, and measured contact angle is measured and drawn as a graph. Two different compositions of OSTE+ were tried: with and without thermal initiator DBN.

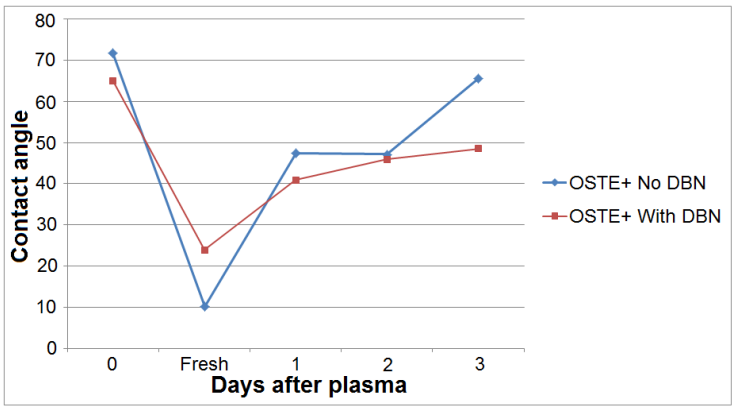

Figure 46: Graph showing OSTE+ hydrophobic recovery

It can be seen that for both types of OSTE+ (with and without DBN), the hydrophilicity obtained by plasma treatment is partially lost over time. Over the course of three days, the contact angle with DBN recovers to 48.5°, while the contact angle without DBN recovers to 65.7°. The experiment shows hydrophobic recovery of OSTE+, but the recovery time is several days. More experiments are required to find out if the contact angle recovers to the initial state in longer time. This effect means that if plasma treatment is used for neuronal adhesion, the treatment should be as fresh as possible. It is an open question whether with OSTE+ the hydrophobic recovery happens also if the surface is kept submerged in liquid (like during a neurobiology experiment).

4.2.2 Neuron culturing

Due to many difficulties with neuron culturing, only preliminary studies have been made with growth experiments on top of OSTE and OSTE+. All the neuron growth experiments on OSTE(+) were carried out by Cecilia Brunello in University of Helsinki. In these experiments, neurons have grown on some OSTE and OSTE+ samples, but the results are not consistent. In one experiment, 10 samples were coated with PLL and neurons were plated on top of them. From these, only 30 % showed viable neuron maturation. The reason for why neurons do not grow on all OSTE and OSTE+ samples has not been found. The growth result may vary even if the polymer sample is cut from the same piece. More studies are needed to find the reason for the problem.

4.3 Axon stretching chip fabrication notes

In the axon stretching chip, the novelty is in the magnetized polymer substrate where neurons are grown. The magnetized substrate is connected to axon isolation chip in order to apply the stretching only to axons. In this device, the membrane is deflected with magnetic force. Magnetically actuated element is embedded inside polymer material (ferromagnetic nanoparticles, metal rod, or permanent magnet) and the device is operated by external magnet, which is brought into proximity. The magnetic field from external magnet affects in ferromagnetic material inside the polymer, which leads to an attractive force towards external magnet. A schematic drawing of the actuation can be seen in Figure 29. As the distance between external magnet and ferromagnetic element gets shorter, the magnetic field get stronger, and higher force is pulling the membrane.

The motivations for improving different designs were either lack of material biocompatibility, structural difficulties in the design, or lack of actuation force. The parental chips had also their own disadvantages, which had to be taken into account when the novel stretching chip emerged. Previously presented axotomy chip (Figure 35) had challenges of connecting the microchannels after dicing the chip in half. The connection of microchannels was crucial in order to have the axons growing over the gap, as illustrated in Figure 47. Even though it was somehow possible to align and connect the halves of the chip together under optical microscope in xy-direction,

it was quite impossible to say if there were any steps in z-direction. Axons can conform to the shapes and structures while growing, but too high steps will appear as a walls and axon growth will be misdirected. Therefore the connection of the chips were tried to enhance by widening the channels. Three different dimensions (Figure 36) were tested in addition to the original, 7.5 μm wide channels. Results show that fluidic connection between the chips was improved, so widening the channels makes alignment in xy-direction better, but does not necessarily improve z-direction mismatch.

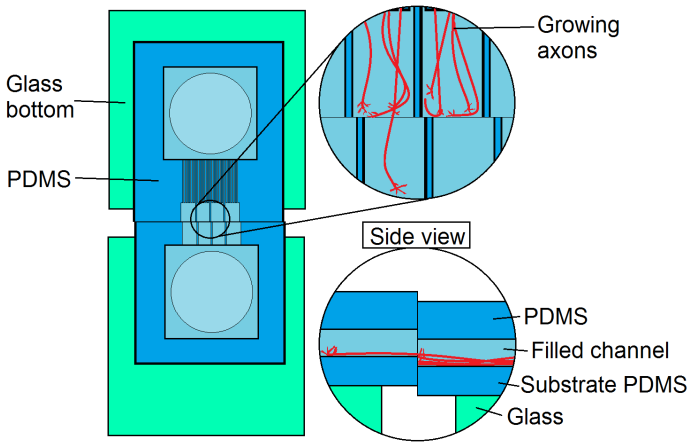

Figure 47: Schematic illustration of neurons growing in axotomy chip. Even minor misalignment in the chip can prevent the axon proliferation over the gap between two pieces.

Another problem with early versions of axotomy chip was material properties; PDMS is hydrophobic by nature, and does not support cell adhesion without proper treatments. There are studies where cells are grown successfully on PDMS [41], but in our experiments this has not been highly successful. Oxygen plasma treatment makes PDMS temporarily hydrophilic, and it enables poly-L-lysine coating, which is required for neuron culturing. Some studies also guide to embed particles or monomers into bulk polymer in order to get long lasting hydrophilic PDMS surface [128, 129, 130]. We tried to embed especially Pluronic F127, as Wu et al. suggests [131], but the surface was not as hydrophilic as they claimed. Also the leaching effect of PDMS proved relevant, as Pluronic F127 leached out of PDMS when chips were sterilized in ethanol.

The presented first version of axon stretching chip had similar problems as the axotomy chip: PDMS is naturally hydrophobic, and axons don not grow over the glass-PDMS interface. The reason why axons do not grow from glass to PDMS is not because of a possible step between the materials. The reason most probably is a change in hydrophobicity. As axon growth cone is all the time searching a new area and direction to attach, it will most probably prefer glass to PDMS as a substrate material. Therefore the solution for both of these abovementioned designs would be the change of substrate material, to OSTE(+) for example.

Most chips included either embedded particles in the bulk material or embedded objects. During the embedding process, care had to be taken in order to fabricate fully functional chip with proper actuation properties. As the stretching is wanted to occur only in axons, alignment was crucial. These important fabrication facts will be discussed in following paragraphs in more detail, and possible alternative solutions are presented.

4.3.1 Magnetic beads embedded OSTE+

Magnetic beads were added to prepolymer mixture just before UV-curing step. Beads require thorough mixing in order to distribute them uniformly in the polymer. If prepolymer mixture is placed into oven for further mixing, one can notice that magnetic beads tend to clump close to each other in around 5 minutes. This is because the beads are ferromagnetic, and small residual magnetism can be stored inside them, and they therefore start to attract each other. These clumps of magnetic beads can be broken with strong mixing. After curing the mixture into solid, the beads are strongly bonded inside polymer network.

Two different concentrations were used in the fabrication, 2.1 % and 4.2 % from total polymer weight. Even with the lower concentration the liquid prepolymer turned into dark grey / black, but it was still possible to cure it with normal curing times. The higher concentration started to shadow the lowest parts of the polymer in a way, that normal UV-curing time was not enough to solidify the whole OSTE+. Therefore, longer UV-curing time was used, but even with that it could be seen that the strength of the polymer network was weaker due to high amount of particles inside.

4.3.2 Metal rod embedded OSTE+

When the OSTE+ is heated in oven for uniform mixing of components, the viscosity of polymer is reduced, close to viscosity of water. This can emerge as a problem with metal rods inside OSTE+, as the polymer does not give mechanical support for rods and they move out of place easily, if used petri dish or similar is tilted or shook.

One plausible problem can occur if the metal rod(s) are placed into curing dish (flat petri dish for example) before the liquid polymer is poured in. Even though the polymer might spread around petri dish uniformly, some air can be trapped under the rod, and after curing this leads to unstable rod placement. When magnet is brought into closer contact with metal rod (ferromagnetic material), the ever denser magnetic field pulls the rod even higher force, and if the structural support is incomplete, the rod might be pulled off.

Another problem might arise if the polymer is first poured into the dish and rod is placed afterwards. There is a possibility that the rod is not fully embedded inside polymer, and it leaves the metal surface exposed (might even happen due to surface tension). After curing there is polymer under the rod, and structural strength is not a problem, but the biocompatibility of used materials might be. The interface between polymer and metal might not support cell growth, and the axon do not

propagate over the metal surface. Also, if the chosen metal is not biocompatible, the neurons might not grow at all.

It goes without saying that alignment of the metal rod is critical, because if the rod is not in the middle of the axon isolation channels, the stretch force is not fully transferred to axons. The rod must also be perpendicular to the channels, as this provides the highest possible force. One key feature must be noted: UV-curing of polymer under the rod. Since the rod is made from metal, it does not let UV-light pass through it, and therefore the polymer film under the rod does not receive as much UV-light as the polymer around it. This is not a problem when only one rod is used, as it does now shadow too big area. But when more than one rod is placed into the chip, the shadowed area is larger and attention must be paid to the curing issue. Usually long enough curing times should solve the problem.

4.3.3 Magnet embedded OSTE+

When small block magnet is used possible issues are similar to the rods explained above. But in addition to those, the magnetic field must be taken into account. Magnets tend to pull each other, when opposite poles are facing each other, and therefore attention must be paid when aligning the magnets into their place in the dish. If the embedded magnets are brought too close to each other before curing, they either repel or attract each other, and this ruins the orientation. Therefore the density is smaller with magnets, as distance between separate chips must be larger. Also one must note that if the chips are intended to be identical, the magnet must always be placed into polymer in same orientation (same direction of poles). This enables standard orientation of actuation magnet in the future.

Another possible problem with magnets inside OSTE+ is environment. If the curing dish is brought too close to ferromagnetic objet, the small magnets start to attract the ferromagnetic material. The object is either pulled close to the dish, or worse, the magnets start moving towards the object and they can also clump to each other. Therefore care must be taken when moving the petri dish into UV-curing system. When detaching the solid polymer membrane with embedded magnets, scalpel must be used between the magnet and petri dish, as the polymer acted like glue between magnet and petri dish.

4.3.4 Metal rod embedded PDMS with OSTE+ membrane

Even though this design is closely related to metal rod embedded OSTE+, there are some key differences. First of all, the metal rod is now embedded inside PDMS. PDMS has higher viscosity than OSTE+, and therefore the rod does not move in uncured polymer as easily as in OSTE+. But as a tradeoff, PDMS has longer curing time, so even though the rod does not move as easily, it has longer time to drift into misalignment. This can only be helped with making sure the used oven is as horizontal as possible. Similar problems as with embedding rods into OSTE+ are present. The 360° coating around rod is not crucial, because there will be OSTE+ film on top of the PDMS. So, if there is no polymer underneath the rod, it is possible

to just turn the chip upside down and spin the OSTE+ membrane on the side where metal is exposed.

Deposition method for OSTE+ film is spinning. The procedure is similar to photoresist deposition of top of silicon wafer. First, as a pretreatment, cured PDMS slab with embedded rods is placed into plasma chamber in order to make the surface hydrophilic (and it increases the adhesion between two polymers). When the PDMS slab is in the spinner, heated OSTE+ is taken from the oven and poured on the substrate. The OSTE+ is recommended to have as low-viscosity as possible, that is why it is poured hot.

Thickness of the dual polymer membrane should be as small as possible, as thicker membrane will be stronger, which results in that the final membrane will be stiffer. Therefore, PDMS should be a little thicker than the embedded metal rod in order to have proper structural strength. OSTE+ membrane should be as thin as possible, as thicker membranes bend less. The thickness of PDMS can be controlled with weight, and thickness of OSTE+ can be controlled with spinning parameters.

4.4 Multielectrode Array chip

Multielectrode array chip is shown in Figure 44. The smallest features were the inner electrodes (50 μm squares with 240 μm distance to each other) intended for axons to attach. This means, that when photolithography allows for $\sim$3 μm accuracy in alignment, the presented chip did not have critical alignment in that scope. Alignment was needed when inner electrodes were cleared from masking metal, and second time when passivation layer was patterned.

4.4.1 Nanocrystalline carbon characterization

NCC film was characterized with atomic force microscopy, Raman spectroscopy and 4-point probe to find out the surface roughness, carbon bond composition, and material resistivity. AFM results can be seen in Figure 48.

Results show that the RMS roughness for NCC is 2.69 nm. For comparison, microscope slides made from glass can have RMS roughness of 0.5 nm. Neuron growth and maturation need somewhat rough surface, as the cells need to attach on the surface in order to stay alive. Brunetti et al. [132] made experiments with gold surface with RMS roughness ranging from 0.46 nm to 99.8 nm, and report that too rough (RMS $\sim$54.2 nm) surfaces can trigger a cascade of signaling processes that eventually lead to necrosis.

Raman spectroscopy was performed in two ways: area scan and line scan. Area scan parameters were: image area 1920 μm^2, lines per image 100, points per line 100, integration time 0.01 s. Line scan parameters were: line length 2934 μm, points in line 50, accumulations per point 10, integration time 0.5 s. Acquired results are presented in Figure 49.

Results show two peaks which correspond to two different carbon bonds: D-peak for sp^3 bond (diamond) and G-peak for sp^2 bond (graphene). D-peak can be found from 1360 cm^{-1} and G-peak from 1580 cm^{-1}. Other distinguishable peaks in the

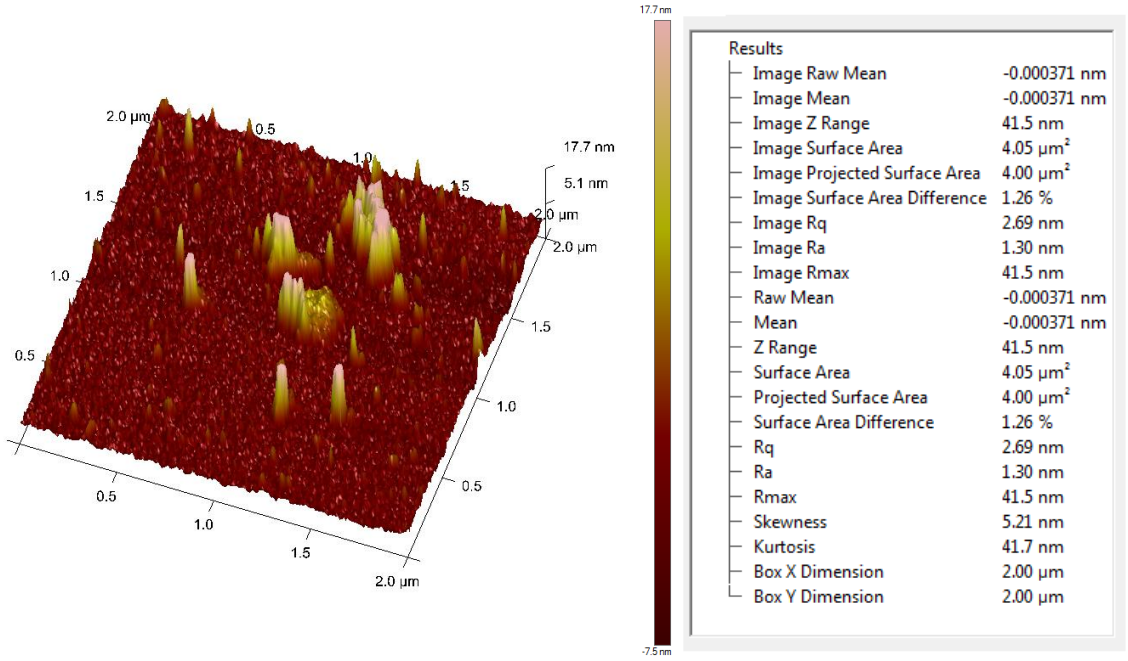

(a) 3D image of AFM scan.

(b) AFM scan specifications

Figure 48: AFM scan of NCC surface roughness

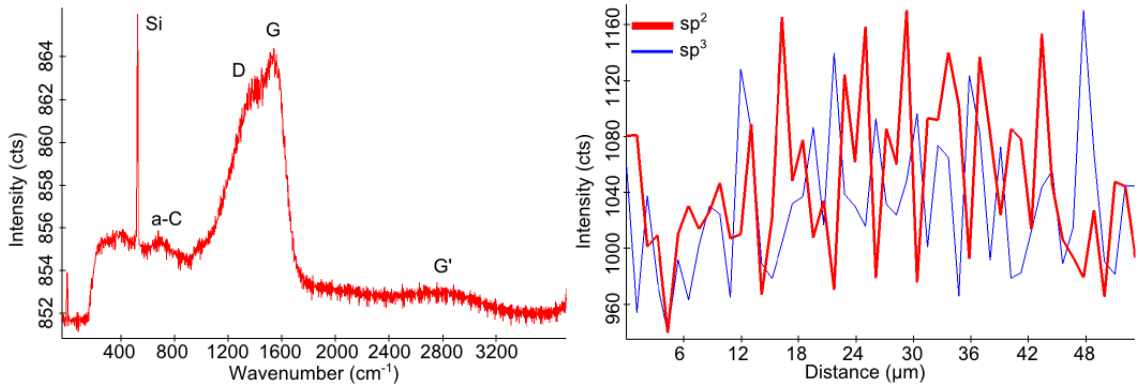

(a) Average Raman spectrum from area.

(b) Raman spectrum from line.

Figure 49: Raman spectrum from area of 48 x 40 μm. a) Average spectrum of the area shows G-peak to be higher. b) Line scan where red is for sp^2 bond and blue is for sp^3 bond.

graph are sharp Si peak at 550 cm^{-1}, small a-C peak (amorphous carbon) around 700 cm^{-1} [133], and G'-peak around 2700 cm^{-1}, which is second overtone of D-mode (and not G-mode as the name suggests) [134]. The averaged graph in Figure 49a shows higher G-peak, which indicates NCC to contain more sp^2 bonds than sp^3 bonds. Higher sp^2 content means more conductive film, which in our case is desired property. The line graph shown is filtered information, where red line corresponds

to sp^2 bond and blue to sp^3 bond. Some locations show higher sp^3 content, but most parts of the line indicate higher sp^2 content.

Thin film resistance was measured with four point probing. Results are shown in Table 16.

Table 16: NCC resistance measurements with four point probe.

Measurement	Resistance (kΩ)
1	13
2	12
3	15
4	16
Average	13.3 ± 1.2

After acquiring the resistance by measurement, the corresponding sheet resistance and resistivity had to be calculated with formula

$$\rho = R_s * t = \frac{W}{L} * R * t = 4.532 * 13.4\ k\Omega * 500\ nm = 3.2\ \Omega cm \tag{28}$$

where ρ is resistivity, R_s is sheet resistance, t is film thickness, and W is width and L length of the sample (for round wafer, W/L = 4.532). The average measured resistance was 13.3 kΩ ± 1.2 kΩ and corresponding sheet resistance 63.4 kΩ/□ ± 5.7 kΩ/□. These yielded resistivity of 3.2 Ωcm. For comparison, Table 17 shows resistivities of some common materials. NCC proves to conduct electricity between diamond and graphene. The conductivity is sufficient for MEA arrays.

Table 17: Resistivities of some common materials found from literature.

Material	Resistivity (Ωm)
Graphene	$1.0*10^{-8}$ [135]
Gold	$2.2*10^{-8}$ [136]
Aluminum	$2.6*10^{-8}$ [136]
Titanium	$4.0*10^{-7}$ [136]
Graphite	$5.0*10^{-6}$-$3.0*10^{-3}$ [137]
NCC	$3.2*10^{-2}$
Silicon	$1.5*10^{-4}$-$1.0*10^{2}$ [87]
Diamond	$1.0*10^{14}$-$1.0*10^{18}$ [137]

4.4.2 Nanocrystalline carbon etching

Etching of NCC was done with two methods, reactive ion etching (RIE) and inductively coupled plasma RIE (ICP-RIE).

Reactive ion etching

In the present study, different gas compositions were tested. Tested gases can be found in Table 18. The different colored rows indicate reference runs, as test series were 1-9, 15-19 and 20-24. Test runs 10-14 were done with 'trial-and-error' method, where interesting parameters (according to test series 1-9) were tried out. The column with 'Sample 1', 'Sample 2', and 'Sample 3' indicates different nanocrystalline carbon films. Multiple samples were diced from one type of film and several RIE runs were performed. The final etch rate shown is result from average value from many etched samples. Green color shows the highest three etch rates achieved.

Table 18: Used RIE recipes and average etch rates.

Test Number	Power (W)	Pressure (mTorr)	Gas flow (sccm)				Gas ratio	Total flow (sccm)	Time (min)	Etch rate (nm/min)		
			Argon	Oxygen	SF_6	CHF_3				Sample 1	Sample 2	Sample 3
1	40	50	80	20	0	0	4:1	100	2	16,31	12,14	
2	40	100	80	20	0	0	4:1	100	2	10,58	4,37	
3	40	150	80	20	0	0	4:1	100	2	8,92	6,54	
4	60	50	80	20	0	0	4:1	100	2	16,97	13,07	
5	80	50	80	20	0	0	4:1	100	2	18,62	9,76	
6	40	50	80	40	0	0	2:1	120	2	15,56	5,64	
7	40	50	80	50	0	0	8:5	130	2	6,82	4,02	
8	40	50	80	20	0	0	4:1	100	2	7,27	4,30	
9	40	50	80	20	0	0	4:1	100	2	12,09	0,99	
10	80	50	80	40	40	0	2:1:1	160	2	9,31	41,46	
11	80	50	0	20	80	0	0:1:4	100	2	2,17	0,57	
12	80	50	80	20	0	0	4:1	100	6	15,32	6,50	
13	80	50	80	20	0	0	4:1	100	10	9,37	4,50	
14	80	50	80	40	0	0	2:1	120	2	20,22	11,78	
15	80	50	80	10	40	0	8:1:4	130	2			11,20
16	80	50	80	25	25	0	8:3:3	130	2			8,68
17	80	50	80	20	80	0	4:1:4	180	2			7,83
18	80	50	80	50	50	0	8:5:5	180	2			12,61
19	80	50	80	10	40	0	8:1:4	130	2			6,43
20	80	50	80	10	0	40	8:1:4	130	2			5,24
21	80	50	80	25	0	25	8:3:3	130	2			13,69
22	80	50	80	20	0	80	4:1:4	180	2			10,74
23	80	50	80	50	0	50	8:5:5	180	2			14,70
24	80	50	80	10	0	40	8:1:4	130	2			5,29

In our experiments, the final etching recipe contained also gas CHF_3, meaning the etchant contained elements H, C, F, O and Ar. As the final etching profile was anisotropic, some conclusions can be made with different material reactions.

First of all, argon is inert gas, and does not react with any of the mentioned elements. But argon has important role in enhancing the ion etching process, as it provides more energy to etched surface, and can produce sputter etching. As mentioned before, oxygen most probably reacts with carbon, both in the chamber (etchant gas) and in the substrate to form CO_2 and CO, which can be pumped out of the system. This leaves H, C and F in the chamber, which will most probably react with each other. H reacts with F to create hydrofluoric acid, and it can be pumped out. C will also react with F in chamber to form COF_2, but also on the

carbon substrate, and create C_2F_4. This film is uniform and has good step coverage (it covers both vertical and horizontal walls), but as ion bombardment is present only to horizontal walls, the film is etched away (because of O_2 ions). This leaves protective polymer film only to vertical walls, which prevent isotropic etching by O_2 ions and bouncing Ar ions. [138]

When SF_6 is used along O_2 and Ar, the reaction products with carbon are most probably CO, CO_2, C_2F_4, and COF_2 [113]. SF_6 can be broken into ${SF_4}^{2+}$ and ${SF_2}^{4+}$ with ionization, which leads to SOF_4 and SO_2F_2 [114]. These formed gases can be pumped out of the system, as they will not react with carbon substrate. Therefore, SF_6 is a good source for fluorine, as F^- ions will react vigorously with C-atoms in the substrate.

In the shown experiments etching with gas SF_6 produced highest etching rate of 41 nm/min, but as can be seen from further experiments, the results was not repeatable. Also etching with SF_6 shows varying etch rates with similar recipes, whereas experiments with CHF_3 show more repeatable etch rates. For example, test number 21 has O_2:CHF_3 ratio 1:1 and total gas flow 130 sccm, and test number 23 has O_2:CHF_3 ratio 1:1 but total gas flow 180 sccm, but both have still similar etch rates. This contrasts results with SF_6 (test 16 versus 18) shows 31% change in etch rate. As a conclusion from these experiments, test number 23 with power of 100 W was used when MEA chip was fabricated. With etch time of 33.5 min, it was possible to achieve average 15 nm/min etch rate. Figure 50 shows SEM images of etch profiles during and after etching.

In literature it is commonly found that tetrahedral amorphous carbon (similar composition as nanocrystalline carbon) is etched in oxygen plasma [110, 139, 140]. A proposed reason for this is that when high energy O_2 ions collide into sp^2 and sp^3 bonded carbon atoms, the strong carbon-carbon bond breaks, and released C-atoms create new bonds with available O_2, and resulting material is CO_2 [140]. Some of the oxygen ions as well as argon ions produce sputter etching due to transfer of high energy, but no new compounds are formed.

Inductively coupled plasma reactive ion etching

Only preliminary test for ICP-RIE of NCC were done. The results are shown in Table 19. With only minimal O_2 gas flow of 10 sccm it was possible to achieve stunning 42 nm/min etch rate. Further studies are needed to confirm this result, and to develop better recipes. The etch rate difference between test number 1 and 2 is due to different NCC composition. Test number 1 is from higher conductivity NCC ($\rho = 20$ mΩcm), and test number 2 from lower conductivity NCC ($\rho = 3$ Ωcm).

Table 19: Used ICP-RIE recipes and average etch rates.

Test Number	RF Power (W)	ICP Power (W)	Pressure (mTorr)	Gas (sccm)			Temperature (°C)	DC Bias (V)	Time (min)	Etch rate (nm/min)
				O2	SF6	H2				
1	100	200	3	10	0	0	20	300	2	18
2	100	200	3	10	0	0	20	300	2	42

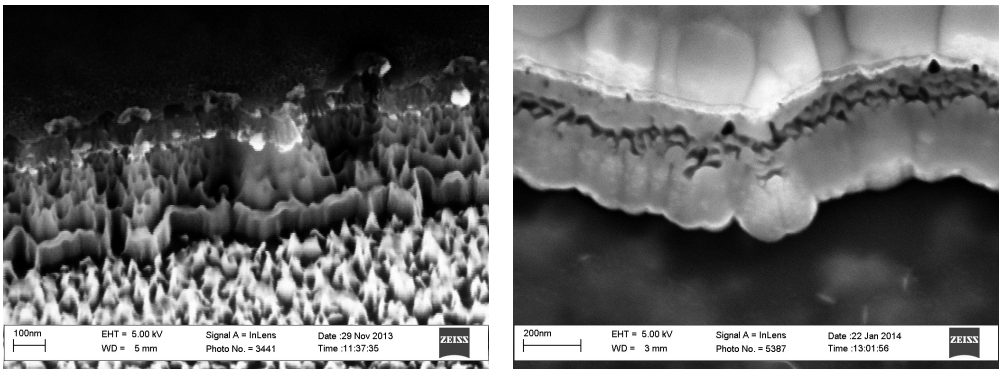

(a) Etch not ready. (b) Etch ready.

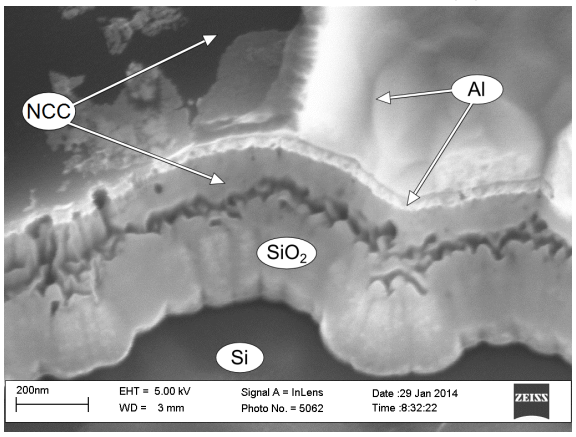

(c) Etch ready, metal partly removed

Figure 50: SEM pictures of different steps of etching. a) Shows etch step where NCC is not completely etched. In b) etching is complete and different layers can be seen. c) Shows location where metal is partly removed by wet etching.

Besides etching, NCC also showed other interesting properties. One property observed is that passivation layer SU-8 2000.5 does not attach to NCC very well, as can be seen from Figure 51. The figure is taken with stylus profilometer DekTak/XT.

The most interesting part in the picture is the zoomed area, where one pad is shown. The dark square in the small picture is the area where aluminum has been etched away, and as can be seen, some aluminum from the conducting path has also been lost. This is because the mask with aluminum etch mask has 200 μm x 200 μm squares to be sure to etch all aluminum from the pads. The downside is that the conducting paths of other electrodes are so close to the pads that some of the covering aluminum is lost while etching.

In the mask for SU-8 insulation the inner pads are only 50 μm x 50 μm squares, the same size as the carbon pads. Therefore, in theory SU-8 should cover some of the exposed carbon from conducting paths, and there should not be risk of having short circuits or other disturbances. But after developing SU-8 and inspecting results with microscope, it can be seen that SU-8 is lost at the 50 μm x 50 μm square as intended, but SU-8 has also been lost from other exposed carbon surfaces as well.

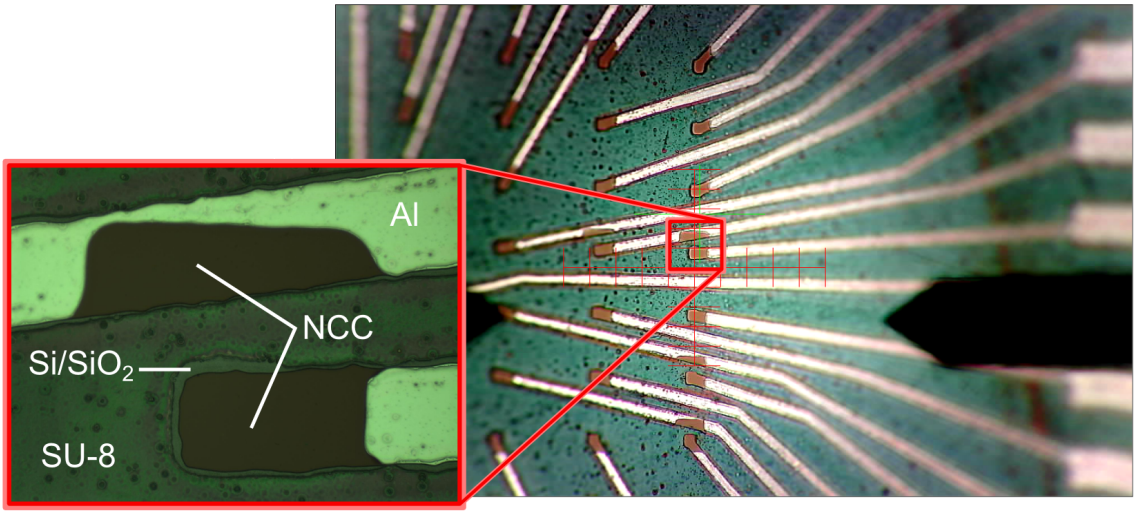

Figure 51: Picture of MEA chip inner electrodes. Picture is taken with Bruker profilometer DekTak/XT, close-up with optical microscope. Different materials present are shown in close-up.

Profilometer measurement was performed over the pads and conducting paths to confirm the visual data. Profilometer graph is shown in Figure 52. The picture on left shows the line in which the stylus measured, and corresponding regions are marked under the graph with red and yellow bars.

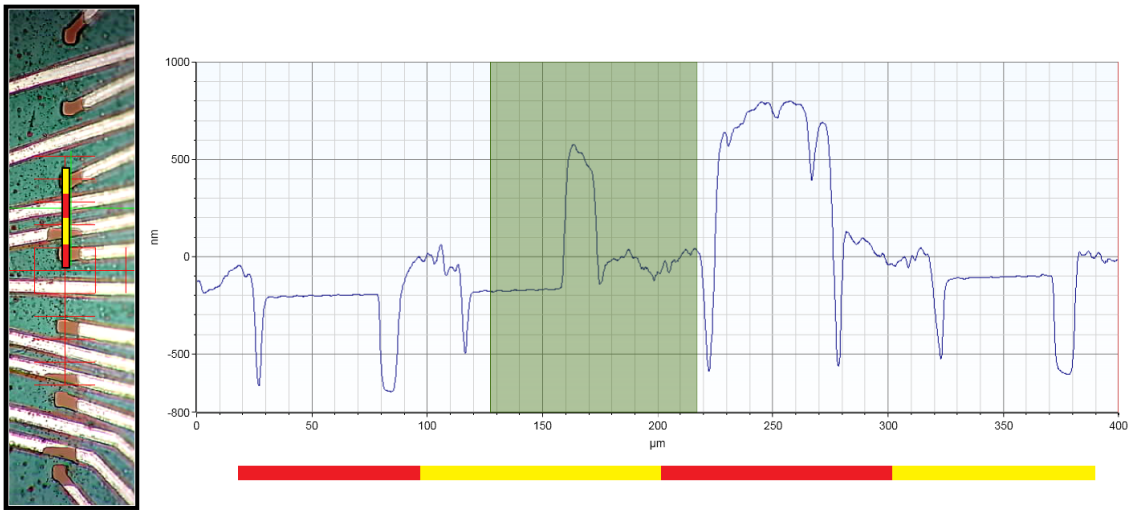

Figure 52: Profile graph from SU-8 coating. The red-yellow bar shows the region of measurement. In the measured line inner electrode openings and conducting paths can be seen.

As can be seen, the first red area marking the 50 μm central pad shows flat surface, which is carbon, and high structures on both sides of the flat area, which

are SU-8 passivation coatings. There are interesting valleys between the carbon and SU-8, which can be because of UV-light scattering during UV-exposure.

The first yellow area shows probably to most interesting data from this measurement. First, a small valley is found between rough SU-8 surface and flat area. This flat area is exposed carbon on conducting line. It is interesting because the used mask did not have any patterns at this area, therefore the whole conducting path has been exposed to UV, including carbon surface. But still, the SU-8 passivation layer is missing. The part of conducting line where aluminum coating is still present, the passivation layer is properly attached. The reason for lack of SU-8 can be loss of adhesion, but after analyzing pictures from the area, there are no signs of rupture. Therefore the reason can be that carbon layer acts as inhibitor for photoactive molecule in SU-8 and prevents polymerization in that area, leading to loss of passivation layer during development. This is preliminary result, and more research on this subject should be performed in order to make valid conclusions.

The second red area is profile from conducting path completely coated with polymer. Once again the small valleys around the structure can be seen. Last yellow area shows another inner pad, where carbon layer is exposed. Profilometer measurements show SU-8 2000.5 layer to have roughly the thickness of 800 nm (target thickness: 800 nm).

4.4.3 Neuron culturing

Biocompatibility of NCC was tested with neuron growth experiments done by Shokoufeh Khakipour and Tatiana Sukhanova in University of Helsinki. Two substrate materials, NCC and glass coverslips, were coated with poly-D-Lysine. Embryonic hippocampal rat neurons (Wistar rats, E17) were cultivated on both samples at a density of 150 000 cells/cm^2. Primary antibodies (anti-KCC2 (1:2 000 dilution, Rabbit) and NeuN (1:400 dilution, Mouse)), were diluted to the final concentration in 2 % serum / 0.1 % Triton X-100 / PBS. Results show enhanced maturation and arborization of individual neurons. Growth experiment images can be seen in Figure 53.

KCC2 is a K-Cl co-transporter and a marker of neuronal cell maturation. Anti-KCC2 and anti-NeuN antibodies were used for visualization of neurons and measuring KCC2 expression intensity. From Figure 53 it can be seen that KCC2 expression is higher in neurons cultivated on NCC substrates beginning from DIV3. The results demonstrate that interaction with NCC substrate stimulates neuronal cell activity and maturation.

When observing individual neurons on NCC substrate, more branched and longer neurites can be seen. The neurite arborization can be explained by interaction of membrane with semiconductor lipophilic support and thus stimulation of neuronal cell development. Properties of nanocrystalline carbon could be responsible for enhanced neuron maturation even though the material is coated with PDL. Enhanced maturation has also been reported with other substrate materials/scaffolds, like silk fibroin nanofibers [141], hybrid nanofiber matrix [142], and microfilament scaffolds [143], and neuronal regeneration is reported in chitosan gel sponge [144]. Other

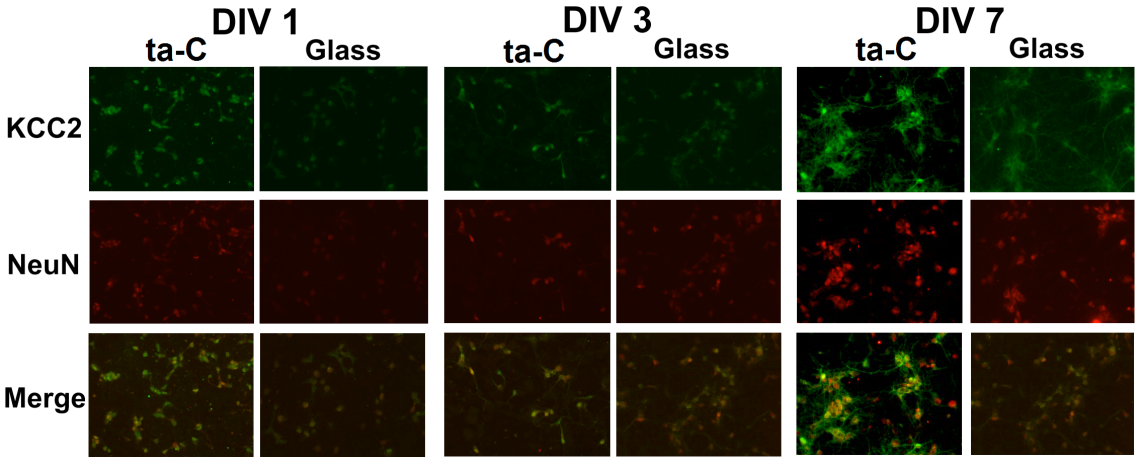

Figure 53: Hippocampal neuron culturing on NCC and glass substrate with KCC2 and NeuN expression. A - Immunostaining by anti-KCC2 (green) and anti-NeuN (red) antibodies. Images show more intense colors on NCC substrate compared to glass substrate, which indicate more maturated cells.

carbon-based materials have showed similar results with enhanced neuronal maturation. Carbon nanotubes are reported to increase expression of KCC2 co-transporter (indicator of neuronal cell maturation) [145] and graphene has enhanced the differentiation of hNSCs (human neural stem cells) into neurons [146].

4.4.4 MEA electrical properties

Multiple versions of the multielectrode array were fabricated, and the electrical properties are shown in Table 20. The resistance was measured from all four reference electrodes, and the average value is compared with other electrode types. Two commercial MED64 chips were also measured and compared.

As the results show, electrodes fabricated only from metal gives a lot lower resistance than the commercial MED64 chips. The chip named Carbon #1 has only NCC as conductive material, and it has very high resistance, $R_{ave} = 1.56$ MΩ. But since the carbon shows many beneficial properties for neuron growth, a combination of metal and carbon electrodes (named Carbon #2 and Carbon #3) were fabricated, and they have resistance of $R_{ave} = 28.5$ Ω and $R_{ave} = 6.5$ Ω, respectively. The metal-carbon electrodes have metal on top of carbon for enhanced electrical conduction, but the metal is removed from the inner pads where neurons are growing.

Table 20: Different MEA chip array materials and their electrical resistance. Thin film layers are listed from top to bottom. Two MED64 chips are commercial products, other MEAs are fabricated during this research.

MEA	Substrate	Layers	Insulation	Resistance (Ω)
MED64 #1	Polymer	Gold ITO	Acrylate resin	528 556 505 455 ave 511
MED64 #2	Glass	Pt Black ITO	Acrylate resin	459 463 455 462 ave 459.8
Metal #1	Pyrex	50 nm W 100 nm Al	SU-8, 2000.5	10.2 10.1 10.5 10.5 ave 10.3
Metal #2	Pyrex	300 nm Al	SU-8, 2000.5	6.4 5.9 6.8 6.5 ave 6.4
Metal #3	Silicon	139 nm Cu	-	11.0 10.1 12.2 13.3 ave 11.7
Carbon #1	Silicon	100 nm NCC 300 nm SiO_2	SU-8, 2000.5	1.13 M 1.72 M 2.06 M 1.32 M ave 1.56 M
Carbon #2	Silicon	100 nm Al 500 nm NCC 300 nm SiO_2	SU-8, 2000.5	32 29 27 26 ave 28.5
Carbon #3	Silicon	300 nm Al 500 nm NCC 300 nm SiO_2	SU-8, 2000.5	8.1 6.1 5.3 6.5 ave 6.5

5 Summary and conclusions

New devices and materials for neuroscience were developed using microfabrication technologies. Three different materials were studied in this research: OSTE, OSTE+ and NCC. Polymer materials OSTE and OSTE+ were characterized, and functioning neuron stimulation device was fabricated and characterized. The forces achieved with magnetic actuation were calculated to be between 0.1 - 25 μN. Largest strain of 1 598 μm was achieved with the PDMS-OSTE+ chips with two embedded metal rods.

Nanocrystalline carbon was characterized with AFM, Raman spectroscopy and 4-point probe, and the characteristics proved to enable cell growth and proper conductivity. Etching experiments were carried out with RIE and ICP-RIE, and highest achieved etch rate was 42 nm/min. Multielectrode array was successfully fabricated from NCC, and electrical properties of different MEAs were measured. Biocompatibility of NCC was studied with cell growth experiment. Carbon material proved to enhance the maturation and arborization of rat hippocampal neurons after three days of cultivation.

OSTE and OSTE+ can be compared to PDMS, which is widely used elastomer and its properties are well known. PDMS can be tuned by its mechanical properties (stiffness, elasticity), but the surface chemistry is mostly the same. Here OSTE and OSTE+ have shown more tunable properties: their chemical composition can be tuned with the ratio of mixed monomers. Different ratios change the functionality of the material crucially. This gives OSTE and OSTE+ advantage over PDMS, as they can have more widespread applications.

OSTE and OSTE+ biocompatibility was studied in this thesis, but the successful results could not be reproduced. More studies are needed in this field, as OSTE(+) can provide stretchable, bendable and twistable growth substrate. The key for proper cell culture on OSTE(+) would enable variety of different studies on functional cell growth platforms.

In this thesis, one completely new device for neuronal research using OSTE+ as functional material was introduced: axon stretching chip. In the chip, common materials as glass and PDMS are present, but by applying OSTE+ on top of PDMS layer, neurons can be grown, stretched, and measured on single device. By magnetic actuation, the stretching forces can be easily adjusted from axonal stretching to axotomy. This could be important for studying varying grades of trauma.

There were not any successful neuron experiments with axon stretching chip, since OSTE(+) supported cell growth only decently. When the problems with OSTE(+) biocompatibility are solved, the stretching chip is ready to be used and the stretching results can be used as a model for studies of neuronal trauma.

Nanocrystalline carbon shows great promise in biological applications. Some metals can be compared to NCC according to their materials characteristics, but the major difference between NCC and metals can be found from the durability and strength. Carbon sheet is practically inert to any liquid etchants, and it is very strong against mechanical damage. It can be patterned with dry etching methods by using non-hazardous gases, and it supports cell culturing.

The MEA fabricated from NCC can be used to track axon growth by attaching axon isolation chip on it. Without the chip, MEA can be used to measure the maturation and activity of neuronal network. This study is especially interesting because of the NCC maturation enhancement property.

This thesis has showed wide range of possibilities microtechnology offers in the field of neuroscience. Since only preliminary studies and results are presented here, more research is required to further characterize the material properties and their functionality as cell growth substrates. OSTE(+) shows promise to become as popular and widely used as PDMS, which gives biologists, engineers, and researchers from other fields of science more possibilities to choose material to best suit their application. The interest to carbon-based materials has increased during last two decades, and NCC created with CFUBM sputtering will become part of the carbon material family.

References

[1] Francisco López-Muñoz, Jesús Boya, and Cecilio Alamo. Neuron theory, the cornerstone of neuroscience, on the centenary of the Nobel Prize award to Santiago Ramón y Cajal. *Brain Research Bulletin*, 70(4–6):391 – 405, 2006.

[2] Carl Fredrik Carlborg, Tommy Haraldsson, Kim Öberg, Michael Malkoch, and Wouter van der Wijngaart. Beyond PDMS: off-stoichiometry thiol–ene (OSTE) based soft lithography for rapid prototyping of microfluidic devices. *Lab on a Chip*, 11(18):3136–3147, 2011.

[3] Mark P Mattson, Robert C Haddon, and Apparao M Rao. Molecular functionalization of carbon nanotubes and use as substrates for neuronal growth. *Journal of Molecular Neuroscience*, 14(3):175–182, 2000.

[4] Hui Hu, Yingchun Ni, Vedrana Montana, Robert C Haddon, and Vladimir Parpura. Chemically functionalized carbon nanotubes as substrates for neuronal growth. *Nano letters*, 4(3):507–511, 2004.

[5] Yu Wang, Wong Cheng Lee, Kiran Kumar Manga, Priscilla Kailian Ang, Jiong Lu, Yan Peng Liu, Chwee Teck Lim, and Kian Ping Loh. Fluorinated graphene for promoting neuro-induction of stem cells. *Advanced Materials*, 24(31):4285–4290, 2012.

[6] Ville Jokinen, Prasanna Sakha, Pia Suvanto, Claudio Rivera, Sami Franssila, Sari E. Lauri, and Henri J. Huttunen. A microfluidic chip for axonal isolation and electrophysiological measurements. *Journal of Neuroscience Methods*, 212(2):276 – 282, 2013.

[7] J. G. White, E. Southgate, J. N. Thomson, and S. Brenner. The structure of the nervous system of the Nematode Caenorhabditis elegans. *Philosophical Transactions of the Royal Society of London. B, Biological Sciences*, 314(1165):1–340, 1986.

[8] Suzana Herculano-Houzel. The remarkable, yet not extraordinary, human brain as a scaled-up primate brain and its associated cost. *Proceedings of the National Academy of Sciences*, 109(Supplement 1):10661–10668, 2012.

[9] Gerard J. Tortora and Bryan Derrickson. *Principles of Anatomy and Physiology*, volume 1. John Wiley & Sons, 12th edition, 2009.

[10] Dominique Debanne, Emilie Campanac, Andrzej Bialowas, Edmond Carlier, and Gisèle Alcaraz. Axon physiology. *Physiological Reviews*, 91(2):555–602, 2011.

[11] WL Maxwell, A Irvine, JH Adams, TA Gennarelli, R Tipperman, M Sturatis, et al. Focal axonal injury: the early axonal response to stretch. *Journal of neurocytology*, 20(3):157–164, 1991.

[12] Douglas H Smith and David F Meaney. Axonal damage in traumatic brain injury. *The neuroscientist*, 6(6):483–495, 2000.

[13] Roger S Chung, Jerome A Staal, Graeme H McCormack, Tracey C Dickson, Mark A Cozens, Jyoti A Chuckowree, Marian C Quilty, and James C Vickers. Mild axonal stretch injury in vitro induces a progressive series of neurofilament alterations ultimately leading to delayed axotomy. *Journal of neurotrauma*, 22(10):1081–1091, 2005.

[14] WL Maxwell and DI Graham. Loss of axonal microtubules and neurofilaments after stretch-injury to guinea pig optic nerve fibers. *Journal of neurotrauma*, 14(9):603–614, 1997.

[15] Donna M Geddes and Robert S Cargill. An in vitro model of neural trauma: device characterization and calcium response to mechanical stretch. *Journal of biomechanical engineering*, 123(3):247–255, 2001.

[16] Robert B Campenot. Local control of neurite development by nerve growth factor. *Proceedings of the National Academy of Sciences*, 74(10):4516–4519, 1977.

[17] Robert B Campenot. Development of sympathetic neurons in compartmentalized cultures: I. local control of neurite growth by nerve growth factor. *Developmental biology*, 93(1):1–12, 1982.

[18] Jean-Pierre Dollé, Barclay Morrison III, Rene S Schloss, and Martin L Yarmush. An organotypic uniaxial strain model using microfluidics. *Lab on a Chip*, 13(3):432–442, 2013.

[19] Yu-Ju Chang, Cho-Jen Tsai, Fan-Gang Tseng, Tsung-Ju Chen, and Tzu-Wei Wang. Micropatterned stretching system for the investigation of mechanical tension on neural stem cells behavior. *Nanomedicine: Nanotechnology, Biology and Medicine*, 9(3):345 – 355, 2013.

[20] Douglas H Smith, John A Wolf, Theresa A Lusardi, Virginia M-Y Lee, and David F Meaney. High tolerance and delayed elastic response of cultured axons to dynamic stretch injury. *The Journal of neuroscience*, 19(11):4263–4269, 1999.

[21] S Klostermann and F Bonhoeffer. Investigations of signaling pathways in axon growth and guidance. *Perspectives on developmental neurobiology*, 4(2-3):237–252, 1995.

[22] Kathryn J Ivins, Elizabeth TN Bui, and Carl W Cotman. β-amyloid induces local neurite degeneration in cultured hippocampal neurons: evidence for neuritic apoptosis. *Neurobiology of disease*, 5(5):365–378, 1998.

[23] Anne M Taylor, Seog Woo Rhee, Christina H Tu, David H Cribbs, Carl W Cotman, and Noo Li Jeon. Microfluidic multicompartment device for neuroscience research. *Langmuir*, 19(5):1551–1556, 2003.

[24] Anne M Taylor, Daniela C Dieterich, Hiroshi T Ito, Sally A Kim, and Erin M Schuman. Microfluidic local perfusion chambers for the visualization and manipulation of synapses. *Neuron*, 66(1):57–68, 2010.

[25] Anne M Taylor and Noo Li Jeon. Micro-scale and microfluidic devices for neurobiology. *Current opinion in neurobiology*, 20(5):640–647, 2010.

[26] Jean-Michel Peyrin, Bérangère Deleglise, Laure Saias, Maéva Vignes, Paul Gougis, Sebastien Magnifico, Sandrine Betuing, Mathéa Pietri, Jocelyne Caboche, Peter Vanhoutte, et al. Axon diodes for the reconstruction of oriented neuronal networks in microfluidic chambers. *Lab on a Chip*, 11(21):3663–3673, 2011.

[27] Thibault Honegger, Mark A Scott, Mehmet F Yanik, and Joel Voldman. Electrokinetic confinement of axonal growth for dynamically configurable neural networks. *Lab on a Chip*, 13(4):589–598, 2013.

[28] Thibault Honegger, Moritz Thielen, Joel Voldman, et al. Contactless three-dimensional guidance of axonal growth. In *17th International Conference on Miniaturized Systems for Chemistry and Life Sciences (microTAS 2013)*, 2013.

[29] Thibault Honegger, Moritz Thielen, and Joel Voldman. Three-dimensional topological neural networks based on ac electrokinetic confinment of neurites. In *18th International Conference on Miniaturized Systems for Chemistry and Life Sciences (microTAS 2014)*, 2014.

[30] George M Whitesides. The origins and the future of microfluidics. *Nature*, 442(7101):368–373, 2006.

[31] Curtis D Chin, Vincent Linder, and Samuel K Sia. Commercialization of microfluidic point-of-care diagnostic devices. *Lab on a Chip*, 12(12):2118–2134, 2012.

[32] Jiseok Lim, Florine Maes, Valérie Taly, and Jean-Christophe Baret. The microfluidic puzzle: chip-oriented rapid prototyping. *Lab on a Chip*, 14(10):1669–1672, 2014.

[33] Stephen C Terry, John H Jerman, and James B Angell. A gas chromatographic air analyzer fabricated on a silicon wafer. *Electron Devices, IEEE Transactions on*, 26(12):1880–1886, 1979.

[34] Haakan N Joensson and Helene Andersson Svahn. Droplet microfluidics—a tool for single-cell analysis. *Angewandte Chemie International Edition*, 51(49):12176–12192, 2012.

[35] Materials Research Science University of Wisconsin and Engineering Center. Microfluidic devices? `http://chemlinks.beloit.edu/Edetc/nanolab/shrink/index.html`, June 2015.

[36] Joose Kreutzer, Liisa Ikonen, Juha Hirvonen, Mari Pekkanen-Mattila, Katriina Aalto-Setälä, and Pasi Kallio. Pneumatic cell stretching system for cardiac differentiation and culture. *Medical Engineering & Physics*, 36(4):496 – 501, 2014.

[37] Yuta Nakashima, Ryo Monji, Katsuya Sato, and Kazuyuki Minami. Cell stretching microdevice for evaluating cellular biomechanics based on in-situ cellular response observation. In *17th International Conference on Miniaturized Systems for Chemistry and Life Sciences (microTAS 2013)*, 2013.

[38] Flexcell Int. *FX-5000 Tension System Manual*, 2014.

[39] Flexcell Int. *Tension Baseplate Assembly Manual*, 2013.

[40] Flexcell int. Flexcell International Corporation. `http://www.flexcellint.com/index.html`, December 2014.

[41] Denis Desmaële, Mehdi Boukallel, and Stéphane Régnier. Actuation means for the mechanical stimulation of living cells via microelectromechanical systems: A critical review. *Journal of biomechanics*, 44(8):1433–1446, 2011.

[42] F Mert Sasoglu, Andrew J Bohl, and Bradley E Layton. Design and microfabrication of a high-aspect-ratio PDMS microbeam array for parallel nanonewton force measurement and protein printing. *Journal of Micromechanics and Microengineering*, 17(3):623, 2007.

[43] S Joo, J Lim, and Y Nam. Designing well-ordered neural network on a microelectrode array using agarose hydrogel. In *18th International Conference on Miniaturized Systems for Chemistry and Life Sciences (microTAS 2014)*, 2014.

[44] F Mert Sasoglu, Andrew J Bohl, Kathleen B Allen, and Bradley E Layton. Parallel force measurement with a polymeric microbeam array using an optical microscope and micromanipulator. *computer methods and programs in biomedicine*, 93(1):1–8, 2009.

[45] Yoko Kamotani, Tommaso Bersano-Begey, Nobuhiro Kato, Yi-Chung Tung, Dongeun Huh, Jonathan W Song, and Shuichi Takayama. Individually programmable cell stretching microwell arrays actuated by a Braille display. *Biomaterials*, 29(17):2646–2655, 2008.

[46] Ross G Harrison. On the stereotropism of embryonic cells. *Science*, 34:279–281, 1911.

[47] Erwin Berthier, Edmond WK Young, and David Beebe. Engineers are from PDMS-land, Biologists are from Polystyrenia. *Lab on a Chip*, 12(7):1224–1237, 2012.

[48] Jingyan Han, Blaine J Zern, Vladimir V Shuvaev, Peter F Davies, Silvia Muro, and Vladimir Muzykantov. Acute and chronic shear stress differently regulate endothelial internalization of nanocarriers targeted to platelet-endothelial cell adhesion molecule-1. *ACS nano*, 6(10):8824–8836, 2012.

[49] Chia-Yen Lee, Chin-Lung Chang, Yao-Nan Wang, and Lung-Ming Fu. Microfluidic mixing: a review. *International journal of molecular sciences*, 12(5):3263–3287, 2011.

[50] Pavel Neuži, Stefan Giselbrecht, Kerstin Länge, Tony Jun Huang, and Andreas Manz. Revisiting lab-on-a-chip technology for drug discovery. *Nature reviews Drug discovery*, 11(8):620–632, 2012.

[51] Kentaro Kawai, Kenta Arima, Mizuho Morita, and Shuichi Shoji. Microfluidic valve array control system integrating a fluid demultiplexer circuit. *Journal of Micromechanics and Microengineering*, 25(6):065016, 2015.

[52] Aaron J Dy, Alin Cosmanescu, James Sluka, James A Glazier, Dwayne Stupack, and Dragos Amarie. Fabricating microfluidic valve master molds in SU-8 photoresist. *Journal of Micromechanics and Microengineering*, 24(5):057001, 2014.

[53] Carl Fredrik Carlborg, Tommy Haraldsson, Matteo Cornaglia, Göran Stemme, and Wouter van der Wijngaart. A high-yield process for 3-D large-scale integrated microfluidic networks in PDMS. *Microelectromechanical Systems, Journal of*, 19(5):1050–1057, 2010.

[54] J Cooper McDonald and George M Whitesides. Poly (dimethylsiloxane) as a material for fabricating microfluidic devices. *Accounts of chemical research*, 35(7):491–499, 2002.

[55] Sunghwan Chang and Young-Ho Cho. Static micromixers using alternating whirls and lamination. *Journal of Micromechanics and Microengineering*, 15(8):1397, 2005.

[56] Norbert Kockmann, Thomas Kiefer, Michael Engler, and Peter Woias. Silicon microstructures for high throughput mixing devices. *Microfluidics and Nanofluidics*, 2(4):327–335, 2006.

[57] Martin Zimmermann, Heinz Schmid, Patrick Hunziker, and Emmanuel Delamarche. Capillary pumps for autonomous capillary systems. *Lab on a Chip*, 7(1):119–125, 2007.

[58] Lauri Sainiemi, Teemu Nissilä, Ville Jokinen, Tiina Sikanen, Tapio Kotiaho, Risto Kostiainen, Raimo A Ketola, and Sami Franssila. Fabrication and fluidic characterization of silicon micropillar array electrospray ionization chip. *Sensors and Actuators B: Chemical*, 132(2):380–387, 2008.

[59] Hong Miao Ji, Victor Samper, Yu Chen, Chew Kiat Heng, Tit Meng Lim, and Levent Yobas. Silicon-based microfilters for whole blood cell separation. *Biomedical microdevices*, 10(2):251–257, 2008.

[60] Suman Bose, Rishi Singh, Mikhail Hanewich-Hollatz, Chong Shen, Chia-Hua Lee, David M Dorfman, Jeffrey M Karp, and Rohit Karnik. Affinity flow fractionation of cells via transient interactions with asymmetric molecular patterns. *Scientific reports*, 3, 2013.

[61] Dongeun Huh, Benjamin D Matthews, Akiko Mammoto, Martín Montoya-Zavala, Hong Yuan Hsin, and Donald E Ingber. Reconstituting organ-level lung functions on a chip. *Science*, 328(5986):1662–1668, 2010.

[62] G Di Caprio, D Shaak, JM Higgins, and E Schonbrun. A lung-on-chip to measure oxygen affinity of single red blood cells. In *18th International Conference on Miniaturized Systems for Chemistry and Life Sciences (microTAS 2014)*, 2014.

[63] Jen-Huang Huang, Pulak Nath, Jennifer F Harris, Ayesha Arefin, and Rashi Iyer. Fabrication of human respiratory construct for in vitro drug development. In *18th International Conference on Miniaturized Systems for Chemistry and Life Sciences (microTAS 2014)*, 2014.

[64] J Seo and D Huh. A human blinking 'eye-on-a-chip'. In *18th International Conference on Miniaturized Systems for Chemistry and Life Sciences (microTAS 2014)*, 2014.

[65] Z Abdi Dezfooli, S-S Bolz, and A Günther. Vein-on-a-chip: Microfluidic platform for functional assessment and staining of intact veins. In *18th International Conference on Miniaturized Systems for Chemistry and Life Sciences (microTAS 2014)*, 2014.

[66] Kyung-Jin Jang, Ali Poyan Mehr, Geraldine A Hamilton, Lori A McPartlin, Seyoon Chung, Kahp-Yang Suh, and Donald E Ingber. Human kidney proximal tubule-on-a-chip for drug transport and nephrotoxicity assessment. *Integrative Biology*, 5(9):1119–1129, 2013.

[67] J Park, S Kim, J Li, and A Han. Brain-on-a-chip: An in vitro myelination model. In *18th International Conference on Miniaturized Systems for Chemistry and Life Sciences (microTAS 2014)*, 2014.

[68] JS Park, BK Lee, GS Jeong, CJ Lee, and SH Lee. Development of a three-dimensional brain-on-a-chip with an interstitial level of flow and its application

as an in vitro model of Alzheimer's disease. In *18th International Conference on Miniaturized Systems for Chemistry and Life Sciences (microTAS 2014)*, 2014.

[69] Janelle R Anderson, Daniel T Chiu, Hongkai Wu, Olivier JA Schueller, and George M Whitesides. Fabrication of microfluidic systems in poly (dimethylsiloxane). *Electrophoresis*, 21:27–40, 2000.

[70] Joint Assessment of Commodity Chemicals. JACC 055: Linear Polydimethylsiloxanes. CAS No. 63148-62-9 (Second Edition). ISSN-2079-1496-55 online, December 2011.

[71] Dow Corning. What is silicone? `http://www.dowcorning.com/content/discover/discovertoolbox/you-know-silicone.aspxl`, December 2014.

[72] ID Johnston, DK McCluskey, CKL Tan, and MC Tracey. Mechanical characterization of bulk Sylgard 184 for microfluidics and microengineering. *Journal of Micromechanics and Microengineering*, 24(3):035017, 2014.

[73] Zhixin Wang, Alex A Volinsky, and Nathan D Gallant. Crosslinking effect on polydimethylsiloxane elastic modulus measured by custom-built compression instrument. *Journal of Applied Polymer Science*, 131(22), 2014.

[74] Yun Seok Heo, Lourdes M Cabrera, Jonathan W Song, Nobuyuki Futai, Yi-Chung Tung, Gary D Smith, and Shuichi Takayama. Characterization and resolution of evaporation-mediated osmolality shifts that constrain microfluidic cell culture in poly (dimethylsiloxane) devices. *Analytical chemistry*, 79(3):1126–1134, 2007.

[75] Véronique Lecault, Michael VanInsberghe, Sanja Sekulovic, David JHF Knapp, Stefan Wohrer, William Bowden, Francis Viel, Thomas McLaughlin, Asefeh Jarandehei, Michelle Miller, et al. High-throughput analysis of single hematopoietic stem cell proliferation in microfluidic cell culture arrays. *Nature methods*, 8(7):581–586, 2011.

[76] Jessamine Ng Lee, Cheolmin Park, and George M Whitesides. Solvent compatibility of poly (dimethylsiloxane)-based microfluidic devices. *Analytical chemistry*, 75(23):6544–6554, 2003.

[77] Hartmuth C Kolb, MG Finn, and K Barry Sharpless. Click chemistry: diverse chemical function from a few good reactions. *Angewandte Chemie International Edition*, 40(11):2004–2021, 2001.

[78] Mikael Hillmering. *Polymer microfluidic systems for samplepreparation for bacterial detection.* PhD thesis, KTH Royal Institute of Technology, Department of Micro and Nanosystems, 2014.

[79] Charles E Hoyle and Christopher N Bowman. Thiol–ene click chemistry. *Angewandte Chemie International Edition*, 49(9):1540–1573, 2010.

[80] Alessandro Dondoni. The emergence of thiol–ene coupling as a click process for materials and bioorganic chemistry. *Angewandte Chemie International Edition*, 47(47):8995–8997, 2008.

[81] Matthew J Kade, Daniel J Burke, and Craig J Hawker. The power of thiol-ene chemistry. *Journal of Polymer Science Part A: Polymer Chemistry*, 48(4):743–750, 2010.

[82] Farizah Saharil, Lamia El Fissi, Yitong Liu, Fredrik Carlborg, Denis Vandormael, Laurent A Francis, Wouter van der Wijngaart, and Tommy Haraldsson. Superior dry bonding of off-stoichiometry thiol-ene epoxy (OSTE (+)) polymers for heterogeneous material labs-on-chip. In *Proceedings Micro Total Analysis Systems (muTAS)*, pages 1831–1833, 2012.

[83] Farizah Saharil, Carl Fredrik Carlborg, Tommy Haraldsson, and Wouter van der Wijngaart. Biocompatible "click" wafer bonding for microfluidic devices. *Lab on a Chip*, 12(17):3032–3035, 2012.

[84] Carlos Errando-Herranz, Alexander Vastesson, Marina Zelenina, Gaspard Pardon, Gunnar Bergström, Wouter van der Wijngaart, Tommy Haraldson, Hjalmar Brismar, and Kristinn B Gylfason. Biocompatibility of OSTE polymers studied by cell growth experiments. In *Proc. MicroTAS*, 2013.

[85] Farizah Saharil, Kristinn B Gylfason, Yitong Liu, Tommy Haraldsson, Paolo Bettotti, Neeraj Kumar, and Wouter van der Wijngaart. Dry transfer bonding of porous silicon membranes to OSTE (+) polymer microfluidic devices. In *Micro Electro Mechanical Systems (MEMS), IEEE 25th International Conference on*, pages 232–234. IEEE, 2012.

[86] Richard P Feynman. There's plenty of room at the bottom. *Engineering and science*, 23(5):22–36, 1960.

[87] Sami Franssila. *Introduction to Microfabrication*. John Wiley & Sons, 2nd edition, 2010.

[88] MicroChemicals. Photolithography, 2012.

[89] Farizah Saharil, Fredrik Forsberg, Yitong Liu, Paolo Bettotti, Neeraj Kumar, Frank Niklaus, Tommy Haraldsson, Wouter van der Wijngaart, and Kristinn B Gylfason. Dry adhesive bonding of nanoporous inorganic membranes to microfluidic devices using the OSTE (+) dual-cure polymer. *Journal of Micromechanics and Microengineering*, 23(2):025021, 2013.

[90] Hiroaki Oka, Ken Shimono, Ryuta Ogawa, Hirokazu Sugihara, and Makoto Taketani. A new planar multielectrode array for extracellular recording: application to hippocampal acute slice. *Journal of neuroscience methods*, 93(1):61–67, 1999.

[91] E Claverol-Tinture, M Ghirardi, F Fiumara, X Rosell, and J Cabestany. Multielectrode arrays with elastomeric microstructured overlays for extracellular recordings from patterned neurons. *Journal of neural engineering*, 2(2):L1, 2005.

[92] Damien C Rodger, Andy J Fong, Wen Li, Hossein Ameri, Ashish K Ahuja, Christian Gutierrez, Igor Lavrov, Hui Zhong, Parvathy R Menon, Ellis Meng, et al. Flexible parylene-based multielectrode array technology for high-density neural stimulation and recording. *Sensors and Actuators B: chemical*, 132(2):449–460, 2008.

[93] Yevgeny Berdichevsky, Helen Sabolek, John B Levine, Kevin J Staley, and Martin L Yarmush. Microfluidics and multielectrode array-compatible organotypic slice culture method. *Journal of neuroscience methods*, 178(1):59–64, 2009.

[94] Khalil Najafi and Kensall D Wise. An implantable multielectrode array with on-chip signal processing. *Solid-State Circuits, IEEE Journal of*, 21(6):1035–1044, 1986.

[95] Almut Branner and Richard Alan Normann. A multielectrode array for intrafascicular recording and stimulation in sciatic nerve of cats. *Brain research bulletin*, 51(4):293–306, 2000.

[96] J Selvakumaran, MP Hughes, JL Keddie, and DJ Ewins. Assessing biocompatibility of materials for implantable microelectrodes using cytotoxicity and protein adsorption studies. In *Microtechnologies in Medicine & Biology 2nd Annual International IEEE-EMB Special Topic Conference on*, pages 261–264. IEEE, 2002.

[97] Alpha MED Scientific. MED Probe. `http://www.med64.com/products/medprobe.html`, January 2015.

[98] Allan Mills. Porous platinum morphologies: Platinised, sponge and black. *Platinum Met. Rev*, 51(1):52, 2007.

[99] Alpha MED Scientific. Dissociate culture of rat cardiac myocytes on the MED probe. `http://www.med64.com/resources/methods_cardiac.html`, January 2015.

[100] Sumio Iijima et al. Helical microtubules of graphitic carbon. *Nature*, 354(6348):56–58, 1991.

[101] Weldons. Fancy coloured diamonds. `http://weldons.ie/fancy-coloured-diamonds/`, January 2015.

[102] Andre K Geim and Konstantin S Novoselov. The rise of graphene. *Nature materials*, 6(3):183–191, 2007.

[103] EV World. Graphene: The stuff dreams are made of. `http://evworld.com/article.cfm?storyid=1950`, February 2015.

[104] John Robertson. Electronic and atomic structure of diamond-like carbon. *Semiconductor science and technology*, 18(3):S12, 2003.

[105] Yong Seob Park, Hyun Sik Myung, Jeon Geon Han, and Byungyou Hong. The electrical and structural properties of the hydrogenated amorphous carbon films grown by close field unbalanced magnetron sputtering. *Thin solid films*, 482(1):275–279, 2005.

[106] Hyun S Myung, Yong S Park, Min J Jung, B Hong, and Jeon G Han. Synthesis and mechanical properties of amorphous carbon films by closed-field unbalanced magnetron sputtering. *Materials Letters*, 58(9):1513–1516, 2004.

[107] Yong Seob Park, Hyun Sik Myung, Jeon Geon Han, and Byungyou Hong. Tribological properties of amorphous carbon thin films grown by magnetron sputtering method. *Surface and Coatings Technology*, 180:218–221, 2004.

[108] Yong Seob Park, Hyun Sik Myung, Jeon Geon Han, and Byungyou Hong. Characterization of CN_x thin films prepared by close field unbalanced magnetron sputtering. *Thin solid films*, 475(1):298–302, 2005.

[109] Jin-Hyo Boo, Heon Kyu Park, Kyung Hoon Nam, and Jeon Geon Han. High rate deposition of poly-Si thin films at low temperature using a new designed magnetron sputtering source. *Surface and Coatings Technology*, 131(1):211–215, 2000.

[110] Šarūnas Meškinis, V Kopustnikas, Kęstutis Šlapikas, Rimas Gudaitis, Asta Guobienė, and Sigitas Tamulevičius. Oxygen ion beam etching of diamond like carbon films. *Materials Science (Medžiagotyra)*, 13(4), 2007.

[111] Yutaka Ando, Yoshiki Nishibayashi, Koji Kobashi, Takashi Hirao, and Kenjiro Oura. Smooth and high-rate reactive ion etching of diamond. *Diamond and Related Materials*, 11(3):824–827, 2002.

[112] PW Leech, GK Reeves, and A Holland. Reactive ion etching of diamond in cf4, o2, o2 and ar-based mixtures. *Journal of materials science*, 36(14):3453–3459, 2001.

[113] GF McLane and JR Flemish. High etch rates of SiC in magnetron enhanced SF_6 plasmas. *Applied physics letters*, 68(26):3755–3757, 1996.

[114] Rob Legtenberg, Henri Jansen, Meint de Boer, and Miko Elwenspoek. Anisotropic reactive ion etching of silicon using SF_6 / O_2 / CHF_3 gas mixtures. *Journal of The Electrochemical Society*, 142(6):2020–2028, 1995.

[115] Jonathan L Schaffer, Michael Rizen, Gilbert J L'Italien, Aziz Benbrahim, Joseph Megerman, Louis C Gerstenfeld, and Martha L Gray. Device for the application of a dynamic biaxially uniform and isotropic strain to a flexible cell culture membrane. *Journal of Orthopaedic Research*, 12(5):709–719, 1994.

[116] Thomas D Brown. Techniques for mechanical stimulation of cells in vitro: a review. *Journal of biomechanics*, 33(1):3–14, 2000.

[117] Maria Berdova, Tuomo Ylitalo, Ivan Kassamakov, Jouni Heino, Pekka T Törmä, Lauri Kilpi, Helena Ronkainen, Jari Koskinen, Edward Hæggström, and Sami Franssila. Mechanical assessment of suspended ALD thin films by bulge and shaft-loading techniques. *Acta Materialia*, 66:370–377, 2014.

[118] Pinyen Lin. *The in-situ measurement of mechanical properties of multi-layer coatings*. PhD thesis, Massachusetts Institute of Technology, 1990.

[119] James M Gere. *Mechanics of Materials*. Brooks Cole, 6th edition, 2004.

[120] Dow Corning. Sylgard® 184 silicone elastomer kit. `http://www.dowcorning.com/applications/search/products/details.aspx?prod=01064291`, February 2015.

[121] Google Patents. Mixture of potassium sorbate and microcrystalline cellulose, talc. `http://www.google.com/patents/US7906151`, February 2015.

[122] Sigma Aldrich. Pentaerythritol tetrakis(3-mercaptopropionate). `http://www.sigmaaldrich.com/catalog/product/aldrich/381462?lang=fi&region=FI`, February 2015.

[123] Sigma Aldrich. Trimethylolpropane diallyl ether. `http://www.sigmaaldrich.com/catalog/product/aldrich/416126?lang=fi&region=FI`, February 2015.

[124] Google Patents. A variable reflectance mirror for the interior or exterior of vehicles; incorporating a reflector/electrode on the inside (third) surface of a dimming portion rearview; adhesive to bond elements to form chamber; corrosion resistance. `http://www.google.com/patents/US6963439`, February 2015.

[125] Chemical Book. Ethyl (2,4,6-trimethylbenzoyl) phenylphosphinate. `http://www.chemicalbook.com/ChemicalProductProperty_EN_CB9855469.htm`, February 2015.

[126] Sigma Aldrich. 1,5-diazabicyclo[4.3.0]non-5-ene. `http://www.sigmaaldrich.com/catalog/product/aldrich/136581?lang=fi&region=FI`, February 2015.

[127] Alenka Vesel and Miran Mozetic. Surface modification and ageing of PMMA polymer by oxygen plasma treatment. *Vacuum*, 86(6):634–637, 2012.

[128] M Reza Nejadnik, Adam LJ Olsson, Prashant K Sharma, Henny C van der Mei, Willem Norde, and Henk J Busscher. Adsorption of Pluronic F-127 on surfaces with different hydrophobicities probed by quartz crystal microbalance with dissipation. *Langmuir*, 25(11):6245–6249, 2009.

[129] Julia Schütte, Christian Freudigmann, Karin Benz, Jan Böttger, Rolf Gebhardt, and Martin Stelzle. A method for patterned in situ biofunctionalization in injection-molded microfluidic devices. *Lab on a Chip*, 10(19):2551–2558, 2010.

[130] Maria Kitsara and Jens Ducrée. Integration of functional materials and surface modification for polymeric microfluidic systems. *Journal of Micromechanics and Microengineering*, 23(3):033001, 2013.

[131] Zhigang Wu and Klas Hjort. Surface modification of PDMS by gradient-induced migration of embedded Pluronic. *Lab on a Chip*, 9(11):1500–1503, 2009.

[132] V Brunetti, G Maiorano, L Rizzello, B Sorce, S Sabella, R Cingolani, and PP Pompa. Neurons sense nanoscale roughness with nanometer sensitivity. *Proceedings of the National Academy of Sciences*, 107(14):6264–6269, 2010.

[133] W. S. Bacsa, J. S. Lannin, D. L. Pappas, and J. J. Cuomo. Raman scattering of laser-deposited amorphous carbon. *Phys. Rev. B*, 47:10931–10934, Apr 1993.

[134] Konstantin Iakoubovskii, Nobutsugu Minami, Taro Ueno, Said Kazaoui, and Hiromichi Kataura. Optical characterization of double-wall carbon nanotubes: Evidence for inner tube shielding. *The Journal of Physical Chemistry C*, 112(30):11194–11198, 2008.

[135] University of Maryland. Electrons can travel over 100 times faster in graphene than in silicon, physicists show. `www.sciencedaily.com/releases/2008/03/080324094514.htm`, September 2015.

[136] Inc Element Collection. Resistivity of the elements. `http://periodictable.com/Properties/A/Resistivity.html`, September 2015.

[137] H.O. Pierson. *Handbook of Carbon, Graphite, Diamond and Fullerenes - Properties, Processing and Applications*. William Andrew Publishing/Noyes, 1993.

[138] Philip D. Rack. Plasma etching. `http://wcam.engr.wisc.edu/Public/Reference/PlasmaEtch/Etching.pdf`, December 2014.

[139] E.D. Babich, A.C. Callegari, F.E. Doany, and S. Purushothaman. Sputter deposition of hydrogenated amorphous carbon film and applications thereof, November 3 1998. US Patent 5,830,332.

[140] M Massi, JMJ Ocampo, HS Maciel, K Grigorov, C Otani, LV Santos, and Ronaldo Domingues Mansano. Plasma etching of DLC films for microfluidic channels. *Microelectronics journal*, 34(5):635–638, 2003.

[141] Jing Qu, Dan Wang, Huihui Wang, Yunhai Dong, Feng Zhang, Baoqi Zuo, and Huanxiang Zhang. Electrospun silk fibroin nanofibers in different diameters support neurite outgrowth and promote astrocyte migration. *Journal of Biomedical Materials Research Part A*, 101(9):2667–2678, 2013.

[142] Shantanu Sur, Eugene T Pashuck, Mustafa O Guler, Masao Ito, Samuel I Stupp, and Thomas Launey. A hybrid nanofiber matrix to control the survival and maturation of brain neurons. *Biomaterials*, 33(2):545–555, 2012.

[143] Jie Cai, Xuejun Peng, Kevin D Nelson, Robert Eberhart, and George M Smith. Permeable guidance channels containing microfilament scaffolds enhance axon growth and maturation. *Journal of Biomedical Materials Research Part A*, 75(2):374–386, 2005.

[144] Namiko Ishikawa, Y Suzuki, M Ohta, H Cho, S Suzuki, M Dezawa, and C Ide. Peripheral nerve regeneration through the space formed by a chitosan gel sponge. *Journal of Biomedical Materials Research Part A*, 83(1):33–40, 2007.

[145] Wolfgang Liedtke, Michele Yeo, Hongbo Zhang, Yiding Wang, Michelle Gignac, Sara Miller, Ken Berglund, and Jie Liu. Highly conductive carbon nanotube matrix accelerates developmental chloride extrusion in central nervous system neurons by increased expression of chloride transporter KCC2. *Small*, 9(7):1066–1075, 2013.

[146] Sung Young Park, Jaesung Park, Sung Hyun Sim, Moon Gyu Sung, Kwang S Kim, Byung Hee Hong, and Seunghun Hong. Enhanced differentiation of human neural stem cells into neurons on graphene. *Advanced Materials*, 23(36):H263–H267, 2011.

A Calculation for OSTE

Calculations for OSTE polymer are presented here. The needed information are molecular weights of the monomers (thiol and allyl), number of functional groups in one molecule, desired weight and used stoichiometry. Material data of TMPEC and TMPDE are presented in Table A1.

Table A1: Material data for OSTE polymer

Material	**Molecular weight (g/mol)**	**Functional groups**
TMPEC	n_{Thiol} = 488.64	4
TMPDE	n_{Allyl} = 214.30	2

The needed amounts for these two materials depend on used off-stoichiometry and desired final polymer weight. Let's call the off-stoichiometry ratio with letter S, which means that there will be S % more thiol functional groups. Table A2 shows formulas for proper weight calculation. The principle is that first S is used to calculate the mole percentage for both materials, and that is transformed into weight (as mole mass is known). User has to decide what is the sum of both materials mole*functional groups (0.0863 == 10 g, 0.1208 == 14 g).

Table A2: Calculations for OSTE material. Lower table shows calculations with example values.

Off-stoichiometry = S

	mol %	**mole*func.grp**	**func. grps**	**mol**	**weight (g)**	**g/mol**
Thiol	$\frac{1+S}{2+S}$=A	D*A	X	$\frac{D*A}{X}$	$\frac{D*A}{X}$*n_{Thiol}	n_{Thiol}
Allyl	$\frac{1}{2+S}$=B	D*B	Y	$\frac{D*B}{Y}$	$\frac{D*B}{Y}$*n_{Allyl}	n_{Allyl}
SUM	100 %	D			w_{Total}	

Example calculation for OSTE. Now D = 0.1035 and S = 40 %

	mol %	**mole*func.grp**	**func. grps**	**mol**	**weight (g)**	**g/mol**
Thiol	58.33 %	0.0604	4	0.0151	7.38	488.64
Allyl	41.67 %	0.0431	2	0.0216	4.62	214.30
SUM	100 %	0.1035			12.00	

B Calculation for OSTE+

Calculations for OSTE+ polymer are presented here. The needed information is molecular weights of the monomers (thiol, allyl and epoxy), number of functional groups in one molecule, desired weight and used stoichiometry for both thiol and epoxy. Material data of TMPEC, TMPDE and DEN 431 are presented in Table B1.

Table B1: Material data for OSTE+ polymer

Material	**Molecular weight (g/mol)**	**Functional groups**
TMPEC	n_{Thiol} = 488.64	4
TMPDE	n_{Allyl} = 214.30	2
DEN 431	n_{Epoxy} = 174.00	1

The needed amounts for these two materials depend on used off-stoichiometry (thiol and epoxy) and desired final polymer weight. Let's call the off-stoichiometry ratio with letter S_T for thiol and S_E for epoxy, which means that there will be S % more thiol or epoxy functional groups. Table B2 shows formulas for proper weight calculation. Lower table shows example calculations. To start the calculations, the w_{Thiol} is assumed to be 1.0000 g.

Table B2: Calculations for OSTE+ material. Lower table shows calculations with example values.

Off-stoichiometry = S_T for thiol and S_E for epoxy

Monomer	**weight(g)**	**g/mol**	**mol**	**func.grps**	**mol*func.grps**
Thiol	w_{Thiol}	n_{Thiol}	$\frac{w_{Thiol}}{n_{Thiol}}$	A	$\frac{w_{Thiol}}{n_{Thiol}} * A = N$
Allyl	$n_{Allyl} * \frac{M}{B} = w_{Allyl}$	n_{Allyl}	$\frac{M}{B}$	B	$\frac{N}{1+S_T} = M$
Epoxy	$n_{Epoxy} * \frac{K}{C} = w_{Epoxy}$	n_{Epoxy}	$\frac{K}{C}$	C	(N-M)*S_E=K
	w_{Total}				

Example calculation for OSTE+. Off-stoichiometry: S_T = 60 % and S_E = 40 %

Monomer	**weight(g)**	**g/mol**	**mol**	**func.grps**	**mol*func.grps**
Thiol	1.0000	488.64	0.002046	4	0.008186
Allyl	0.54821	214.30	0.002558	2	0.005116
Epoxy	0.74779	174.00	0.004298	1	0.004298
	2.295995				

Scale the acquired weight to match your desired weight.